Title

Mechanical Instability, Phase Separation and Fracture Phenomena in Soft Materials

Author

Zhou, Yu

Publication Date

2024

Peer reviewed|Thesis/dissertation

UNIVERSITY OF CALIFORNIA

Los Angeles

Mechanical Instability, Phase Separation and Fracture Phenomena in Soft Materials

A dissertation submitted in partial satisfaction of the

requirements for the degree Doctor of Philosophy

in Mechanical Engineering

by

Yu Zhou

2024

ABSTRACT OF THE DISSERTATION

Mechanical Instability, Phase Separation and Fracture Phenomena in Soft Materials

by

Yu Zhou

Doctor of Philosophy in Mechanical Engineering

University of California, Los Angeles, 2024

Professor Lihua Jin, Chair

Soft materials, such as elastomers, hydrogels, and liquid crystal elastomers (LCEs), exhibit unique mechanical properties like hyperelasticity, poroelasticity, and anisotropy, stemming from their molecular structures. Elastomers are rubber-like materials composed of cross-linked long-chain polymer networks, while hydrogels consist of cross-linked polymer networks immersed in a solvent. Unlike hydrogels, LCEs combine polymer networks with liquid crystal mesogens, exihibiting semisoft elasticity where a finite, though small, stress is required to rotate the mesogens. These materials find applications in both natural and artificial structures, including biological tissues, soft robots, and flexible sensors.

Under extreme external loading conditions, soft materials can display various deformation behaviors such as mechanical instability, phase separation, and fracture. These behaviors are highly nonlinear and not fully understood. For instance, mechanical instability under extreme compression can significantly alter the shape and load-bearing capacity of the materials. Dramatic environmental changes can induce phase separation in a homogeneous mixture, causing it to split into different phases. Additionally, extreme tension can cause soft materials to fracture into multiple pieces. This dissertation aims to study these phenomena and uncover the underlying mechanisms driving these complex behaviors.

First, we study mechanical instability through elastomeric tube structures. Specifically, we conduct three-dimensional buckling and postbuckling analysis for thick hyperelastic tubes subjected to axial compression under finite deformation by the asymptotic expansion method. Our theoretical results successfully predict the deformation and stress-strain curves of buckled tubes near the critical loading, which are well validated by finite element analysis. Depending on the geometry, three kinds of postbuckling paths, including continuous buckling, snap-through and snap-back, are discovered. Our work provides understanding and insights into the buckling and postbuckling of thick tubes, and bridges the knowledge gap between postbuckling of thick columns and tubes.

Second, we investigate the underpinning role of mechanical constraints and dynamic loading on triggering volume phase transitions and phase separation of hydrogels. Using the Flory-Rehner free energy, which does not predict phase separation of hydrogels under equilibrium free swelling, we show that mechanical constraints can lead to coexistence of multiple phases. We systematically obtain the states of equilibrium for hydrogels under various mechanical constraints,

and unravel how mechanical constraints change the convexity of the free energy and monotonicity of the stress-stretch curves, leading to phase coexistence. Using a phase-field model, we predict the pattern evolution of phase coexistence, and show many features cannot be captured by the homogeneous states of equilibrium due to large mismatch stretch between the coexisting phases. We further reveal that the system size, quenching rate, and loading rate can significantly influence the phase behavior, which provides insights for experimental studies related to morphological patterns of hydrogels.

Lastly, we investigate the fracture behavior of liquid crystal elastomers (LCEs). We begin by developing a modified semisoft constitutive model to accurately capture their unique mechanical responses. Next, we address the gap in understanding the effect of deformation-director coupling on LCE fracture paths and the lack of established fracture criteria. By combining experimental and theoretical approaches, we aim to elucidate fracture propagation in LCEs. We stretch edge-cracked monodomain LCE samples, recording their stress-strain responses and crack paths under varying initial directors and stretching rates. Our findings reveal that crack propagation paths are highly dependent on both the initial director and the stretching rate. To further understand LCE fracture behavior, we develop a rate-dependent phase-field fracture model, which is validated through experiments and demonstrates the ability to predict complex fracture paths. Our study paves the way for designing LCEs with enhanced fracture properties, beneficial for future applications.

The dissertation of Yu Zhou is approved.

Ajit Mal

Mohammed Khalid Jawed

Samanvaya Srivastava

Vinay Goyal

Lihua Jin, Committee Chair

University of California, Los Angeles

2024

TABLE OF CONTENTS

LIST OF FIGURES

LIST OF TABLES

ACKNOWLEDGMENTS

First and foremost, I would like to express my deepest and sincerest gratitude to my advisor, Prof. Lihua Jin. These past six years have been incredibly challenging for me. Three years ago, I experienced profound depression and frustration, feeling unable to achieve my ambitions. I reached my loneliest, lowest, and darkest state during my PhD. My life and research were completely stuck. I struggled with rest, and for about two years, I had no research outcomes. Prof. Jin, you always supported me, no matter what. Your kind words inspired me. I wrote in my notebook, "I must do something to repay your patience, kindness, and warmth. I felt I would climb a mountain of swords or plunge into a sea of flames." Gradually, I adjusted myself and emerged from that difficult situation. Even though progress has been slow over the last two years, I feel happy and determined. As an advisor, Prof. Jin gave me the freedom to pursue my interests and consistently provided insightful understanding of physics. With her guidance, I gradually learned to identify important and interesting problems, and became more confident as a researcher. Prof. Jin has always given me the utmost support for any opportunity. I truly feel fortunate to be one of her students. Thank you, Prof. Jin! You are genuinely a great person, friend, and advisor. I wish you and the group continued success in research, and I wish you and your family happiness, health, and all the best.

I would also like to thank my committee members: Prof. Ajit Mal, Prof. M Khalid Jawed, Prof. Samanvaya Srivastava, Prof. Vinay Goyal, and Prof. Alex Levine, for their invaluable suggestions and comments on my research. I deeply appreciate Prof. Ajit Mal for his support and for kindly writing recommendation letters for me. I also want to thank Prof. Vinay Goyal for his

appreciation when I first arrived at UCLA, which gave me tremendous courage to meet the challenges in academia.

I am thankful to my collaborators. I gained significant knowledge about tumor growth from Dr. Jiayi Du and Prof. Ke Sheng. I also appreciate Chen Wei for his work on LCEs. I am grateful to Prof. Wei Hong for sharing the COMSOL file with me, which greatly helped me learn the software. I am particularly thankful to Prof. Yuzhen Chen for his enormous help in both research and life. His support has been priceless, and I will always remember his assistance. I also thank all the group members in the Mechanics of Soft Materials Lab.

I am grateful to Prof. Jinxiong Zhou and Prof. Zishun Liu. I have learned so much from their groups, which helped me develop my research skills. Prof. Zishun Liu is one of the kindest people in the world. Prof. Liu, thank you for giving me all the opportunities and support.

I thank the UCLA Martial Arts Program. It was my sole activity outside of research, helping me become tougher both physically and mentally. I am grateful to all the incredible people I met there.

I also want to thank all my friends. Your encouragement helped me through the difficulties I encountered. I would like to especially thank Zidi Zhou. We share our stories and encourage each other. Your constant support motivates me to improve in all aspects. I hope this continues forever.

Without my parents, I wouldn't be here. Thank you for your endless love, care, support, and understanding. We will always be together. I thank all my family members. To my late grandparents, I will explore the wider world for you. I hope you can rest in peace.

I often blame myself, but I would like to thank myself lastly. You did well. You have grown a lot. You learned to forgive yourself. Thank you for continuing to move forward. Just prepare for the next step. You have a lifetime to realize your dream.

VITA

2014-2018 B.S. in Engineering Mechanics, Xi'an Jiaotong University, China.

PUBLICATIONS

[1] **Zhou, Y.**, Chen, Y., & Jin, L. (2023). Three-dimensional postbuckling analysis of thick hyperelastic tubes. *Journal of the Mechanics and Physics of Solids*, 173, 105202.

[2] **Zhou, Y.**, & Jin, L. (2023). Mechanics underpinning phase separation of hydrogels. *Macromolecules*, *56*(2), 426-439.

[3] Xuan, C.[1], **Zhou, Y.**[1], Zhao, Y., He, X., & Jin, L. (2022). Photodriven self-excited hydrogel oscillators. *Physical Review Applied*, 17(1), 014007. ([1]Equal contributions)

[4] **Zhou, Y.**, & Jin, L. (2020). Hydrolysis-induced large swelling of polyacrylamide hydrogels. *Soft Matter*, 16(24), 5740-5749.

[5] **Zhou, Y.**, Hu, J., & Liu, Z. (2019). Deformation behavior of fiber-reinforced hydrogel structures. *International Journal of Structural Stability and Dynamics*, 19(03), 1950032.

[6] **Zhou, Y.**, Wei, C., & Jin, L. (2024). Fracture of liquid crystal elastomers. *In preparation*.

[7] **Zhou, Y.**, Wei, C., & Jin, L. (2024). A modified semisoft model of liquid crystal elastomers: application to elastic and viscoelastic responses. *In preparation*.

[8] Wei, C., **Zhou, Y.**, Hsu, B., & Jin, L. (2023). Exceptional stress-director coupling at the crack tip of a liquid crystal elastomer. *Journal of the Mechanics and Physics of Solids*, 105522.

[9] Wei, C., Cao, S., **Zhou, Y.**, Lin, D., & Jin, L. (2023). Rate-dependent stress-order coupling in main-chain liquid crystal elastomers. *Soft Matter*, 19(41), 7923-7936.

[10] Du, J., **Zhou, Y.**, Jin, L., & Sheng, K. (2023). Gell: A GPU-powered 3D hybrid simulator for large-scale multicellular system. *Plos one*, 18(7), e0288721.

Chapter 1 Introduction

Soft materials are prevalent in nature and everyday life, characterized by their ability to deform easily. This deformation enables various functions, making soft materials highly versatile. In engineering, they have numerous potential applications, including human-machine interfaces and use in complex environments [1-4]. Their similarity to biological tissues allows for seamless integration between biological systems and electronic devices. Additionally, soft materials can be easily activated by stimuli such as temperature, light, magnetic fields, electric fields, and mechanical stresses, which allows them to function as actuators and soft robotics [5-8]. Compared to traditional robotics, soft robotics offer enhanced safety, adaptability, and flexibility.

1.1 Basics of Soft Materials

Soft materials have been extensively developed and investigated over the past few decades. Typical soft materials, such as elastomers (Figure 1.1a), hydrogels (Figure 1.1b), and LCEs (Figure 1.1c), exhibit unique mechanical properties such as hyperelasticity, poroelasticity, and anisotropy. Figure 1.1 illustrates examples of soft materials. Figure 1.1a demonstrates a fluidic soft elastomeric jumper that utilizes snap-through instability to release energy suddenly and deform quickly [9]. Figure 1.1b depicts a polyelectrolyte hydrogel undergoing large volume changes as solvent molecules diffuse in and out of the hydrogel [10]. Figure 1.1c shows an image sequence of a LCE actuator lifting a weight in response to temperature changes [11].

Elastomers are rubber-like materials with elastic properties, which are cross-linked long chain polymer networks (Figure 1.2a). The elastic energy change is usually associated with the entropy change when the material is deformed [12, 13]. For example, when an elastomer is

stretched, the network chains become straight and the entropy decreases. The entropy decrease leads to the elastic energy increase. Typical constitutive model to describe them is the neo-Hookean elastic energy density function, where stress-stretch response is nonlinear [12, 13]. The shear modulus is proportional to the cross-link density and temperature. Elastomers can be applied in various industries such as automotive sector and medical devices [14-16]. They can also be functionalized by adding other components; examples include dielectric elastomers [17, 18] and magnetorheological elastomers [19-21] that can be driven by electric and magnetic fields, respectively.

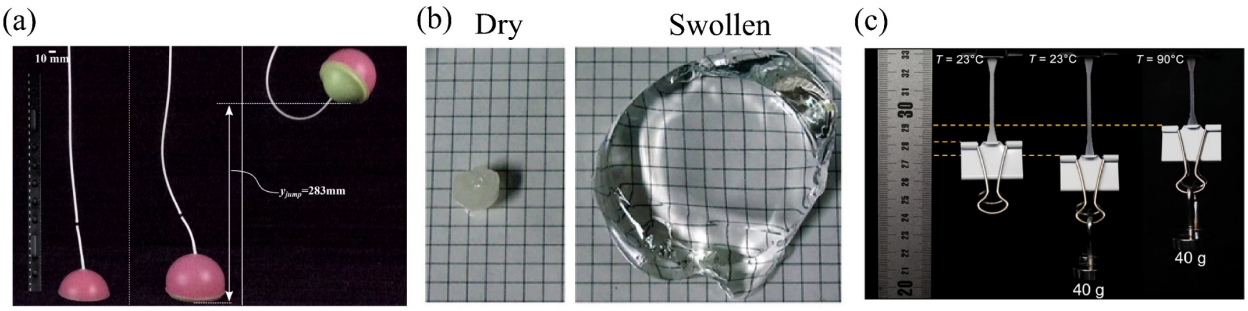

Figure 1.1 Examples of soft materials. (a) Inflatable soft jumper made of elastomeric materials [9]. (b) Dried hydrogel and swollen hydrogel showing a significant volume change [10]. (c) Liquid crystal elastomers lifting a weight in response to temperature change [11].

Hydrogels consist of crosslinked polymer networks immersed in a solvent, which are essentially elastomers swelled in a solvent (Figure 1.1b). Hydrogels can swell or shrink in response to many external stimuli, such as variation of ionic strength, pH, temperature, light and electrical fields [22, 23]. These stimuli-responsive hydrogels have wide applications in engineering sectors of sensing and actuation [24, 25]. In addition, the mechanical, electrical and biological properties

of hydrogels can be easily designed, rendering hydrogels ideal materials to bridge biology and electronics [1].

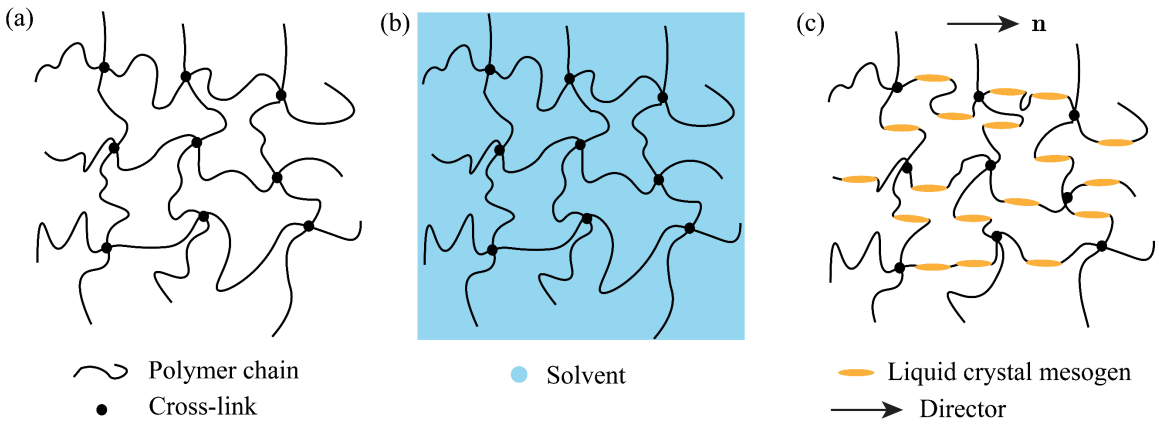

Figure 1.2 Schematic of (a) an elastomer, (b) a hydrogel, and (c) an LCE.

Different from hydrogels, LCEs are combinations of polymer networks and liquid crystal mesogens (Figure 1.1c). The coupling between polymer networks and mesogens leads to unusual mechanical properties of LCEs, such as semisoft elasticity where a finite but small stress is required to rotate the liquid crystal mesogens within the polymer network and viscoelasticity [26]. LCEs can undergo large deformation in response to various external stimuli [27], including temperature [28], light [29], and electric fields [30]. mechanical stress [31]. As a result, LCEs have many potential applications, including energy dissipation [32-34], robotics [35, 36], actuation [37, 38], and so on.

1.2 Intriguing Phenomena under External Loadings

Soft materials, with their long flexible polymer chains, can undergo large deformations under external loadings. Extreme loading conditions can lead to various deformation behaviors,

including mechanical instability, phase separation, and fracture. Soft materials can undergo different types of elastic instabilities without permanent deformation. For instance, when an elastomeric beam structure is compressed, different types of buckling behavior, such as continuous, snap-through, and snap-back buckling, can be obtained depending on the beam's width-to-length ratio (Figure 1.3a) [39]. With such simple geometry, the large deformation of soft materials results in geometric nonlinearity, leading to fascinating phenomena. These elastic instabilities enable soft materials to achieve desired responses in simple and inexpensive ways, allowing for novel designs in sensors, actuators, dampers, and soft robotics [40-42].

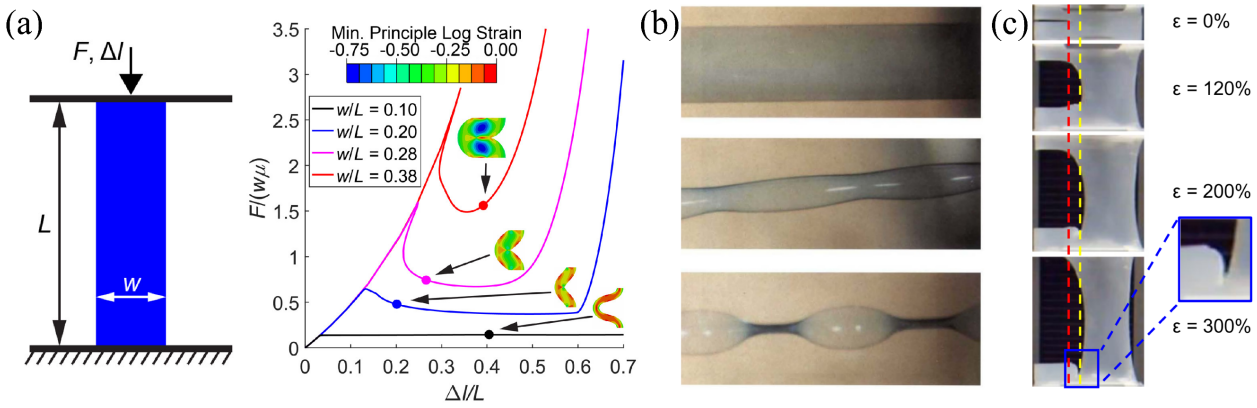

Figure 1.3 (a) An elastomeric beam structure under compression. Continuous, snap-through, and snap-back buckling, and creasing are predicted with different beam width-to-length ratios [39]. (b) Pattern formation in a shrinking hydrogel immersed in a poor solvent [43]. (c) Sideways crack propagation in a pre-cracked silicone elastomer subjected to vertical stretching. The crack terminates at the boundary [44].

Instabilities can be triggered by mechanical forces or other stimuli such as temperature, pH, and electric fields. For example, in hydrogels, a dramatic change in the external environment

can cause the material to lose stability, leading to phase separation [43]. This phase separation can enhance the material's properties and induce morphological changes [43, 45, 46]. Additionally, mechanical constraints can further influence pattern development (Figure 1.3b). The coupling between large deformation, solvent diffusion, and instability makes these phenomena particularly challenging to investigate.

Fracture can occur in thin films under extreme tension, leading to various intriguing phenomena depending on the material's molecular structure. For example, in silicone elastomers, sideways crack propagation is observed, with the crack stopping at the boundary, allowing for enormous stretchability (Figure 1.3c) [44]. In viscoelastic materials with dynamic bonds, different fracture responses occur at different loading rates [47]. At a low loading rate, the precrack opens, the crack surface becomes blunted, and no crack propagation occurs. At an intermediate loading rate, the crack propagates and then stops. At a high loading rate, the crack propagates and ultimately fractures the sample. These phenomena cannot be explained by existing fracture theories.

1.3 Motivation and Objectives

The above phenomena are highly nonlinear, and some are poorly understood. In addition, in material systems such as hydrogels and LCEs, the material response often involves multiple physical processes, which further complicates the challenges. These complexities require advanced theoretical, numerical and experimental approaches for a comprehensive understanding. There are several key knowledge gaps in the field of soft material mechanics. Firstly, understanding mechanical instability under finite deformation states is crucial, as these materials

undergo large deformations. Secondly, developing new constitutive models to describe material behavior is essential. Thirdly, investigating material instability in systems that couple multiple physical processes is particularly challenging. Lastly, exploring how materials fracture under different conditions is necessary to improve fracture properties for practical applications. Addressing these knowledge gaps will provide valuable insights into material responses and help develop better-performing materials.

In this dissertation, we will explore mechanical instability, phase separation, and fracture phenomena in the following material systems to address some of these knowledge gaps. Elastomers, with their pure elastic deformation, are suitable systems for investigating mechanical instability. Hydrogels, composed of polymer networks and solvent, are good candidates for studying phase separation. LCEs, as viscoelastic materials combining polymer networks and liquid crystals, are ideal systems for exploring interesting fracture behaviors. Specifically, we study buckling and postbuckling of elastomeric tube structures (Figure 1.4), phase separation of hydrogels (Figure 1.5) under various mechanical constraints and dynamic loading conditions, and fracture of viscoelastic LCEs (Figure 1.6).

As for elastomeric tube structures, they are widely found in biological and engineering systems, such as microtubules [48], blood vessels [49], packers [50], foams [51] and lattices [52]. They play critical roles in transporting fluid and nutrition in engineering and biological systems. Although the hollow structures of tubes impart them with lightweight properties, tubes are susceptible to buckling under axial and lateral loadings (Figure 1.4). Predicting the buckling and postbuckling of tubes is essential for their applications. As a particular example, lightweight lattice structures composed of hollow tubes are designed to control deformation [53] and absorb energy

[54]. By tuning the wall thickness, the buckling and postbuckling of the tubes can be significantly altered. As a result, researchers are not only able to change the elastic isotropy of the lattices, but also the stress-strain curve and recoverable energy absorption. Despite the wide application of instabilities of tube structures, the theoretical postbuckling analysis has barely been done.

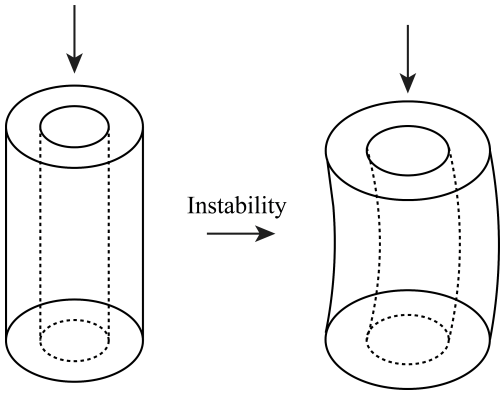

Figure 1.4 Schematic of mechanical instability of a tube structure.

Hydrogels, composed of polymer networks and solvents, can significantly change the volume through the transport of solvent molecules. Certain hydrogels can undergo a discontinuous volume transition from a swollen state to a shrunk state, which is called a volume phase transition [55-57]. Hydrogels capable of a volume phase transition have diverse applications, including sensors [58], actuators [59], soft robots [60], drug delivery [61], and so on. During the process of a volume phase transition, which is governed by the kinetics of solvent migration, phase separation occurs, and the swollen and shrunk states coexist (Figure 1.5). Phase separation has been utilized to enhance the mechanical properties, such as stiffness and toughness, of hydrogels [46, 62-66]. For example, a soft poly(acrylic acid) hydrogel containing calcium acetate, which helps form hydrophobic complexes, can be rapidly switched to a rigid plastic due to phase separation via

spinodal decomposition with its volume almost conserved, leading to tremendous enhancement of stiffness and strength [67]. Nonetheless, the effect of mechanical constraints on phase separation of hydrogels lacks systematic study.

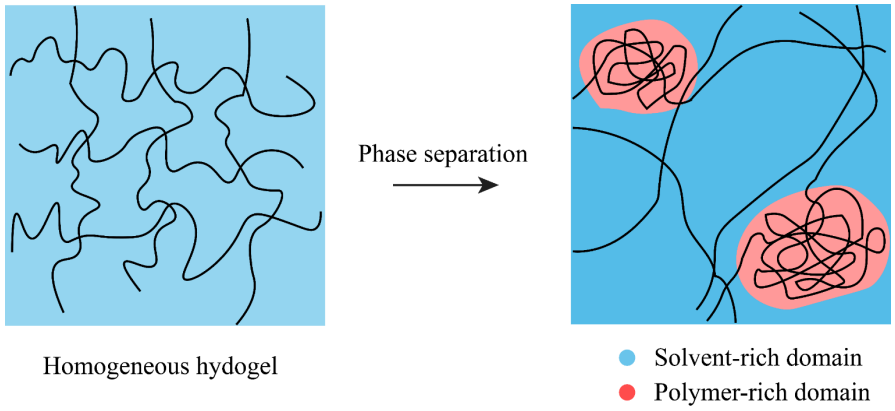

Figure 1.5 Schematic of phase separation of a hydrogel.

LCEs, coupling the liquid crystal order and elasticity, are promising materials for actuation. LCEs are typical viscoelastic materials, with mechanical responses are highly dependent on the stretching rate, as characterized by numerous experiments and models, where theoretical models for accurately predicting stress, deformation and director (liquid crystal orientation) rotation still require improvement [68-70]. Additionally, LCEs are anisotropic [71, 72], exhibiting varying fracture energies with different director distributions [73]. Few studies have examined LCE fracture, primarily focusing on measuring fracture energy through pure shear tests, with the director either parallel or perpendicular to the stretching direction [73, 74]. Their fracture behavior remains relatively unknown. Figure 1.6 shows schematic of the unconventional fracture path of LCEs.

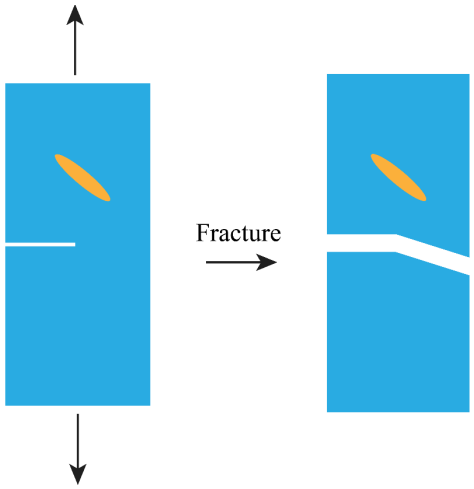

Figure 1.6 Schematic of fracture of a LCE sheet.

The lack of understanding of these phenomena presents a significant challenge for both theoretical modeling and practical applications. Studying these phenomena in different soft material systems helps to contribute to broadening the applications of soft materials.

1.4 Outline of the Dissertation

Our goal with this dissertation is to uncover the mechanisms behind mechanical instability, phase separation, and fracture in soft materials under extreme loading conditions. The dissertation comprises the following chapters.

In Chapter 2, we conduct theoretical postbuckling analysis for hyperelastic thick-walled tube structures subjected to axial compression under general three-dimensional (3D) finite deformation, and investigate the influence of geometric parameters on the postbuckling response.

In Chapter 3, we systematically study how mechanical constraints can induce the coexistence of multiple phases in hydrogels that do not exhibit phase separation under equilibrium

free swelling. We utilize the phase-field modeling to demonstrate phase separation and coexistence of hydrogels under different mechanical constraints and loading conditions.

In Chapter 4, we investigate the constitutive behavior of LCEs through a modified semisoft model, studying both elastic and viscoelastic responses. We demonstrated robust predictions of our model by comparison with experimental results.

In Chapter 5, we combine experimental and theoretical approaches to investigate fracture propagation in LCEs. Our findings reveal that crack propagation paths are highly dependent on both the initial director and the stretching rate. To further understand LCE fracture behavior, we develop a rate-dependent phase-field fracture model, which is validated through experiments and demonstrates the ability to predict complex fracture paths.

Chapter 6 concludes the dissertation.

Chapter 2 Three-dimensional Postbuckling Analysis of Thick Hyperelastic Tubes

While the buckling of tubes under axial compression has been extensively studied, the postbuckling behavior of thick tubes remains elusive. In this chapter, we conduct three-dimensional buckling and postbuckling analysis for thick hyperelastic tubes subjected to axial compression under finite deformation by the asymptotic expansion method. Our theoretical results successfully predict the deformation and stress-strain curves of buckled tubes near the critical loading, which are well validated by finite element analysis. Depending on the geometry, three kinds of postbuckling paths, including continuous buckling, snap-through and snap-back, are discovered. We summarize our results in two phase diagrams of the critical stretch for the onset of buckling and postbuckling paths with respect to the geometric parameters. In particular, we have observed that the postbuckling response can undergo a complex transition among different types of postbuckling paths, including continuous buckling, snap-through and snap-back, which is attributed to the competition between two modes of deformation, i.e., global deformation and local distortion. When a tube is long and thick, it prefers global deformation, and its cross section remains almost a plane after buckling, whereas when a tube is relatively short and relatively thin, it prefers local distortion and its cross section does not remain a plane any more after buckling. Our work provides understanding and insights into the buckling and postbuckling of thick tubes, and bridges the knowledge gap between postbuckling of thick columns and tubes.

2.1 Introduction

The theoretical study on buckling can be traced back to Euler's work, which predicts the buckling condition of slender solid columns subjected to axial compression [75]. After the onset of buckling, the applied force increases with the increase of the displacement [76]. When a column is wide, snap-through buckling occurs and the postbuckling slope of the force-displacement curve is negative, where the force decreases as the displacement increases [77]. Lubbers, van Hecke [78] developed a one-dimensional (1D) nonlinear elastic beam model to capture the transition from a positive to negative postbuckling slope with the increase of the width-to-length ratio. In contrast to the 1D beam model, Triantafyllidis, Scherzinger [79] conducted the general asymptotic analysis to study the postbuckling of two-dimensional (2D) hyperelastic wide columns subjected to compression under finite deformation. The results show that the material model and width-to-length ratio of the wide column can significantly influence the critical load and the buckling mode. Surprisingly, when the width-to-length ratio is large enough, the postbuckling response under displacement control is unstable, indicating the occurrence of snap-back buckling. More recently, we used experiments, simulations and a theoretical model to prove that when the width-to-length ratio of a column is large, the postbuckling response can be snap-through or snap-back, which is attributed to the strong coupling between bending and stretching in wide columns [39, 80]. When the column is even wider, creasing occurs before the onset of buckling [39, 81].

In contrast to the postbuckling study of 2D wide solid columns, the majority of work on the instability of hyperelastic tube structures under axial compression focuses on predicting the onset of buckling and the buckling mode. Wilkes [82] might be the first one to use the finite deformation theory to study the buckling condition of hyperelastic thick-walled tubes under axial

compression. In his work, an incompressible neo-Hookean material model was assumed, and the critical stretch for axisymmetric buckling mode was obtained by solving the linearized equations based upon a base state of finite deformation. Haughton and Ogden [83] extended the theory to a tube subjected to both uniaxial stretch and inner pressure, and the combined loading conditions, and obtained the critical onset conditions for different buckling modes. More recently, Goriely, Vandiver [84] revisited the instability of tube structures, where the critical stretch is asymptotically expanded as a function of the geometric parameter, and the transition between the Euler buckling and barreling modes was also identified. Similar predictions on buckling of hyperelastic tubes under axial compression can be found in a considerable body of literature [85, 86]. However, due to the complexity of the theory and computation, the postbuckling analysis of hyperelastic thick-walled tubes has not been solved yet. The difficulty in obtaining the postbuckling response was also highlighted by Goriely, Vandiver [84]. It is worth mentioning that Dai, Wang [87] studied the postubuckling of a hyperelastic tube under the assumption of axisymmetric deformation. They used the Blatz-Ko material model and employed the multiple-scale analysis to find the postbuckling solutions. Interestingly, they found that a thick tube can be softer than a thin tube, i.e., the postbuckling slope of a thick tube can be smaller than that of a thin tube. Nonetheless, their model cannot be applied to tubes with a wide range of thicknesses because of their limit to the axisymmetric mode. How the geometry influences the postbuckling behavior of thick-walled tubes is still not clear yet.

In this chapter, we conduct postbuckling analysis for hyperelastic thick-walled tube structures subjected to axial compression under general three-dimensional (3D) finite deformation, and investigate the influence of geometric parameters on the postbuckling response. The chapter

is organized as follows. In Section 2, we describe the geometry and material model used in this work. In Section 3, we briefly review the general asymptotic expansion method. In Section 4, we obtain the critical load and buckling mode by conducting the linear bifurcation analysis. A buckling phase diagram is plotted. In Section 5, we obtain the postbuckling response near the critical load by performing weakly postbuckling analysis. The deformed shapes and the nominal force-displacement curves are validated by finite element analysis (FEA). A postbuckling phase diagram is also constructed. Section 6 concludes the chapter.

2.2 Geometry and Material Model

Here we consider a tube under axial compression (Figure 2.1), where the stress-free configuration is taken as the reference configuration. The undeformed tube has an inner radius A, outer radius B and height H. We introduce a cylindrical coordinate, and label a material point of the tube as (R,Θ,Z) in the reference state. The tube is between two rigid and smooth plates that cannot transmit shear. We require that the displacement in the R-Θ plane of an arbitrary point at one end of the tube is the same as that of the point with the same R and Θ coordinates at the other end. The bottom plate is fixed, while the top plate is loaded in the Z direction through a displacement control. We can define the load parameter λ to be the distance of the two plates divided by their initial distance. In the deformed configuration, the position of the material point moves to (r,θ,z) by a displacement

$$\tilde{\mathbf{U}} = U_R\mathbf{e}_R + U_\Theta\mathbf{e}_\Theta + U_Z\mathbf{e}_Z . \tag{2.1}$$

Then the deformation gradient tensor can be given as

$$\mathbf{F}=\begin{bmatrix} 1+U_{R,R} & \dfrac{U_{R,\Theta}-U_{\Theta}}{R} & U_{R,Z} \\ U_{\Theta,R} & 1+\dfrac{U_{R}+U_{\Theta,\Theta}}{R} & U_{\Theta,Z} \\ U_{Z,R} & \dfrac{U_{Z,\Theta}}{R} & 1+U_{Z,Z} \end{bmatrix}. \tag{2.2}$$

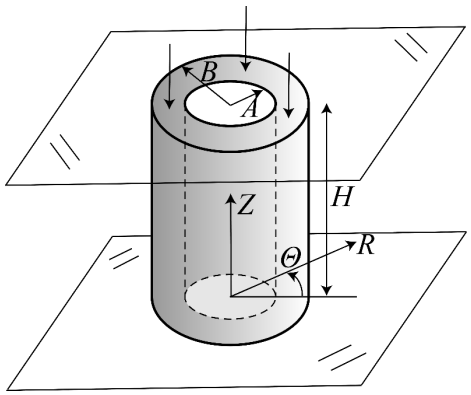

Figure 2.1 Schematics of a thick tube under axial compression.

The tube is modeled as an incompressible neo-Hookean material, which can be described by the following strain energy density function,

$$W=\frac{1}{2}\mu\left[\operatorname{tr}\left(\mathbf{F}^{T}\mathbf{F}\right)-3\right], \tag{2.3}$$

where μ is the shear modulus. The incompressibility of the material is constrained by $J=1$, where $J=\det\left(\mathbf{F}\right)$ is the Jacobian of $\mathbf{F}$.

When the tube is under a displacement-controlled loading, its total potential energy is given by

$$\Phi\left(\lambda,\mathbf{U}\right)=\int_{V}\left[W-p\left(J-1\right)\right]dV=\int_{0}^{H}\int_{0}^{2\pi}\int_{A}^{B}\left[W-p\left(J-1\right)\right]RdRd\Theta dZ, \tag{2.4}$$

where V represents the reference domain of the tube and p is a Lagrange multiplier to enforce the incompressibility of the material. We use $\mathbf{U}=\left(U_R,U_\Theta,U_Z,p\right)$ to represent the unknown displacement field, where the Lagrange multiplier is treated as a generalized displacement field.

2.3 Asymptotic Analysis

We will use the asymptotic expansion method to investigate the buckling and weakly postbuckling of a hyperelastic thick tube. In this section, we will first briefly review the theory. The more detailed derivation and explanation can be referred to the literature [76, 88-90].

Given the total potential energy in Eq. (2.4), its stationarity condition with respect to the generalized displacement is obtained as

$$\forall\delta\mathbf{U}\quad D\Phi\left(\lambda,\mathbf{U}\right)\delta\mathbf{U}=0. \tag{2.5}$$

where $\forall\delta\mathbf{U}$ with $\delta\mathbf{U}=\left(\delta U_R,\delta U_\Theta,\delta U_Z,\delta p\right)$ means an arbitrary kinematic admissible virtual displacement, and $D\Phi\left(\lambda,\mathbf{U}\right)\delta\mathbf{U}$ is the first Gateaux variation (or Gateaux derivative) of the functional Φ in the direction of $\delta\mathbf{U}$, namely,

$$D\Phi\left(\lambda,\mathbf{U}\right)\delta\mathbf{U}=\frac{d}{dt}\Phi\left(\lambda,\mathbf{U}+t\delta\mathbf{U}\right)\Big|_{t=0}. \tag{2.6}$$

A fundamental solution to Eq. (2.5) can be obtained,

$$\mathbf{U}_0\left(\lambda\right)=\left(U_{0R},U_{0\Theta},U_{0Z},p_0\right)=\left(\left(\frac{1}{\sqrt{\lambda}}-1\right)R,0,\left(\lambda-1\right)Z,\frac{\mu}{\lambda}\right), \tag{2.7}$$

which corresponds to the equilibrium homogeneous deformation of the tube.

Following the asymptotic expansion theory in the literature [76, 79, 88], we expand the load parameter λ and displacement field $\mathbf{U}$ in terms of a small parameter ξ,

$$\lambda = \lambda_c + \xi\lambda_1 + \xi^2\lambda_2 + \cdots, \tag{2.8}$$

and

$$\mathbf{U} = \mathbf{U}_0(\lambda) + \xi\mathbf{U}_1 + \xi^2\mathbf{U}_2 + \cdots, \tag{2.9}$$

where λ_c is the critical stretch for the onset of buckling. The terms $\mathbf{U}_1$ and $\mathbf{U}_2$ are restricted by the orthogonality relation

$$\langle \mathbf{U}_1, \mathbf{U}_2 \rangle \triangleq \frac{1}{|V|}\int_V U_{1i}U_{2i}dV = 0, \tag{2.10}$$

where the first equation defines the inner product of $\mathbf{U}_1$ and $\mathbf{U}_2$, $|V|$ means the volume of the tube, and U_{1i} and U_{2i} are the components of $\mathbf{U}_1$ and $\mathbf{U}_2$, respectively.

Inserting the expansions Eqs. (2.8) and (2.9) into Eq. (2.5) and setting the coefficients of the ξ, ξ^2 and ξ^3 terms equal to 0, we obtain a set of equations [76, 89]. At the order of ξ, the equation corresponds to the linear bifurcation equation, and is formulated as

$$\forall \delta\mathbf{U} \quad D^2\Phi\left(\lambda_c, \mathbf{U}_0(\lambda_c)\right)\mathbf{U}_1\delta\mathbf{U} = 0, \tag{2.11}$$

where $\mathbf{U}_1$ is the buckling mode. The critical stretch λ_c and buckling mode $\mathbf{U}_1$ can be analytically determined by solving Eq. (2.11).

At the order of ξ^2, we obtain

$$\forall \delta\mathbf{U}\; D^2\Phi\left(\lambda_c,\mathbf{U}_0\left(\lambda_c\right)\right)\mathbf{U}_2\delta\mathbf{U}+\frac{1}{2}D^3\Phi\left(\lambda_c,\mathbf{U}_0\left(\lambda_c\right)\right)\mathbf{U}_1\mathbf{U}_1\delta\mathbf{U} + \lambda_1\, d\left(D^2\Phi\left(\lambda,\mathbf{U}_0\left(\lambda\right)\right)\right)\Big/d\lambda\Big|_{\lambda_c}\mathbf{U}_1\delta\mathbf{U}=0, \tag{2.12}$$

and

$$\lambda_1=-\frac{1}{2}\frac{D^3\Phi\left(\lambda_c,\mathbf{U}_0\left(\lambda_c\right)\right)\mathbf{U}_1\mathbf{U}_1\mathbf{U}_1}{d\left(D^2\Phi\left(\lambda,\mathbf{U}_0\left(\lambda\right)\right)\right)\Big/d\lambda\Big|_{\lambda_c}\mathbf{U}_1\mathbf{U}_1}, \tag{2.13}$$

where the expression of λ_1 is obtained by setting $\delta\mathbf{U}=\mathbf{U}_1$ in Eq. (2.12) and vanishing the first term of Eq. (2.12) by Eq. (2.11).

If $D^3\Phi\left(\lambda_c,\mathbf{U}_0\left(\lambda_c\right)\right)\mathbf{U}_1\mathbf{U}_1\mathbf{U}_1\neq 0$, $\lambda_1\neq 0$ according to Eq. (2.13), and the initial postbuckling path can be determined by calculating λ_1 using Eq. (2.13) without solving Eq. (2.12). Keeping the first order term of λ and $\mathbf{U}$ in Eqs. (2.8) and (2.9), the displacement field is obtained as $\mathbf{U}=\mathbf{U}_0\left(\lambda\right)+\frac{\lambda-\lambda_c}{\lambda_1}\mathbf{U}_1$ for a given applied stretch λ. On the other hand, if $D^3\Phi\left(\lambda_c,\mathbf{U}_0\left(\lambda_c\right)\right)\mathbf{U}_1\mathbf{U}_1\mathbf{U}_1=0$, we have $\lambda_1=0$. In order to determine the displacement field, λ_2 and $\mathbf{U}_2$ need to be obtained by the higher order equations. At the order of ξ^3, we find

$$\lambda_2=-\frac{\frac{1}{6}D^4\Phi\left(\lambda_c,\mathbf{U}_0\left(\lambda_c\right)\right)\mathbf{U}_1\mathbf{U}_1\mathbf{U}_1\mathbf{U}_1+D^3\Phi\left(\lambda_c,\mathbf{U}_0\left(\lambda_c\right)\right)\mathbf{U}_1\mathbf{U}_1\mathbf{U}_2}{d\left(D^2\Phi\left(\lambda,\mathbf{U}_0\left(\lambda\right)\right)\right)\Big/d\lambda\Big|_{\lambda_c}\mathbf{U}_1\mathbf{U}_1}. \tag{2.14}$$

Making use of $D^3\Phi\left(\lambda_c,\mathbf{U}_0\left(\lambda_c\right)\right)\mathbf{U}_1\mathbf{U}_1\mathbf{U}_1=0$, we can rewrite Eq. (2.12) as

$$D^2\Phi\left(\lambda_c,\mathbf{U}_0\left(\lambda_c\right)\right)\mathbf{U}_2\delta\mathbf{U}+\frac{1}{2}D^3\Phi\left(\lambda_c,\mathbf{U}_0\left(\lambda_c\right)\right)\mathbf{U}_1\mathbf{U}_1\delta\mathbf{U}=0, \tag{2.15}$$

where $\mathbf{U}_2$ is determined by solving Eq. (2.15).

2.4 Linear Bifurcation Analysis

In this section, we conduct the linear bifurcation analysis by solving Eq. (2.11) to predict the critical stretch and buckling modes. Then we briefly discuss the influence of geometrical parameters and plot the buckling phase diagram.

2.4.1 Formulation

Since the buckling of hyperelastic tubes has been intensively studied in the literature through linear perturbation analysis [84, 86], we only briefly show how to obtain the critical stretch λ_c and buckling mode $\mathbf{U}_1=\left(U_{1R},U_{1\Theta},U_{1Z},p_1\right)$.

Integrating Eq. (2.11) by parts, we obtain a group of four partial differential equations

$$\begin{cases}\sqrt{\lambda_c}\left(U_{1R,R}\right)+\sqrt{\lambda_c}\left(\dfrac{U_{1R}+U_{1\Theta,\Theta}}{R}\right)+\dfrac{1}{\lambda_c}\left(U_{1Z,Z}\right)=0,\\ \mu\left(\dfrac{1}{R^2}-\dfrac{1}{R}\dfrac{\partial}{\partial R}-\dfrac{\partial^2}{\partial R^2}-\dfrac{1}{R^2}\dfrac{\partial^2}{\partial\Theta^2}-\dfrac{\partial^2}{\partial Z^2}\right)U_{1R}+\mu\left(\dfrac{2}{R^2}\dfrac{\partial}{\partial\Theta}\right)U_{1\Theta}+\sqrt{\lambda_c}\dfrac{\partial}{\partial R}p_1=0,\\ \mu\left(\dfrac{1}{R^2}-\dfrac{1}{R}\dfrac{\partial}{\partial R}-\dfrac{\partial^2}{\partial R^2}-\dfrac{1}{R^2}\dfrac{\partial^2}{\partial\Theta^2}-\dfrac{\partial^2}{\partial Z^2}\right)U_{1\Theta}+\mu\left(-\dfrac{2}{R^2}\dfrac{\partial}{\partial\Theta}\right)U_{1R}+\sqrt{\lambda_c}\dfrac{1}{R}\dfrac{\partial}{\partial\Theta}p_1=0,\\ \mu\left(\dfrac{\partial^2}{\partial R^2}+\dfrac{1}{R}\dfrac{\partial}{\partial R}+\dfrac{1}{R^2}\dfrac{\partial^2}{\partial\Theta^2}+\dfrac{\partial^2}{\partial Z^2}\right)U_{1Z}-\dfrac{1}{\lambda_c}\dfrac{\partial}{\partial Z}p_1=0,\end{cases} \tag{2.16}$$

where the first equation represents the incompressibility of the material.

The boundary conditions at the boundary $R = A$ and $R = B$ are

$$\begin{cases} \mu\left(U_{1R,R}\right) - \sqrt{\lambda_c}\, p_1 - \mu\left[\left(\dfrac{U_{1R} + U_{1\Theta,\Theta}}{R}\right) + \dfrac{1}{\lambda_c\sqrt{\lambda_c}}\left(U_{1Z,Z}\right)\right] = 0, \\ \mu\left(U_{1\Theta,R}\right) + \mu\left(\dfrac{U_{1R,\Theta} - U_{1\Theta}}{R}\right) = 0, \\ \mu\left(U_{1Z,R}\right) + \mu\dfrac{1}{\lambda_c\sqrt{\lambda_c}}\left(U_{1R,Z}\right) = 0, \end{cases} \tag{2.17}$$

which correspond to the stress-free condition in the R, Θ and Z directions. The boundary conditions at the boundary $Z = 0$ and $Z = H$ are

$$\begin{cases} \mu\left(U_{1R,Z}\right) + \mu\dfrac{1}{\lambda_c\sqrt{\lambda_c}}\left(U_{1Z,R}\right) = 0, \\ \mu\left(U_{1\Theta,Z}\right) + \mu\dfrac{1}{\lambda_c\sqrt{\lambda_c}}\left(\dfrac{U_{1Z,\Theta}}{R}\right) = 0, \\ U_{1Z} = 0, \end{cases} \tag{2.18}$$

which correspond to zero shear stress components, and zero displacement in the Z direction, respectively.

We introduce two functions Ω_1 and Ψ_1 to express the displacement field as

$$\begin{cases} U_{1R} = \dfrac{1}{\sqrt{\lambda_c}}\left(\Omega_{1,RZ} + \dfrac{\Psi_{1,\Theta}}{R}\right), \\ U_{1\Theta} = \dfrac{1}{\sqrt{\lambda_c}}\left(\dfrac{\Omega_{1,\Theta Z}}{R} - \Psi_{1,R}\right), \\ U_{1Z} = -\lambda_c \mathrm{M}\left(\Omega_1\right), \end{cases} \tag{2.19}$$

where $\mathrm{M}(\bullet)=\frac{1}{R}(\bullet)_{,R}+(\bullet)_{,RR}+\frac{1}{R^2}(\bullet)_{,\Theta\Theta}$ is the 2D Laplace operator in polar coordinates. The introduction of Ω_1 and Ψ_1 ensures the incompressibility condition in Eqs. (2.16) is satisfied automatically, and the rest equations in Eqs. (2.16) become

$$\begin{cases} \frac{\mu}{\lambda_c}\left(\mathrm{M}\left(\Omega_1\right)_{,RZ}+\frac{1}{R}\mathrm{M}\left(\Psi_1\right)_{,\Theta}\right)+\frac{\mu}{\lambda_c}\left(\Omega_{1,RZZZ}+\frac{\Psi_{1,\Theta ZZ}}{R}\right)-\frac{\partial}{\partial R}p_1=0, \\ \frac{\mu}{\lambda_c}\left(-R\mathrm{M}\left(\Psi_1\right)_{,R}+\mathrm{M}\left(\Omega_1\right)_{,\Theta Z}\right)+\frac{\mu}{\lambda_c}\left(\Omega_{1,\Theta ZZZ}-R\Psi_{1,RZZ}\right)-\frac{\partial}{\partial \Theta}p_1=0, \\ \mu{\lambda_c}^2\left(\mathrm{M}^2\left(\Omega_1\right)+\mathrm{M}\left(\Omega_1\right)_{,ZZ}\right)+\frac{\partial}{\partial Z}p_1=0. \end{cases} \tag{2.20}$$

The functions Ω_1, Ψ_1 and p_1 are sought in the forms

$$\begin{cases} \Omega_1\left(R,\Theta,Z\right)=\omega_1\left(R\right)\cos n\Theta\sin\eta Z, \\ \Psi_1\left(R,\Theta,Z\right)=\psi_1\left(R\right)\sin n\Theta\cos\eta Z, \\ p_1\left(R,\Theta,Z\right)=q_1\left(R\right)\cos n\Theta\cos\eta Z. \end{cases} \tag{2.21}$$

The boundary conditions (2.18) at $Z=0$ and $Z=H$ are satisfied automatically. n and $\eta=\frac{k\pi}{H}$ $\left(k=1,2,3,\cdots\right)$ are the circumferential and longitudinal wave numbers, respectively. We require the value of the parameter k to be an even number such that the displacement in the $R-\Theta$ plane of an arbitrary point at one end of the tube is the same as that of the point with the same R and Θ coordinates at the other end. Therefore, the minimum value of parameter k is 2.

The expressions of ψ_1, ω_1 and q_1 can be obtained from Eqs. (2.20), and the detailed calculations can be found in the work by Bigoni and Gei [91].

$$\begin{cases} \psi_1(R) = c_1 I_n(\eta R) + c_2 K_n(\eta R), \\ \omega_1(R) = a_1 I_n(\eta R) + a_2 I_n(\rho\eta R) + a_3 K_n(\eta R) + a_4 K_n(\rho\eta R), \\ q_1(R) = \dfrac{\mu\lambda_c{}^2}{\eta}\left(L_n^2(\omega_1) - \eta^2 L_n(\omega_1)\right), \end{cases} \tag{2.22}$$

where c_i and a_j $(i=1,2; j=1,2,3,4)$ are arbitrary constants, $I_n(\bullet)$ and $K_n(\bullet)$ are the modified Bessel functions of order n, $L_n(\bullet) = \dfrac{1}{R}(\bullet)_{,R} + (\bullet)_{,RR} - \dfrac{n^2}{R^2}(\bullet)$ is the Bessel operator, and $\rho = \lambda_c{}^{-\frac{3}{2}}$.

Using Eqs. (2.21), the displacement field can be expressed as

$$\begin{cases} U_{1R} = f_1(R)\cos n\Theta \cos\eta Z, \\ U_{1\Theta} = g_1(R)\sin n\Theta \cos\eta Z, \\ U_{1Z} = h_1(R)\cos n\Theta \sin\eta Z, \end{cases} \tag{2.23}$$

where

$$\begin{cases} f_1(R) = \dfrac{1}{\sqrt{\lambda_c}}\left(\eta\omega_1' + \dfrac{n}{R}\psi_1\right), \\ g_1(R) = \dfrac{1}{\sqrt{\lambda_c}}\left(-\dfrac{\eta n}{R}\omega_1 - \psi_1'\right), \\ h_1(R) = \lambda_c L_n(\omega_1). \end{cases} \tag{2.24}$$

Different values of n and η represent different buckling modes (Figure 2.2). Particularly, $n=0$ corresponds to axisymmetric buckling modes (Figure 2.2a).

Substituting the displacement field into the traction-free boundary conditions Eq. (2.17) at $R=A$ and $R=B$, we formulate an eigenvalue problem, which gives us the critical stretch λ_c and bifurcation modes. We denote $\mathbf{U}_1$ as

$$\mathbf{U}_1 = C\mathbf{U}_{1(a_1=1)}, \tag{2.25}$$

where $\mathbf{U}_{1(a_1=1)}$ means the displacement field $\mathbf{U}_1$ with the constant a_1 equal to 1. The undetermined parameter C will be replaced by another parameter ζ in the postbuckling analysis.

2.4.2 Results

Figure 2.2 shows schematics of two different buckling modes of tubes of different geometry, the barreling mode (Figure 2.2a) and Euler buckling mode (Figure 2.2b). The geometric parameters of a tube define two dimensionless numbers: the inner-to-outer-radius ratio, A/B, and the radius-to-length ratio, B/H. Here we will study the effect of the dimensionless geometric parameters A/B and B/H on the critical buckling condition and buckling modes.

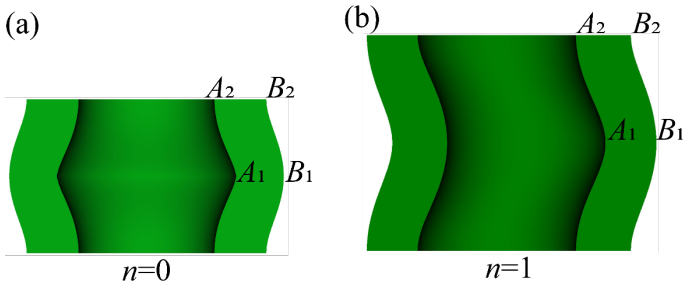

Figure 2.2 Schematics of the (a) barreling ($n = 0, k = 2$) and (b) Euler buckling ($n = 1, k = 2$) modes. The coordinates of points A_1, A_2, B_1 and B_2 in the cylindrical coordinate system (R, Θ, Z) are $(A, \Theta, H/2)$, (A, Θ, H), $(B, \Theta, H/2)$ and (B, Θ, H), respectively.

Figure 2.3a-c plot the critical stretch λ_c as a function of the dimensionless longitudinal wave number, $\eta B = k\pi B/H$, for different circumferential wave numbers, n, under three different values of radius ratio, $A/B = 0.25, 0.5, \text{and } 0.65$, respectively. In Figure 2.3a, the critical stretch

for the Euler buckling mode ($n = 1$) monotonically decreases with ηB (the black curve), indicating long-wavelength modes are preferred. The blue and cyan dashed curves correspond to the critical stretches for the buckling modes with $n = 0$ (barreling mode) and $n = 2$, respectively, which increase with ηB in the range considered, indicating the preference of short-wavelength modes in thick tubes ($A/B = 0.25$). For solid columns when $A/B = 0$, it is predicted that the barreling mode with an infinitesimal wavelength is preferred [39, 79]. The red dashed line represents the critical stretch λ_c for the onset of creasing, whose value is 0.562. The value was predicted by FEA, which is the most common way to predict the formation and evolution of creases [92-95], for the onset of creasing on the surface of an incompressible neo-Hookean solid subjected to a uniaxial loading [94, 96, 97]. Since the critical compressive strain for the onset of buckling of a short and thick tube is very large [82, 86], creases may form before the onset of buckling. This value is chosen to set the boundary between buckling and creasing in the following analysis.

By comparing the critical conditions for the different buckling modes, we can determine the highest critical stretch and the corresponding buckling mode, which should occur in reality. When A/B is fixed, the maximum critical stretch can be found among buckling modes with different circumferential wave numbers n and crease instability for a given ηB. When $A/B = 0.25$ (Figure 2.3a), the Euler buckling mode ($n = 1$) has the maximum critical stretch among buckling modes with different n and crease instability when $\eta B < 1.74$, while the crease instability has the maximum critical stretch when $\eta B > 1.74$. Therefore, Euler buckling ($n = 1$) occurs when $\eta B < 1.74$, while crease instability becomes dominant with $\eta B > 1.74$. The buckling

modes $n = 0$ and $n = 2$ never occur. For the Euler buckling mode, the critical stretch monotonically decreases as ηB increases. Therefore, for a tube with a fixed B/H, the Euler buckling mode with the lowest longitudinal wave number, namely, the largest wavelength, is preferred, which enforces the minimum ηB and maximum stretch. As a result, the value of k is always 2 and the corresponding buckling mode is similar to the schematic in Figure 2.2b. The theoretical results are validated by FEA via using the buckling analysis step (*BUCKLE keyword) in the commercial software Abaqus.

When the radius ratio A/B is increased to 0.5 (Figure 2.3b), The critical stretches for the buckling modes with $n = 0$ (barreling mode, blue curve) and $n = 2$ (cyan dashed curve) non-monotonically increase and then decrease as ηB increases, indicating the preference of a mode of an intermediate wavelength. However, whether a mode can occur or not is still determined by whether its critical stretch is the highest among other modes. The result shows that Euler buckling occurs when $\eta B < 2.80$, the barreling mode occurs when ηB ranges from 2.80 to 3.89, while the crease mode occurs when $\eta B > 3.89$. When $\eta B < 3.89$, the maximum critical stretch decreases with the increase of ηB, so the value of k should be 2 for both the Euler buckling and barreling modes. Using the relation $B/H = \eta B/(k\pi) = \eta B/(2\pi)$, we can determine that Euler buckling occurs when $B/H < 0.45$, the barreling mode occurs when B/H ranges from 0.45 to 0.62, while the crease instability occurs when $B/H > 0.62$. When $A/B = 0.65$ (Figure 2.3c), Euler buckling occurs when $\eta B < 3.13$ and the barreling mode occurs when ηB ranges from 3.13 to 5. The crease instability does not occur in the range of ηB considered here. Since the maximum critical stretch also decreases with the increase of ηB, the value of k is 2. Correspondingly, $B/H = 0.50$ is the

boundary between the onset of the Euler buckling and barreling mode. When A/B goes beyond 0.65, i.e., the wall of the tube becomes relatively thin, the $\lambda_c - \eta B$ curve for the mode $n = 2$ intersects with that of the Euler buckling mode, and moreover, the critical stretch λ_c for the Euler buckling mode changes non-monotonically with the increase of ηB [86]. This leads to richer buckling modes as B/H varies. In particular, the buckling modes with high wave numbers can occur in thin tubes, which has been reported for thin cylindrical shells [98, 99].

From these results, one can tell that a thick tube prefers a buckling mode with a small wave number, because it costs much higher energy for a thick tube to buckle with a short wavelength ($k > 2$ and $n \geq 2$) than a long wavelength ($k = 2$ and $n = 0,1$). It is worth noticing that the critical stretches for all the buckling modes asymptotically approach 0.444 [82, 86] when ηB approaches infinite; this condition is the same as the critical stretch for the onset of surface instability (wrinkling) of neo-Hookean materials under uniaxial compression, which was first determined by Biot [100]. This asymptotic stretch is smaller than the critical stretch for crease. Therefore, creasing occurs first when $\eta B \to \infty$. In addition, Euler buckling always occurs when ηB approaches 0.

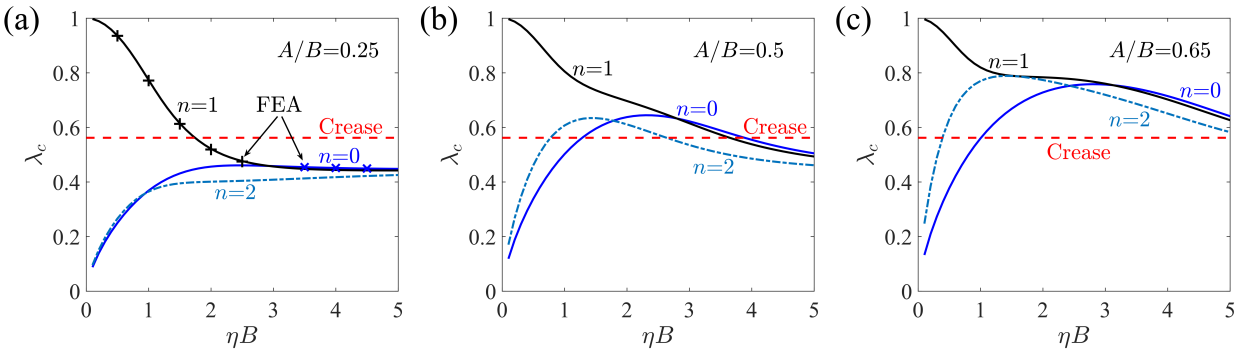

Figure 2.3 Critical stretches for different buckling modes with different longitudinal wave number n of a cylindrical tube as a function of the parameter ηB at three sets of radius ratios of the tube (a) $A/B = 0.25$, (b) $A/B = 0.5$, (c) $A/B = 0.65$.

Limiting ourselves to the barreling, Euler buckling and crease instability, we plot a phase diagram describing different instability modes in the geometric parameter range of $0.05 < A/B < 0.65$ and $0.01 < B/H < 0.95$ in Figure 2.4, where the corresponding critical stretch is represented by the color. When B/H is small, corresponding to a long tube, the Euler buckling mode occurs. When B/H is large and A/B is small, corresponding to a short and thick tube, the crease mode occurs in a wide range of the geometric parameters. When both B/H and A/B are large, corresponding to a short and relatively thin tube, the barreling mode occurs.

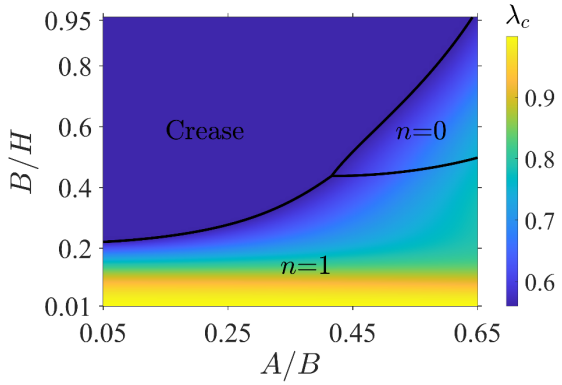

Figure 2.4 Phase diagram for the onset of buckling and creasing under axial compression. The color represents the value of the critical stretch.

2.5 Weakly Postbifurcation Analysis

In this section, we conduct postbuckling analysis near the critical loading. We first solve the high order equations. Thereafter, we predict the deformed shapes and nominal force-displacement curves and plot the postbuckling phase diagram.

2.5.1 Formulation

Using the obtained $\mathbf{U}_1$ in Eq. (2.25), we find the value of expression $D^3\Phi\left(\lambda_c,\mathbf{U}_0\left(\lambda_c\right)\right)\mathbf{U}_1\mathbf{U}_1\mathbf{U}_1$ is zero. Therefore, the calculation of λ_2 and $\mathbf{U}_2=\left(U_{2R},U_{2\Theta},U_{2Z},p_2\right)$ is required to determine the postbuckling path.

From the equation at the order of ξ^2, Eq. (2.12), another group of four partial differential equations is obtained for the unknown $\mathbf{U}_2$ as follows,

$$\begin{cases}\mu\left(\dfrac{1}{R^2}-\dfrac{1}{R}\dfrac{\partial}{\partial R}-\dfrac{\partial^2}{\partial R^2}-\dfrac{1}{R^2}\dfrac{\partial^2}{\partial\Theta^2}-\dfrac{\partial^2}{\partial Z^2}\right)U_{2R}+\mu\left(\dfrac{2}{R^2}\dfrac{\partial}{\partial\Theta}\right)U_{2\Theta}+\sqrt{\lambda_c}\dfrac{\partial}{\partial R}p_2=X_1,\\ \mu\left(\dfrac{1}{R^2}-\dfrac{1}{R}\dfrac{\partial}{\partial R}-\dfrac{\partial^2}{\partial R^2}-\dfrac{1}{R^2}\dfrac{\partial^2}{\partial\Theta^2}-\dfrac{\partial^2}{\partial Z^2}\right)U_{2\Theta}+\mu\left(-\dfrac{2}{R^2}\dfrac{\partial}{\partial\Theta}\right)U_{2R}+\sqrt{\lambda_c}\dfrac{1}{R}\dfrac{\partial}{\partial\Theta}p_2=X_2,\\ \mu\left(\dfrac{\partial^2}{\partial R^2}+\dfrac{1}{R}\dfrac{\partial}{\partial R}+\dfrac{1}{R^2}\dfrac{\partial^2}{\partial\Theta^2}+\dfrac{\partial^2}{\partial Z^2}\right)U_{2Z}-\dfrac{1}{\lambda_c}\dfrac{\partial}{\partial Z}p_2=X_3,\\ \sqrt{\lambda_c}\left(U_{2R,R}\right)+\sqrt{\lambda_c}\left(\dfrac{U_{2R}+U_{2\Theta,\Theta}}{R}\right)+\dfrac{1}{\lambda_c}\left(U_{2Z,Z}\right)=X_4.\end{cases}\tag{2.26}$$

The corresponding boundary conditions at the boundary $R=A$ and $R=B$ are

$$\begin{cases} \mu\left(U_{2R,R}\right)-\sqrt{\lambda_c}\,p_2-\mu\left[\left(\dfrac{U_{2R}+U_{2\Theta,\Theta}}{R}\right)+\dfrac{1}{\lambda_c\sqrt{\lambda_c}}\left(U_{2Z,Z}\right)\right]=X_5, \\ \mu\left(U_{2\Theta,R}\right)+\mu\left(\dfrac{U_{2R,\Theta}-U_{2\Theta}}{R}\right)=X_6, \\ \mu\left(U_{2Z,R}\right)+\mu\dfrac{1}{\lambda_c\sqrt{\lambda_c}}\left(U_{2R,Z}\right)=X_7, \end{cases} \tag{2.27}$$

where $X_i\ \left(i=1,2,\cdots,7\right)$ are functions of $\mathbf{U}_1$, which are explicitly expressed in Appendix A1.1. The boundary conditions at the boundary $Z=0$ and $Z=H$ are

$$\begin{cases} \mu\left(U_{2R,Z}\right)+\mu\dfrac{1}{\lambda_c\sqrt{\lambda_c}}\left(U_{2Z,R}\right)=0, \\ \mu\left(U_{2\Theta,Z}\right)+\mu\dfrac{1}{\lambda_c\sqrt{\lambda_c}}\left(\dfrac{U_{2Z,\Theta}}{R}\right)=0, \\ U_{2Z}=0. \end{cases} \tag{2.28}$$

In order to solve Eqs. (2.26)-(2.28), both homogeneous and particular solutions need to be found. Comparing Eqs. (2.26)-(2.28) with Eqs. (2.16)-(2.18), we can see that the homogeneous solution of $\mathbf{U}_2$ can be $\mathbf{U}_1$ multiplied by an arbitrary constant α. Making use of the restriction (2.10), the constant α should vanish.

To seek the particular solution of $\mathbf{U}_2$, we assume that $\mathbf{U}_2$ is given by

$$\begin{cases} U_{2R}=f_2^{[0]}\left(R\right)+f_2^{[1]}\left(R\right)\cos 2n\Theta+f_2^{[2]}\left(R\right)\cos 2\eta Z+f_2^{[3]}\left(R\right)\cos 2n\Theta\cos 2\eta Z, \\ U_{2\Theta}=g_2^{[0]}\left(R\right)+g_2^{[1]}\left(R\right)\sin 2n\Theta+g_2^{[2]}\left(R\right)\cos 2\eta Z+g_2^{[3]}\left(R\right)\sin 2n\Theta\cos 2\eta Z, \\ U_{2Z}=h_2^{[0]}\left(R\right)+h_2^{[1]}\left(R\right)\cos 2n\Theta+h_2^{[2]}\left(R\right)\sin 2\eta Z+h_2^{[3]}\left(R\right)\cos 2n\Theta\sin 2\eta Z, \\ p_2=q_2^{[0]}\left(R\right)+q_2^{[1]}\left(R\right)\cos 2n\Theta+q_2^{[2]}\left(R\right)\cos 2\eta Z+q_2^{[3]}\left(R\right)\cos 2n\Theta\cos 2\eta Z. \end{cases} \tag{2.29}$$

Functions $h_2^{[1]}$ and $h_2^{[0]}$ are set to be zero to ensure that the boundary conditions at the boundary $Z=0$ and $Z=H$ are satisfied automatically.

Substituting Eqs. (2.29) into Eqs. (2.26)-(2.27), we can separate Eqs. (2.26)-(2.27) into 4 groups in terms of $\cos 2n\Theta\cos 2\eta Z$, $\cos 2\eta Z$, $\cos 2n\Theta$ and 1. Noting the validity of the equations for all Θ and Z, we require all the coefficients to be zero independently, which gives us 4 groups of linear ordinary differential equations and boundary conditions. We name them as group [3], group [2], group [1] and group [0], respectively. In the main text, we only show equations of group [3]. The equations of group [2], [1] and [0] are given in Appendix A1.4, A1.6 and A1.8, respectively. For all the indices related to the displacement field $\mathbf{U}_2$, the superscripts correspond to the different groups. For brevity, $\mathbf{U}_2$ is expressed as

$$\mathbf{U}_2=\mathbf{U}_2^{[0]}+\mathbf{U}_2^{[1]}+\mathbf{U}_2^{[2]}+\mathbf{U}_2^{[3]}, \tag{2.30}$$

where $\mathbf{U}_2^{[i]}=\left(U_{2R}^{[i]},U_{2\Theta}^{[i]},U_{2Z}^{[i]},p_2^{[i]}\right)\ (i=0,1,2,3)$.

For group [3], the linear differential equations can be obtained as

$$\begin{cases}\mu\left(\dfrac{1}{R^2}-\dfrac{1}{R}\dfrac{\partial}{\partial R}-\dfrac{\partial^2}{\partial R^2}+\dfrac{4n^2}{R^2}+4\eta^2\right)f_2^{[3]}+\mu\left(\dfrac{4n}{R^2}\right)g_2^{[3]}+\sqrt{\lambda_c}\dfrac{\partial}{\partial R}q_2^{[3]}=X_1^{[3]},\\ \mu\left(\dfrac{1}{R^2}-\dfrac{1}{R}\dfrac{\partial}{\partial R}-\dfrac{\partial^2}{\partial R^2}+\dfrac{4n^2}{R^2}+4\eta^2\right)g_2^{[3]}+\mu\left(\dfrac{4n}{R^2}\right)f_2^{[3]}-\sqrt{\lambda_c}\dfrac{2n}{R}q_2^{[3]}=X_2^{[3]},\\ \mu\left(\dfrac{\partial^2}{\partial R^2}+\dfrac{1}{R}\dfrac{\partial}{\partial R}-\dfrac{4n^2}{R^2}-4\eta^2\right)h_2^{[3]}+2\eta\dfrac{1}{\lambda_c}q_2^{[3]}=X_3^{[3]},\\ \sqrt{\lambda_c}f_{2,R}^{[3]}+\sqrt{\lambda_c}\dfrac{f_2^{[3]}+2ng_2^{[3]}}{R}+\dfrac{1}{\lambda_c}2\eta h_2^{[3]}=X_4^{[3]}.\end{cases} \tag{2.31}$$

The corresponding boundary conditions at $R = A$ and $R = B$ are

$$\begin{cases} \mu\left(f_2^{[3]}{}_{,R}\right) - \sqrt{\lambda_c} q_2^{[3]} - \mu\left[\left(\dfrac{f_2^{[3]} + 2ng_2^{[3]}}{R}\right) + \dfrac{1}{\lambda_c\sqrt{\lambda_c}}\left(2\eta h_2^{[3]}\right)\right] = X_5^{[3]}, \\ \mu\left(g_2^{[3]}{}_{,R}\right) + \mu\left(\dfrac{-2nf_2^{[3]} - g_2^{[3]}}{R}\right) = X_6^{[3]}, \\ \mu\left(h_2^{[3]}{}_{,R}\right) - \mu\dfrac{1}{\lambda_c\sqrt{\lambda_c}}\left(2\eta f_2^{[3]}\right) = X_7^{[3]}. \end{cases} \tag{2.32}$$

The expressions of $X_i^{[3]}$ $\left(i = 1, 2, \cdots, 7\right)$ are listed in Appendix A1.2.

The solution to the coupled inhomogeneous ordinary differential equation set Eqs. (2.31)-(2.32) is given in Appendix A1.3. Briefly, we first decouple the equations by introducing velocity potentials and eliminating unknown functions, followed by solving the homogeneous and particular solutions of one decoupled ordinary differential equation containing one unknown function. This solution gives the displacement field of group [3]

$$\mathbf{U}_2^{[3]} = \left(U_{2R}^{[3]}, U_{2\Theta}^{[3]}, U_{2Z}^{[3]}, p_2^{[3]}\right) = \begin{pmatrix} f_2^{[3]}(R)\cos 2n\Theta\cos 2\eta Z \\ g_2^{[3]}(R)\sin 2n\Theta\cos 2\eta Z \\ h_2^{[3]}(R)\cos 2n\Theta\sin 2\eta Z \\ q_2^{[3]}(R)\cos 2n\Theta\cos 2\eta Z \end{pmatrix}^T. \tag{2.33}$$

The solutions of the displacement field to the equations of group [2], [1] and [0] are derived in Appendix A1.5, A1.7, and A1.9, respectively.

The second order displacement field $\mathbf{U}_2$ can be denoted as

$$\mathbf{U}_2 = C^2\mathbf{U}_{2(a_1=1)}. \tag{2.34}$$

Substituting Eqs. (2.25) and (2.34) into Eq. (2.14), we can obtain

$$\lambda_2 = C^2 \lambda_{2(a_1=1)}, \tag{2.35}$$

where $\lambda_{2(a_1=1)}$ means the value of λ_2 when the constant a_1 equals to 1.

Substituting $\lambda_1 = 0$ and Eq. (2.35) into Eq. (2.8), λ is expressed as

$$\lambda = \lambda_c + \left(\xi C\right)^2 \lambda_{2(a_1=1)} + \cdots . \tag{2.36}$$

Defining another parameter $\zeta = \xi C$ and keeping the second order of expansion λ in Eq. (2.8), we can rewrite Eq. (2.36) as

$$\lambda = \lambda_c + \zeta^2 \lambda_{2(a_1=1)} . \tag{2.37}$$

Similarly, the displacement field can be written as

$$\mathbf{U} = \mathbf{U}_0 \left(\lambda\right) + \zeta \mathbf{U}_{1(a_1=1)} + \zeta^2 \mathbf{U}_{2(a_1=1)} . \tag{2.38}$$

From Eq. (2.37), the parameter ζ can be obtained for a prescribed λ. Then substituting ζ into Eq. (2.38), the displacement field $\mathbf{U}$ can be obtained. Once the displacement field is known, the weakly postbuckling problem is solved. Substituting $\mathbf{U}$ into Eq. (2.2), the deformation gradient can be calculated.

Specially, if the value of $\lambda_{2(a_1=1)}$ is negative, then $\zeta = \sqrt{\frac{\lambda_c - \lambda}{-\lambda_{2(a_1=1)}}}$ according to Eq. (2.37), and λ is smaller than λ_c, which makes the bifurcation supercritical. When the value of $\lambda_{2(a_1=1)}$ is positive, $\zeta = \sqrt{\frac{\lambda - \lambda_c}{\lambda_{2(a_1=1)}}}$ and the bifurcation is subcritical.

We define the normalized average nominal compressive stress as

$$s = -\frac{1}{\mu\pi\left(B^2 - A^2\right)} \int_0^{2\pi} \int_A^B \left(\frac{\partial W}{\partial \mathbf{F}} - p\mathbf{F}^{-T} \right)_{33} R dR d\Theta, \tag{2.39}$$

where the negative sign means the tube is under compression, and s is its magnitude. We define the nominal compressive strain as

$$\varepsilon = 1 - \lambda . \tag{2.40}$$

We further define the normalized postbukling slope based on the nominal strain and stress as

$$S = \lim_{\varepsilon \to \varepsilon_{cr}} \frac{s - s_{cr}}{s_{cr}\left(\varepsilon - \varepsilon_{cr}\right)}, \tag{2.41}$$

where ε_{cr} and s_{cr} are the critical strain and stress for the onset of buckling, and stress s and strain ε are beyond the buckling point.

The postbuckling analysis is still valid for the barreling mode by setting n as 0, which is discussed in the Appendix A1.10.

2.5.2 Results

We first compare the morphology of a tube in postbuckling predicted by the asymptotic theory and FEA to validate the theory (Figure 2.5). For the FEA, Riks method is used in Abaqus. To trigger the instability, we introduce into the perfect geometry a small imperfection in the shape of the buckling mode obtained from the linear perturbation with an amplitude less than 10^{-5} times the thickness of the tube. The results are compared at a fixed applied stretch, which is chosen as $\lambda = 1 - 1.01\varepsilon_{cr}$ if the value of $\lambda_{2(a_1=1)}$ is negative, while which is chosen as $\lambda = 1 - 0.99\varepsilon_{cr}$ if $\lambda_{2(a_1=1)}$ is positive. For a tube with $A/B = 0.6$ and $B/H = 0.2$, both the linear bifurcation theory and FEA predict the Euler buckling mode occurs, the critical stretch is 0.7872, and the value of $\lambda_{2(a_1=1)}$ is positive. Figure 2.5a shows the 3D buckled shape of the tube at $\lambda = 0.7894$ in a cross-sectional view in Θ=0 and π plane from FEA. The deformed shape of the cross section originally in the horizontal plane $Z = 0.25H$ in the reference configuration (Figure 2.5b) is projected to the plane $z = 0.25\lambda H$ in the current configuration, with the color showing the relative displacement defined as $\Delta U_Z = U_Z + (1 - \lambda)Z$ (Figure 2.5d-e). The predicted deformation by the theory (Figure 2.5e) agrees well with that by FEA (Figure 2.5d). Similarly, the deformed shape of vertical RZ cross section originally in $\Theta = 0$ and $\Theta = \pi/4$ planes (Figure 2.5c) is projected to the plane $\theta = 0$ and $\theta = \pi/4$, respectively, in the current configuration, where the projection distance defined as $\Delta U_\Theta = U_\Theta$ is represented by the color shown in Figure 2.5f-i.

For a tube with $A/B = 0.6$ and $B/H = 0.6$, the theory predicts that the barreling mode occurs, the critical stretch is 0.6727, and the value of $\lambda_{2(a_1=1)}$ is also positive. Figure 2.6b shows the predicted vertical cross section at $\lambda = 0.6760$, which agrees well with the FEA results (Figure

2.6a). The distorted mesh shows that the tube undergoes large shear deformation, due to the large thickness-to-length ratio.

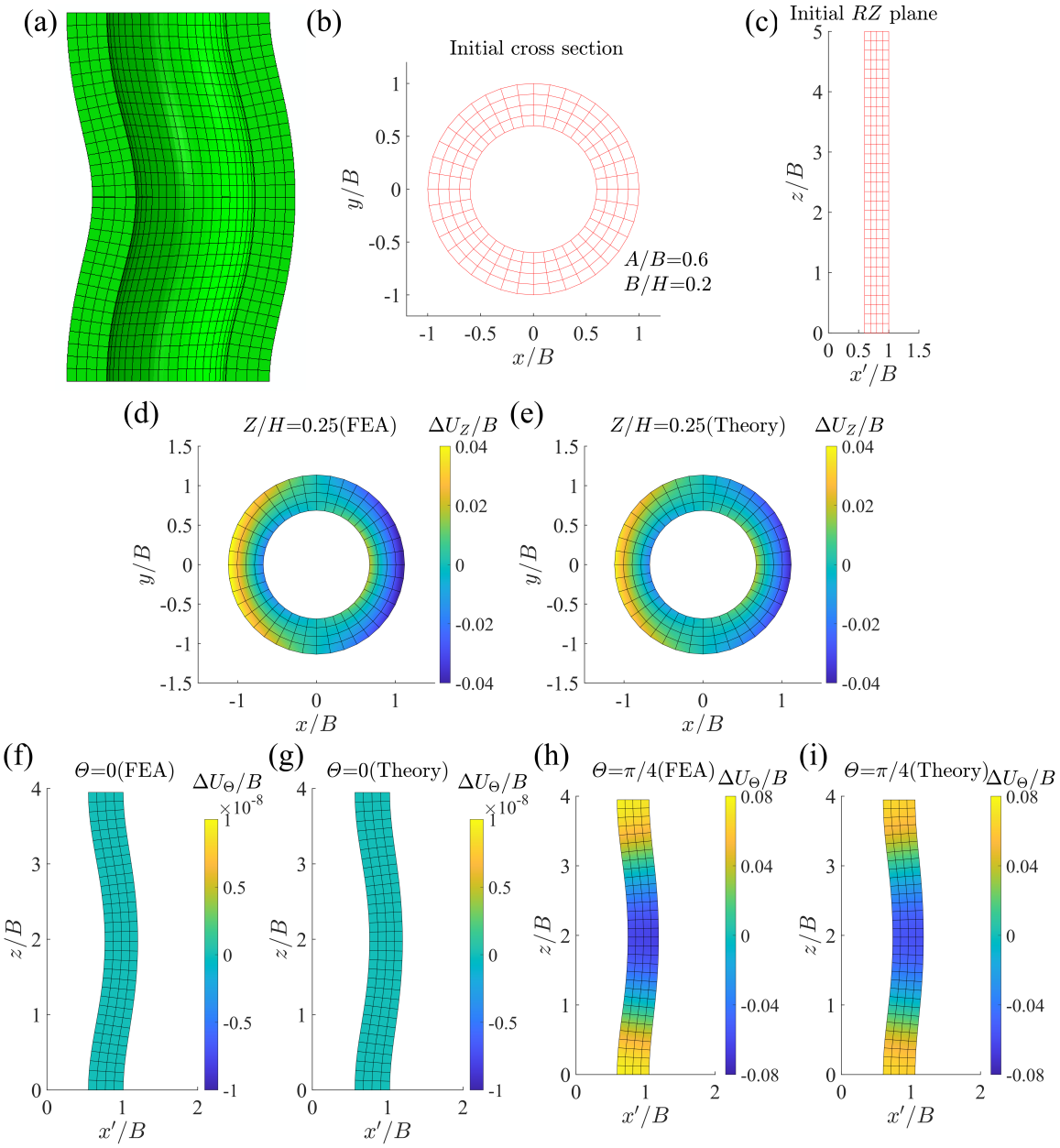

Figure 2.5 Comparing the deformed shape of the Euler buckling mode predicted by the asymptotic expansion method with that from the FEA for a tube with $A/B = 0.6$ and $B/H = 0.2$ at applied

stretch $\lambda = 1 - 0.99\varepsilon_{cr} = 0.7894$. (a) FEA result of 3D buckled shape in a cross-sectional view in $\Theta = 0$ and π plane. (b) The initial $R\Theta$ plane (horizontal cross section) with a constant Z is meshed uniformly. (c) The initial RZ plane (vertical cross section) with a constant Θ is meshed uniformly. (d) The FEA and (e) theoretical results of the projection of the deformed horizontal cross section (originally in $Z = 0.25H$) to the current plane $z = 0.25\lambda H$, where the color represents the projection distance. The projection of the deformed vertical RZ cross section (f-g) originally in $\Theta = 0$ to the current plane $\theta = 0$, and (h-i) originally in $\Theta = \pi/4$ to the current plane $\theta = \pi/4$, where (f) and (h) are FEA results and (g) and (i) are theoretical results.

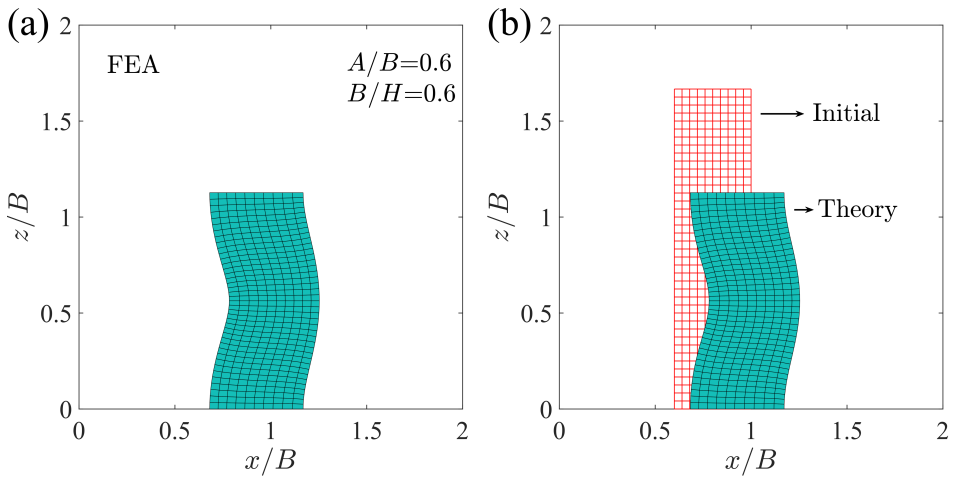

Figure 2.6 Comparing the deformed shape of the barreling mode predicted by the asymptotic expansion method with the FEA results for a tube with $A/B = 0.6$ and $B/H = 0.6$ at applied stretch $\lambda = 1 - 0.99\varepsilon_{cr} = 0.6760$. (a) The FEA result and (b) theoretical result of the deformed shape of a RZ plane, with the initial state plotted for reference.

We then keep track of the current coordinates along R direction normalized by the coordinates in the reference state, r/R, of points A_1, A_2, B_1 and B_2, which are labeled in Figure

2.2, as nominal strain ε increases for tubes with $A/B = 0.6$ and B/H varying from $0.1, 0.2, 0.48$ to 0.6, where the green dashed curve represents the homogenous soluion, the solid curves are predicted by the theory and the dots are FEA results (Figure 2.7). For $B/H = 0.1$ (Figure 2.7a) and $B/H = 0.2$ (Figure 2.7b), the Euler buckling mode is predicted, and we show the coordinates of the points in the RZ plane with $\Theta = 0$ in the initial configuration. For $B/H = 0.48$ (Figure 2.7c) and $B/H = 0.6$ (Figure 2.7d) the axisymmetric barreling mode is predicted, and the coordinates in an arbitrary plane are plotted. As Figure 2.7 shows, the normalized coordinates of points A_1, A_2, B_1 and B_2 initially coincide with the homogenous solution as the applied strain increases. Upon a critical strain, the tube buckles and the normalized coordinates deviate from the homogenous solution. For both the Euler buckling and barreling modes, taking point A_1 as an example, the coordinate can increase with either the increase or decrease of the nominal strain after the onset of buckling, which corresponds to the supercritical (Figure 2.7a and c) or subcritical (Figure 2.7b and d) bifurcation, respectively. The theoretically predicted normalized coordinates for all four cases agree well with the FEA results.

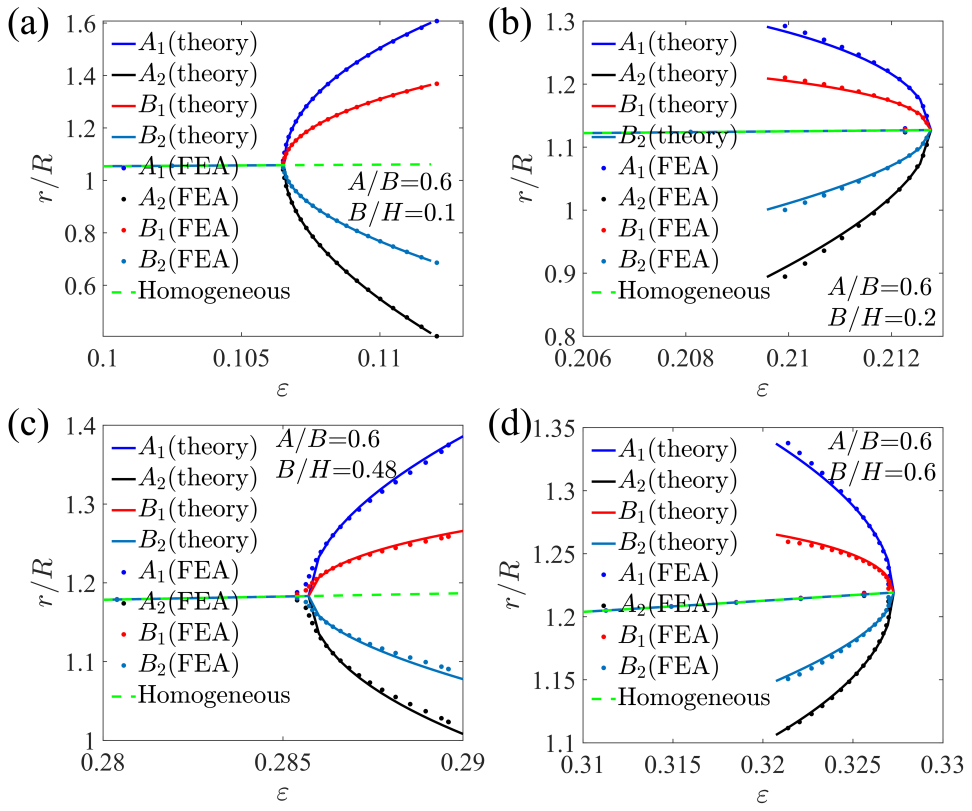

Figure 2.7 Normalized coordinates of points A_1, A_2, B_1 and B_2 along R direction, r/R, as a function of nominal strain, ε, for fixed $A/B = 0.6$ and different B/H: (a) $B/H = 0.1$; (b) $B/H = 0.2$; (c) $B/H = 0.48$ and (d) $B/H = 0.6$. For (a) and (b), the Euler buckling mode is predicted, and the coordinates are shown in the vertical cross section originally in the plane $\Theta = 0$. For (c) and (d), the axisymmetric barreling mode is predicted.

We further calculate the average nominal stress by Eq. (2.39). Figure 2.8 shows the average nominal stress-strain curves of tube structures under axially compression in the vicinity of the buckling point. We fix $A/B = 0.6$, and widely vary B/H from $0.02, 0.1, 0.2, 0.48$ to 0.6 (Figure 2,8 and 9). Although, Euler buckling occurs in all the tubes with $B/H = 0.02, 0.1, 0.2$, different postbuckling paths are predicted. In Figure 2.8a ($B/H = 0.02$), after the tube buckles, both the

nominal stress and strain increase, the postbuckling response of which is called continuous buckling. In Figure 2.8b ($B/H = 0.1$), after the tube buckles, the nominal stress decreases while the strain increases along the equilibrium path, which is called snap-through buckling. In Figure 2.8c ($B/H = 0.2$), after the tube buckles, both the nominal stress and strain decrease, which is called snap-back buckling. The increasing strain corresponds to a negative value of $\lambda_{2(a_1=1)}$, while the decreasing strain corresponds to a positive value of $\lambda_{2(a_1=1)}$. Therefore, the postbuckling response can be either supercritical or subcritical. When the tube becomes shorter, i.e., B/H is increased to 0.48 and 0.6, the barreling mode occurs. The corresponding average nominal stress-strain curves are shown in Figure 2.9. A snap-through buckling path is predicted for $B/H = 0.48$, while a snap-back buckling path is predicted for $B/H = 0.6$. For all the above mentioned cases, no matter the Euler buckling or barreling mode occurs, the theoretical results of the average nominal stress-strain relations in the weakly postbuckling region agree very well with the FEA results.

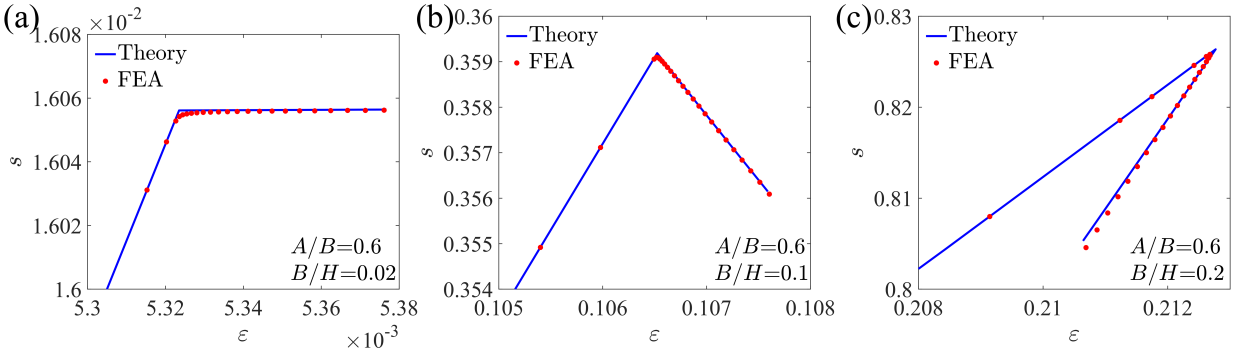

Figure 2.8 The postbuckling stress-strain relation for axially compressed tubes with fixed $A/B = 0.6$ and different B/H: (a) $B/H = 0.02$, (b) $B/H = 0.1$, (c) $B/H = 0.2$. The corresponding buckling mode is Euler buckling.

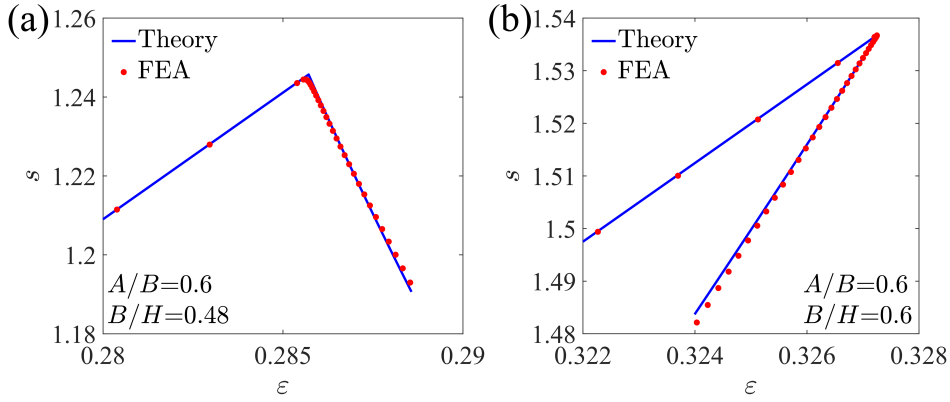

Figure 2.9 The postbuckling stress-strain relation for axially compressed tubes with fixed $A/B = 0.6$ and different B/H: (a) $B/H = 0.48$, (b) $B/H = 0.6$. The corresponding buckling mode is the barreling mode.

The postbuckling slope is calculated by Eq. (2.41) and plotted in Figure 2.10. When we fix $B/H = 0.2$, and vary A/B from 0.15 to 0.55, Euler buckling always occurs (Figure 2.10a). As A/B increases from 0.15 to 0.254, the slope first increases from a positive value to positive infinite. At $A/B = 0.254$, the slope changes from positive infinite to negative infinite, indicating the transition of the postbuckling path from snap-back to snap-through. When A/B increases from 0.254 to 0.479, the postbuckling slope remains negative, and the postbuckling path remains snap-through. At $A/B = 0.479$, the postbuckling slope transits from negative infinite to positive infinite, indicating a transition of the postbuckling path from snap-through to snap-back again.

Then we fix $A/B = 0.6$, and vary B/H from 0.01 to 0.8 (Figure 2.10b). Euler buckling occurs when B/H is between 0.01 and 0.474, while barreling mode exists when B/H is between 0.474 and 0.8. Within the Euler buckling range, the slope first gradually decreases from positive to zero when B/H increases from 0.01 to 0.033, where the postbuckling path is continuous. As B/H further increases from 0.033 to 0.131, the postbuckling slope decreases from zero to negative infinite, and the postbuckling path is snap-through. At $B/H = 0.131$ and $B/H = 0.431$, the postbuckling slope transits from negative infinite to positive infinite, indicating a transition of the postbuckling path from snap-through to snap-back, whereas at $B/H = 0.325$, the postbuckling slope transits from positive infinite to negative infinite, indicating a transition of the postbuckling path from snap-back to snap-through. The postbuckling slope flips its sign multiple times, demonstrating complex postbuckling behaviors as the geometric parameters vary. Within the barreling range, at $B/H = 0.516$, the postbuckling slope transits from negative infinite to positive infinite, indicating the transition of the postbuckling path from snap-through to snap-back.

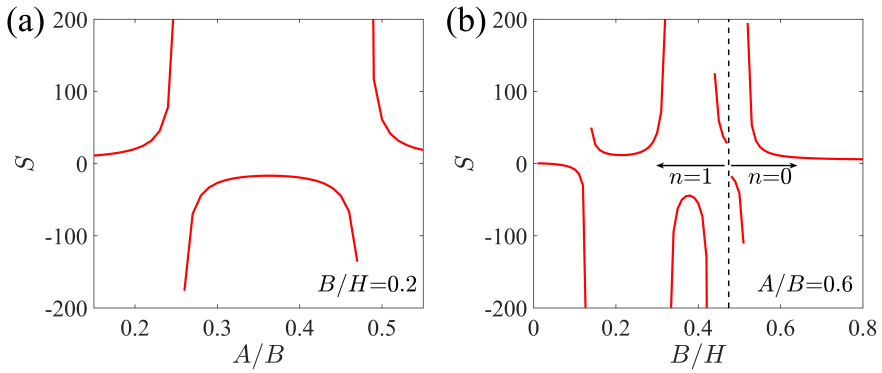

Figure 2.10 Postbuckling slopes as functions of geometric parameters (a) A/B ($B/H = 0.2$) and (b) B/H ($A/B = 0.6$).

To thoroughly investigate the influence of parameters A/B and B/H on the postbuckling path, a phase diagram of the postbuckling path is plotted (Figure 2.11). In the diagram, we use letters "C", "T" and "B" to represent different phases, i.e., different types of postbuckling path, continuous buckling, snap-though and snap-back, respectively, with black curves demarcating the different phases. When B/H is small, less than 0.02, a tube can be treated as a traditional slender column. Correspondingly, the buckling mode is Euler buckling, and the continuous buckling path occurs in the entire range of A/B from 0.05 to 0.65. When B/H becomes larger, snap-through Euler buckling occurs. When A/B is smaller than 0.477, with further increase of B/H, snap-back Euler buckling occurs. However, when A/B is larger than 0.477, there is another island of snap-back Euler buckling surrounded by the snap-through Euler buckling. As a result, when B/H increases while A/B is fixed (e.g., B/H is varied from 0.01 to 0.474, while A/B is fixed as 0.6), although the buckling mode remains Euler buckling, the postbuckling path can undergo a complex transition from continuous, snap-through, snap-back, to snap-through, and finally back to snap-back; the corresponding postbuckling slope is shown in Figure 2.10b. In the region where the barreling mode exists, when A/B increases while B/H is fixed (e.g., A/B increases from 0.48 to 0.65, while B/H is fixed as 0.55), the postbuckling path transits from snap-back to snap-through. When A/B is fixed (e.g., $A/B = 0.6$), the postbuckling slope as a function of B/H is shown in Figure 2.10b.

To understand the transition from continuous, snap-through to snap-back Euler buckling, in our previous work (Chen and Jin [39]), a discrete model was established to predict the buckling of wide columns. By assuming that the cross section of a column remains a plane after buckling, the discrete model reveals that the coupling between the stretching and bending energy leads to

the snap-through and snap-back buckling. As the width-to-length ratio increases, the ratio of the bending to stretching energy increases, and the column can undergo a transition from continuous, snap-through to snap-back buckling. When A/B of a tube is very small, B/H becomes the only dimensionless geometric parameter, so the buckling behavior of the tube shows similar dependence on B/H to that on the width-to-length ratio of a solid cylinder. However, when A/B is large, the buckling behavior is more complex. For a long and relatively thin tube, i.e., A/B is large and B/H is small, its cross-section approximately remains a plane after buckling (Figure 2.12a). Therefore, the tube still undergoes a transition from continuous, snap-through to snap-back as B/H increases. However, in a relatively short and relatively thin tube, i.e., when both A/B and B/H are large, although Euler buckling still occurs, the cross section does not remain a plane anymore during buckling, but undergoes a complex local distortion (Figure 2.12b). Essentially, the tube behaves like two solid columns connected in parallel, with $(B-A)/H$ as the effective width-to-length ratio, which leads to another transition from the snap-through to snap-back Euler buckling. Consequently, the competition between the two deformation modes, i.e., the global deformation vs local distortion, gives rise to the complex postbuckling behavior of a tube with relatively large A/B, i.e., an island of snap-back buckling is formed and surrounded by the snap-through buckling in the phase diagram.

Noticing that in the Euler buckling region, there is one boundary between the continuous buckling and snap-through buckling ("C"-"T") and another boundary between the snap-through and snap-back buckling ("T"-"B") other than the boundary of the island of the snap-back buckling. The phase diagram shows that across the "C"-"T" boundary under fixed B/H, a thinner tube tends to undergo snap-through buckling. In such a case, the tube is long and prefers the global

deformation. Therefore, the increase of A/B increases the ratio of the bending to stretching energy, leading to the transition from continuous buckling to snap-through buckling at lower B/H. In contrast, across the "T"-"B" boundary under fixed B/H, a thicker tube tends to undergo snap-back buckling. In this case, the tube is short and prefers local distortion, i.e., it behaves like two solid columns connected in parallel. As a result, a thicker tube gives rise to a larger effective width-to-length ratio, leading to the transition from the snap-through and snap-back instability at lower B/H.

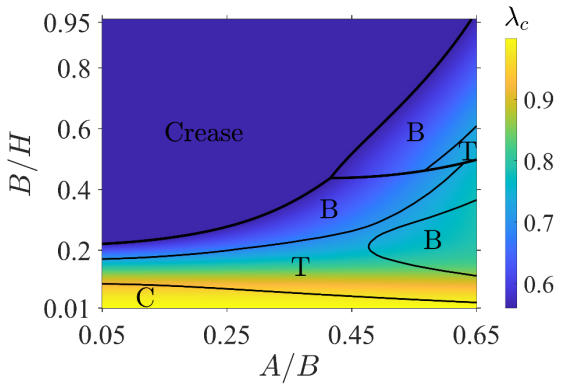

Figure 2.11 Phase diagram for different types of postbuckling paths. In this diagram, we use letters "C", "T" and "B" to represent continuous buckling, snap-though and snap-back, respectively. The color contour represents the value of the critical stretch λ_{cr}.

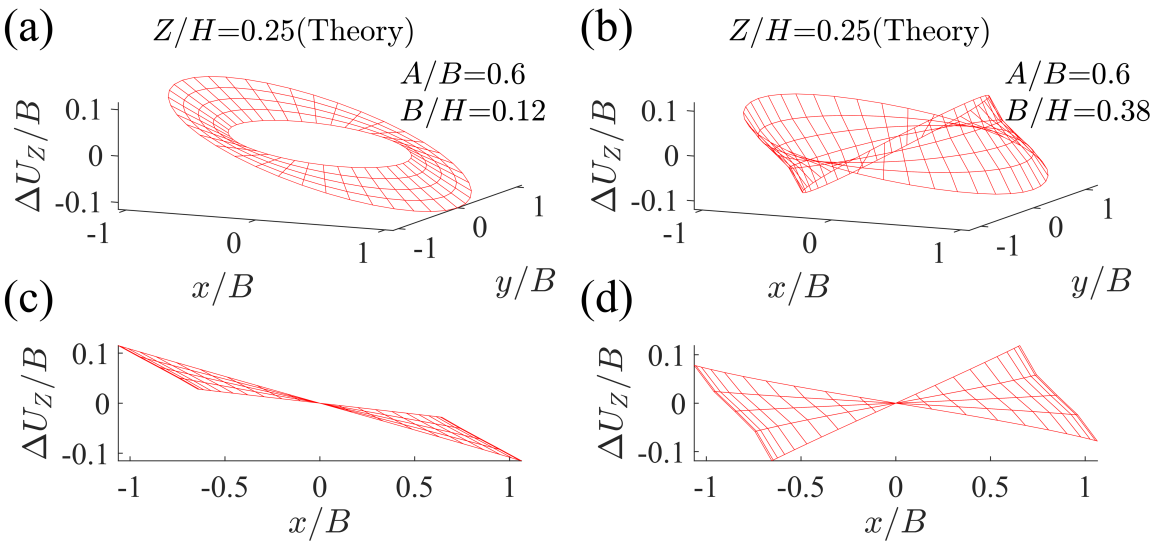

Figure 2.12 (a) (b) 3D plots and (c) (d) side views of the deformed cross section (originally in $Z = 0.25H$) at applied stretch $\lambda = 1 - 1.01\varepsilon_{cr}$ when A/B is fixed at 0.6, and (a) (c) $B/H = 0.12$, or (b) (d) $B/H = 0.38$. For both tubes, snap-through Euler buckling occurs.

2.6 Conclusion

In this work, we conduct buckling and postbuckling analysis for axially compressed thick hyperelastic tubes under finite deformation by the asymptotic expansion method. Depending on the inner-to-outer radius ratio, A/B, and radius-to-length ratio, B/H, the buckling mode can be the Euler buckling or barreling mode. A phase diagram for the critical onset stretch of buckling is constructed for the different buckling modes. The result shows that when a tube is relatively long, it prefers the Euler buckling mode, while when it is short, either crease or barreling occurs, depending on the inner-to-outer radius ratio.

Our postbuckling analysis successfully predicts the deformed shapes, the displacement fields, and the stress-strain curves of buckled tubes near the critical loading, which are well

validated by FEA. In particular, the postbuckling slope of the stress-strain curve is calculated. Depending on the geometry, three kinds of postbuckling paths, the continuous buckling, snap-through and snap-back, are discovered for the Euler buckling mode, and two kinds of postbuckling paths, the snap-through and snap-back paths, are discovered for the barreling mode. A phase diagram of different postbuckling paths is further constructed with respect to the geometric parameters. As the geometric parameters vary, the postbuckling response can transit among different types of paths, which are attributed to the competition between the global deformation and local distortion. In particular, when a tube is long and thick, it prefers global deformation, and its cross section remains almost a plane after buckling, whereas when a tube is relatively short and relatively thin, it prefers local deformation and its cross section does not remain a plane any more after buckling. This work provides insights into the buckling and postbuckling of thick tubes, bridges the knowledge gap between postbuckling of thick columns and tubes, and lays foundations for the design of tube structures and hollow-tube lattices.

Yet, this theoretical analysis is limited to perfect tubes. In practical applications, imperfections are inevitable, and can have substantial influences on the buckling and postbuckling behavior of tubes. It is known that subcritical bifurcations are particularly sensitive to imperfections [90, 101]. We demonstrate in Appendix A1.11 using FEA that when an imperfection exists in a tube, the critical stress is reduced for snap-through buckling, and both the critical stress and critical strain are reduced even more significantly for snap-back buckling. Moreover, snap-back buckling can transit to a snap-through buckling, when the imperfection has a large enough amplitude [102, 103], or a small imperfection is added to a tube with geometric parameters close to the boundaries of snap-through and snap-back buckling. As a result, the phase boundaries of

both phase diagrams of buckling and postbuckling can be shifted by geometric imperfections. However, theoretical postbuckling analysis of imperfect thick tubes under finite deformation is extremely challenging, and is left to be studied in the future. Other than the geometric imperfections, knowing the influence of boundary conditions on the buckling and postbuckling behavior of tubes is important for practical applications of tubes. It is expected that the boundary condition can affect the buckling modes and postbuckling paths, particularly for short tubes. In our model, we do not consider shear stresses at the two ends of the tube. More realistic boundary conditions, such as the fixed boundary condition and including friction at the two ends, could be considered. Nonetheless, such boundary conditions lead to difficult theoretical analysis since the tube undergoes inhomogeneous deformation before the onset of buckling, which are to be addressed as future work.

Chapter 3 Mechanics Underpinning Phase Separation of Hydrogels

This chapter reveals the underpinning role of mechanical constraints and dynamic loading on triggering volume phase transitions and phase separation of hydrogels. Using the Flory-Rehner free energy that does not predict phase separation of hydrogels under equilibrium free swelling, we show that mechanical constraints can lead to coexistence of multiple phases. We systematically obtain the states of equilibrium for hydrogels under various mechanical constraints, and unravel how mechanical constraints change the convexity of the free energy and monotonicity of the stress-stretch curves, leading to phase coexistence. Using a phase-field model, we predict the pattern evolution of phase coexistence, and show many features cannot be captured by the homogeneous states of equilibrium due to large mismatch stretch between the coexisting phases. We further reveal that the system size, quenching rate, and loading rate can significantly influence the phase behavior, which provides insights for experimental studies related to morphological patterns of hydrogels.

3.1 Introduction

Volume phase transitions and phase separation of hydrogels have been experimentally demonstrated in various hydrogels [104]. Tanaka et al. found that neutral polyacrylamide (PAAm) hydrogels immersed in a basic solution can become polyelectrolyte hydrogels via hydrolysis [105, 106]. While neutral PAAm hydrogels undergo a continuous volume change with the acetone concentration, the resultant polyelectrolyte hydrogels in an acetone solution can undergo a discontinuous volume transition by changing the acetone concentration, which is attributed to the osmotic pressure of dissociated hydrogen ions [105]. Hirokawa and Tanaka reported that neutral

poly(N-isopropylacrylamide) (PNIPAM) hydrogels immersed in water could also exhibit a volume phase transition by changing temperature [107]. Shen et al. demonstrated that blisters form on the surface of neutral PNIPAM hydrogels when they are subjected to heating, where an impermeable skin layer is formed during phase separation, and water fills into the defects under the skin layer, forming inflated blisters [108]. When subjected to heating, a neutral PNIPAM hydrogel cylinder shows coexistence of swollen and shrunk phases along the radial direction, while a weakly ionized PNIPAM hydrogel cylinder shows phase coexistence along the axial direction [109, 110].

Most theoretical studies on the volume phase transition of hydrogels are based on double-well free energy. Cai and Suo successfully demonstrated a volume phase transition of thermo-responsive hydrogels by obtaining the state of equilibrium through minimizing a properly constructed free energy function, and predicted phase coexistence based on the assumption of a sharp interface between the swollen and shrunk phases [111]. A continuum field theory was developed by Yu et al. to predict the volume phase transition of polyelectrolyte hydrogels induced by changing the salt concentration of an external solution [112]. The above models are based on the Flory-Rehner theory, where the Flory-Huggins interaction parameter χ, describing the interaction between a polymer and a solvent, is modelled as a function of the polymer volume fraction to obtain double-well free energy, thus, to capture the phase coexistence and the discontinuous volume change [55]. Considering a sharp interface between the swollen and shrunk phases of a one-dimensional cylindrical or spherical hydrogel, Tomari and Doi numerically studied the kinetic process of the hydrogel undergoing a volume phase transition [113-115]. By the introduction of interfacial energy and kinetics of diffusion, a phase-field model was developed to simulate the evolution of different phases and interfaces under two-dimensional deformation using

a double-well free energy [116]. Bao et al. utilized the phase-field model with proposed new free energy including the processes of detachment of polymer chains from and reattachment onto crosslinks to simulate the three-dimensional morphology evolution of nanocomposite hydrogels during a phase separation process [117].

Of particular interest is the influence of mechanical constraints on phase transitions and phase separation of hydrogels. Although it is well known that PAAm hydrogels do not have volume phase transitions under free swelling, Matsuo and Tanaka found that subjected to different axial stretches, PAAm hydrogels immersed in an acetone solution show different shapes and phase separation patterns [43]. In particular, an impermeable skin layer forms on the surface of a PAAm hydrogel cylinder, which provides extra mechanical constraints [43]. Based on the Flory-Rehner model with a constant Flory-Huggins interaction parameter χ, Hennessy et al. studied phase separation of a hydrogel under constrained uniaxial deformation, i.e. free deformation in one-dimension but constrained in the other two dimensions. They found that a volume phase transition cannot occur when the hydrogel is in equilibrium with a solvent of zero chemical potential, but two phases can coexist when the hydrogel is in equilibrium with a solvent of higher chemical potential [118, 119]. Cirillo et al. predicted that when a hydrogel is subjected to a pressure load, a swollen and a shrunk phase only coexist under constrained uniaxial deformation, instead of constrained biaxial or three-dimensional volumetric deformation [120]. Contradictorily, Duda et al. theoretically showed that hydrogels under hydrostatic loading could have multiphase equilibria, which indicates the possibility of a volume phase transition [121]. Yamamoto et al. predicted that composite hydrogels with cofacially aligned nanosheets could undergo discontinuous deformation with a constant volume [122-124]. The above models are based on the Flory-Rehner free energy

with the parameter χ independent of polymer concentration, which is not double-well, and consequently, no volume phase transition can be predicted under free swelling. However, the introduction of mechanical constraints changes the total free energy, leading to possible phase coexistence. It's worth mentioning that Dušková-Smrčková and Dušek showed that the volume phase transition can be either induced or suppressed by expansive and compressive strain [125]. Though the above-mentioned theoretical works based on the Flory-Rehner model with a constant Flory-Huggins interaction parameter χ show possible phase transitions of hydrogels under certain constraints [118, 120, 121], they focus on the equilibrium states under one specific stress state or chemical potential loading, and some of the results seem even contradictory. This chapter will systematically investigate the effect of mechanical constraints on the equilibrium states based on single-well Flory-Rehner free energy. We will not only identify the conditions for existence of multiple homogeneous equilibrium states, but also use the phase field model to demonstrate the pattern evolution of phase coexistence. Our results will show that the predicted multiple homogeneous equilibrium states cannot always well represent the swollen and shrunk phases in phase separation, attributed to the large stretch mismatch between the two separated phases.

Phase separation of hydrogels is limited by the diffusion process of solvent molecules, and therefore loading rates can also play an important role in the phase behavior. When subjected to different heating rates, PNIPAM hydrogels could show different phase morphologies, including the fine and coarse surface patterns, and the bubble pattern [109, 110]. Chang et al. demonstrated that a toroid-shaped PNIPAM hydrogel subjected to slow heating remains toroidal shape, while the hydrogel subjected to rapid heating buckles and undergoes mechanical instability [126]. Considering the kinetics of diffusion, Hennessy et al. have shown that temporary phase separation

can occur in a neutral hydrogel under free swelling by quenching it through a sudden increase of the interaction parameter χ [127]. However, how a quenching rate, which is different from the diffusion time scale, affects the texture and morphology of phase-separated hydrogels still needs to be investigated. In addition, when a hydrogel is mechanically loaded, the influence of stretching rates on its phase separation is yet to be explored. To address the above questions, we utilize the phase-field modeling to demonstrate phase separation and coexistence of hydrogels under different mechanical constraints and loading conditions. The influence of system size, stretching rate and quenching rate on the volume phase transition and phase separation of hydrogels will be studied.

In this chapter, we first briefly introduce the constitutive models of hydrogels in Section 2. We then obtain homogeneous solutions and the onset conditions of phase separation of hydrogels under free swelling, hydrostatic loading, constrained uniaxial deformation and constrained biaxial deformation in Section 3. Using the phase-field model, we simulate the phase separation and pattern evolution of hydrogels under one-dimensional and two-dimensional settings with finite system sizes in Section 4. We further investigate the effect of quenching and stretching rates in Section 5. Section 6 concludes the chapter.

3.2 Constitutive Models of Hydrogels

Here we consider the deformation of a hydrogel subjected to applied mechanical loadings and solvent exchanges with an external solvent. The dry polymer is taken as the reference state, where the material point of the hydrogel labeled with a coordinate $\boldsymbol{X}$ is displaced to a coordinate $\boldsymbol{x}$ in the current state at time t (Figure 3.1). The deformation gradient tensor of the hydrogel is defined as $\mathbf{F} = \partial \boldsymbol{x}/\partial \boldsymbol{X}$ or $F_{iK} = \partial x_i/\partial X_K$, whose determinant $J = \det \mathbf{F}$ represents the volume

change of the material point. The number of solvent molecules per unit reference volume is denoted as C. The polymer network and solvent are assumed to be incompressible, which gives

$$vC+1=J, \tag{3.1}$$

where v is the volume of a solvent molecule. The inverse of the swelling ratio is related to the polymer concentration ϕ via $1/J=\phi$.

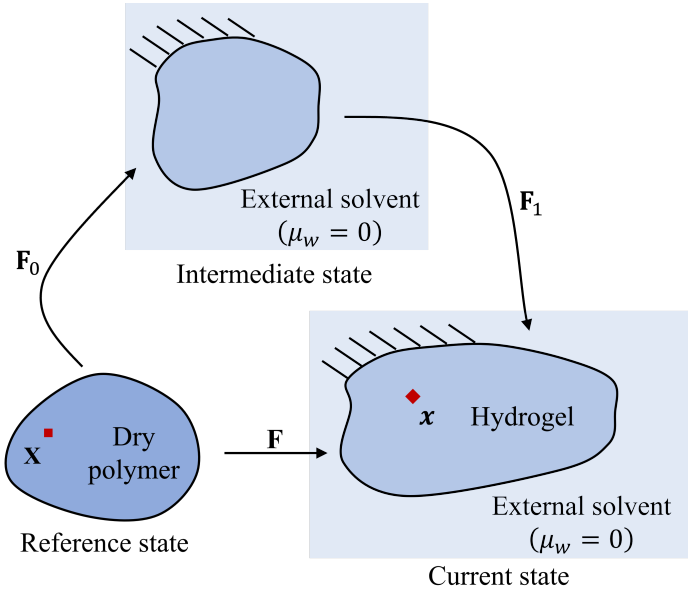

Figure 3.1 Schematic of the reference, intermediate and current states. The intermediate state is chosen as the initial state in numerical simulations.

The free energy of the hydrogel per unit reference volume is contributed by the stretching of the network and the mixing of the polymer and solvent [12, 128, 129],

$$W=\frac{1}{2}NkT\left(F_{iK}F_{iK}-3-2\ln J\right)+\frac{kT}{v}\left(vC\ln\frac{vC}{vC+1}+\chi\frac{vC}{vC+1}\right), \tag{3.2}$$

where N is the crosslink density of the hydrogel in the dry state, k is the Boltzmann constant, T is the temperature, and χ is the interaction constant measuring the enthalpy of mixing between the polymer and solvent. The parameter χ is often a function of polymer concentration $\chi = \chi(\phi)$, empirically fitted from experimental results [125, 130]. Specifically, χ often increases with ϕ for poor solvents, while is nearly independent of ϕ for good solvents [131]. There is not a universal $\chi(\phi)$ function. Although a frequently used form is a polynomial relation, the fitted parameters can vary widely. Here our goal is to demonstrate that mechanical constraints can lead to coexistence of multiple phases in hydrogels where coexistence does not occur without constraints. The Flory-Rehner free energy with the parameter χ independent of ϕ describs such hydrogels, and it does not predict volume phase transitions of these hydrogels under equilibrium free swelling. Therefore, instead of choosing a specific $\chi(\phi)$ function with a specific set of parameters, here we simply assume χ is independent of ϕ for the majority of the demonstration in this chapter. The dependence of χ on other external fields, such as temperature $\chi = \chi(\phi)$, is directly prescribed as variations of χ within a reasonable range from 0 to 2, comparable to that in the literature [122, 125]. To further show that our method can be easily extended to different $\chi(\phi)$ functions, in Appendix A2, we demonstrate the phase behavior of a hydrogel with $\chi = \chi_1 + \chi_2\phi$ as an example. It is worth mentioning that there are many other forms of stretching energy considered in the literature, and the stretching energy can also be formulated by choosing the initial fabrication state as the relaxation state of the polymer network [57, 132-134], the energy which tends to become double-welled more easily under mechanical constraints. Therefore, here we show that even with the current stretching energy in (3.2), a hydrogel with a single phase under equilibrium

swelling can undergo complex phase behaviors under mechanical constraints. Our method and results can be easily extended to hydrogels with other forms of free energy.

Given the free energy, the nominal stress can be obtained as [135]

$$s_{iK} = \frac{\partial W}{\partial F_{iK}} - \Pi J H_{iK} = NkT\left(F_{iK} - H_{iK}\right) - \Pi J H_{iK}, \tag{3.3}$$

where Π is a Lagrange multiplier to enforce the incompressibility condition (3.1), and H_{iK} defined by $H_{iK} = (1/J)\,\partial J/\partial F_{iK}$ leads to $\mathbf{H} = \mathbf{F}^{-T}$. The chemical potential of the solvent molecules in the hydrogel can be calculated as [135]

$$\mu = \frac{\partial W}{\partial C} + \Pi v = kT\left[\ln\frac{vC}{vC+1} + \frac{1}{vC+1} + \chi\frac{1}{(vC+1)^2}\right] + \Pi v. \tag{3.4}$$

When the hydrogel reaches chemical equilibrium, the chemical potential μ equals the chemical potential of the solvent in the environment, μ_w. We assume $\mu_w = 0$, unless otherwise mentioned. Several cases of homogeneous deformation are studied in the next section.

3.3 Homogeneous State of Equilibrium

In this section, we study homogeneous deformation of a hydrogel, its energy landscape and stability under various mechanical constraints. A local minimum of free energy corresponds to an equilibrium state of the hydrogel. Therefore, the coexistence of multiple phases is identified by the existence of multiple local minima and via analyzing the non-convexity of the free energy.

We consider a hydrogel immersed in a solvent subjected to a certain mechanical constraint. Four cases are studied here: (1) free swelling, (2) swelling under hydrostatic loading, (3) swelling

with constrained uniaxial deformation, and (4) swelling with constrained biaxial deformation. For case (1), no mechanical constraint is applied on the hydrogel, and the swelling is assumed to be isotropic so that $F_{iK} = \lambda\delta_{iK} = J^{1/3}\delta_{iK}$, where λ is the stretch in all directions. For case (2), the hydrogel is subjected to a hydrostatic loading with a fixed nominal stress s. The swelling is assumed to be isotropic, $F_{iK} = \lambda\delta_{iK}$. It is noted that this hydrostatic loading defined by fixed nominal stress is different from the usual hydrostatic stress defined by fixed true stress. For case (3), two principal stretches of the hydrogel are assumed to be one, and in the other principal direction the hydrogel exerts a nominal stress s. The deformation gradient can be written as $\mathbf{F} = diag(\lambda, 1, 1)$. For case (4), the hydrogel is assumed to undergo isotropic in-plane deformation with fixed equi-biaxial nominal stress s. The other principal stretch is assumed to be one. The deformation gradient can be written as $\mathbf{F} = diag(\lambda, \lambda, 1)$.

Combining with the incompressibility constraint (3.1), the free energy (3.2) becomes

$$W = \frac{d}{2}NkT\left(\lambda^2 - 1 - 2\ln\lambda\right) + \frac{kT}{v}\left[\left(\lambda^d - 1\right)\ln\frac{\lambda^d - 1}{\lambda^d} + \chi\frac{\lambda^d - 1}{\lambda^d}\right], \tag{3.5}$$

where $d\ (= 1,2,3)$ represents the dimension of deformation. $d = 1$ corresponds to case (3), $d = 2$ corresponds to case (4), and $d = 3$ corresponds to cases (1) and (2). Selecting the system to be the hydrogel, the environment and the load, we obtain the total free energy of the system to be the sum of that of all the components

$$G = \frac{d}{2}NkT\left(\lambda^2 - 1 - 2\ln\lambda\right) + \frac{kT}{v}\left[\left(\lambda^d - 1\right)\ln\frac{\lambda^d - 1}{\lambda^d} + \chi\frac{\lambda^d - 1}{\lambda^d}\right] - \frac{\mu_w}{v}\left(\lambda^d - 1\right) - ds\lambda. \tag{3.6}$$

When the system is in equilibrium, the first derivative of the free energy G with respect to λ vanishes,

$$\frac{\partial G}{\partial \lambda} = dNkT\left(\lambda - \frac{1}{\lambda}\right) + d\frac{kT}{v}\left(\lambda^{d-1}\ln\frac{\lambda^d - 1}{\lambda^d} + \frac{1}{\lambda} + \frac{\chi}{\lambda^{d+1}}\right) - d\frac{\mu_w}{v}\lambda^{d-1} - ds = 0. \tag{3.7}$$

The stability criterion for the system is determined by the second derivative of G with respect to λ,

$$\begin{aligned}\frac{\partial^2 G}{\partial \lambda^2} = {} & dNkT\left(1 + \frac{1}{\lambda^2}\right) + d\frac{kT}{v}\left[(d-1)\lambda^{d-2}\ln\frac{\lambda^d - 1}{\lambda^d} + \frac{d\lambda^{d-2}}{\lambda^d - 1} - \frac{1}{\lambda^2} - (d+1)\frac{\chi}{\lambda^{d+2}}\right] \\ & - d(d-1)\frac{\mu_w}{v}\lambda^{d-2} = 0.\end{aligned} \tag{3.8}$$

When $\partial^2 G/\partial\lambda^2 > 0$, the system is stable.

3.3.1 Free swelling

When the hydrogel is under free swelling, we have $s = 0$. Eqs. (3.7) and (3.8) determine the condition of equilibrium and the stability of the system. For the free swelling case, we use the swelling ratio J as a variable and obtain the equivalent forms to Eqs. (3.7) and (3.8). The free energy (3.2) expressed as a function of J is

$$W = \frac{1}{2}NkT\left(3J^{\frac{2}{3}} - 3 - 2\ln J\right) + \frac{kT}{v}\left[(J-1)\ln\frac{J-1}{J} + \chi\frac{J-1}{J}\right]. \tag{3.9}$$

When the hydrogel is in equilibrium, Eq. (3.7) is equivalent to the following equation,

$$\frac{\partial W}{\partial J} = NkT\left(J^{-\frac{1}{3}} - \frac{1}{J}\right) + \frac{kT}{v}\left(\ln\frac{J-1}{J} + \frac{1}{J} + \frac{\chi}{J^2}\right) = \frac{\mu_w}{v}. \tag{3.10}$$

The free energy W is plotted as a function of J at different values of χ, and points a, b and c correspond to the equilibrium solutions when $\mu_w = 0$ (Figure 3.2a).

Whether the system is stable or not can also be determined by the second derivative of W with respect to J,

$$\frac{\partial^2 W}{\partial J^2} = NkT\left(-\frac{1}{3}J^{-\frac{4}{3}} + J^{-2}\right) + \frac{kT}{v}\left[\frac{1}{(J-1)J^2} - \frac{2\chi}{J^3}\right] = 0. \tag{3.11}$$

Eq. (3.11) is equivalent to Eq. (3.8), if μ_w is eliminated by substituting Eq. (3.7) into Eq. (3.8). Eq. (3.11) determines the stability of the system regardless of the value of μ_w. When $\partial^2 W/\partial J^2$ is positive, the hydrogel prefers to stay homogeneous, while when $\partial^2 W/\partial J^2$ is negative, phase separation occurs. The solutions to Eq. (3.11) are shown as points d and e in Figure 3.2a, where we have $\partial^2 W/\partial J^2 > 0$ when the swelling ratio is smaller than that of point d or e. When $\chi = 0.2$, the solution to Eq. (3.11) is $J = 29.3$, which is not shown in Figure 3.2a. Clearly, when $\mu_w = 0$, all three equilibrium solutions a, b and c are stable.

Solutions to Eq. (3.10) under $\mu_w = 0$ (the black curve) and $\mu_w = 0.015kT$ (the blue curve) and to Eq. (3.11) (the red curve) are plotted as functions of χ (Figure 3.2b). The red curve, corresponding to the solution to Eq. (3.11), is called the spinodal curve. Above the curve, we have $\partial^2 W/\partial J^2 < 0$ and the system is unstable. The black curve of the equilibrium solutions when $\mu_w = 0$ is always below the spinodal curve, indicating the equilibrium states are stable. The blue curve of the equilibrium solutions when $\mu_w = 0.015kT$ intersects with the red curve at point f corresponding to $J = 3.02$ and $\chi = 0.75$. Under a given χ larger than 0.75, there are two solutions of J to Eq. (3.10). The solution corresponding to J smaller than 3.02 is stable, since it is below the

red curve, while the other solution is unstable. In general, for $\mu_w > 0$, there are either zero, one or two solutions to Eq. (3.10) for a given χ, where the one solution corresponds to the intersection of solutions to Eq. (3.10) and Eq (3.11), for example, point f for $\mu_w = 0.015kT$. When there are two solutions, one solution is stable and the other one is unstable. Since there is at most one stable solution, there is no phase coexistence when the hydrogel is under equilibrium. According to the literature and the discussion of Figure A2 in Appendix A2, when the parameter χ depends on the swelling ratio J, there might exist two stable equilibrium solutions.[111] As a conclusion, although phase coexistence can be predicted when the parameter χ depends on the swelling ratio J, for the case of free swelling, the free energy (3.9) with constant χ cannot predict equilibrium phase coexistence.

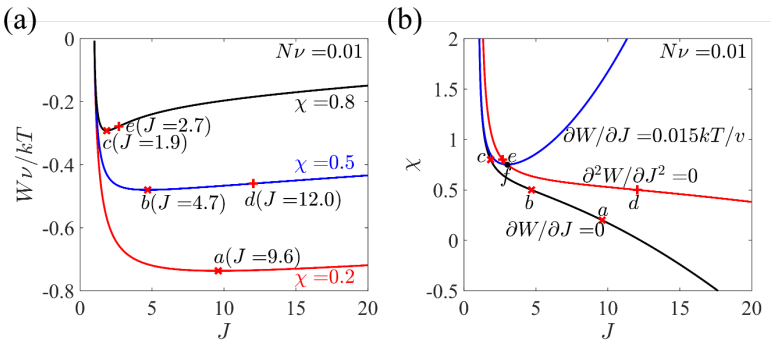

Figure 3.2 A hydrogel is in equilibrium with an external solvent without mechanical constraints. (a) The free energy as a function of the swelling ratio J at various χ. Points a, b, and c correspond to the equilibrium solutions when $\mu_w = 0$, and points d and e are the solutions to Eq. (3.11). (b) The equilibrium solutions under $\mu_w = 0$ (the black curve) and $\mu_w = 0.15kT$ (the blue curve) and the spinodal curve (the red curve). Points *a*-*e* correspond to the same conditions as in (a), while

point f is the intersection of solutions to Eq. (3.10) (i.e. the equilibrium solutions) and to Eq (3.11) when $\mu_w = 0.015kT$.

3.3.2 Swelling under hydrostatic loading

We next consider a hydrogel under a hydrostatic loading immersed in a solvent with $\mu_w = 0$. The free energy W is plotted as a function of λ at different values of χ (Figure 3.3a). The convexity of the curve changes when χ increases. When χ is small, the free energy is convex for the entire range of stretch λ; the corresponding examples of $\chi = 0.2$ and 0.5 are shown in Figure 3.3a. As Eq. (3.7) shows, the system reaches equilibrium when $\partial G/\partial\lambda = \partial W/\partial\lambda - 3s = 0$, where the slope of the free energy W equals to $3s$. Since $\partial^2 G/\partial\lambda^2 = \partial^2 W/\partial\lambda^2 > 0$ when χ is small, there is only one solution of stretch for a given external stress. On the other hand, when χ is large, the free energy becomes concave for an intermediate range of stretch λ. For example for $\chi = 0.8$ there is a common tangent line (the red dashed line in Figure 3.3a) intersecting the $W - \lambda$ curve at points a and b. The slope of the common tangent $3s^*$ corresponds to the critical stress s^* for coexistence, when the free energy G for the coexisting phases are equal. We further plot the free energy of the system $G = W - 3s\lambda$ defined in Eq. (3.6) as a function of λ in Figure 3.3b. When $s = s^*$, the free energy G indeed has two local minima with equal values, indicating that the two phases can coexist when stress s^* is applied. When s is slightly smaller ($s = 0.9s^*$) or larger ($s = 1.2s^*$) than s^*, the free energy G is still double-well, but the shrunk phase has lower or higher free energy than the swollen phase, respectively. As s further decreases ($s = 0.75s^*$) or increases ($s = 1.35s^*$), the free energy G becomes single-well, with the single minimum corresponding to one stable equilibrium shrunk or swollen phase, respectively. The two local minima in Figure 3.3b

correspond to the two tangent points in Figure 3.3a. Using the condition $\partial^2 G/\partial\lambda^2 = 0$, we identify points c and d. When a stretch is between points c and d, we have $\partial^2 G/\partial\lambda^2 < 0$, which indicates that the system is unstable and phase separation might occur. Connecting all the tangent points for various χ, we obtain the binodal curve (the red curve in Figure 3.3c). The spinodal curve and the binodal curve merge at the critical point e, corresponding to a critical interaction parameter χ_c and a critical stretch λ_c, where χ_c is the smallest value of χ that can induce phase separation. Solving Eq. (3.7), we plot the nominal stress s as a function of λ at different values of χ (Figure 3.3d). When χ is smaller than χ_c, the nominal stress increases monotonically as λ increases, and the corresponding free energy is convex (Figure 3.3a). When χ is larger than χ_c, the stress-stretch curve becomes non-monotonic, and there might exist three stretch solutions under a fixed stress value. The non-monotonic stress-stretch curves are also plotted with $\chi = \chi_1 + \chi_2\phi$ (Figure 3.S1e). The volume phase transition might occur with two phases coexisting when the hydrogel is gradually stretched to a certain range. It is worth mentioning that the stretch for coexisting phases may not be predicted accurately. Taking $\chi = 0.8$ as an example, if both two coexisting phases follow the assumed deformation $F_{iK} = \lambda\delta_{iK}$, the stretch values of the two phases correspond to those of points a and b in Figure 3.3, which minimizes the free energy of the system consists of the hydrogel and the load. However, the two separated phases may not follow the assumed homogeneous deformation due to the stretch mismatch between the two phases. Therefore, the free energy W of the hydrogel may not be simply written as Eq, (3.5). The solution to this issue will be discussed in Sec. 4.

Figure 3.3e shows the equilibrium solutions under free swelling (the red curve) and hydrostatic loading (the blue curve). It is noted that the free swelling case ($\mu_w = 0$ and $s = 0$) is

a special case of swelling under hydrostatic loading when the applied stress equals zero. From Figure 3.3e, it is shown that when the stress equals zero there exists only one solution of stretch for a given parameter χ, and the stretch decreases monotonically with the increase of χ. In contrast, when $s = 0.032kT/v$, the stretch changes non-monotonically with the increase of χ, and there might exist three solutions of stretch for a given χ in certain range of value, verifying the predictions of Duda et al [121]. Meanwhile, Cirillo et al. predicted that when a hydrogel is subjected to a hydrostatic true stress, no phases coexist under three-dimensional volumetric deformation [120]; in their study, the defined pressure load is equivalent to μ_w in our manuscript. According to our studies of hydrogels under free swelling, there is at most one stable solution for given μ_w, which also validates the results of Cirillo et al. The seemingly contradictory results come from different mechanical loadings.

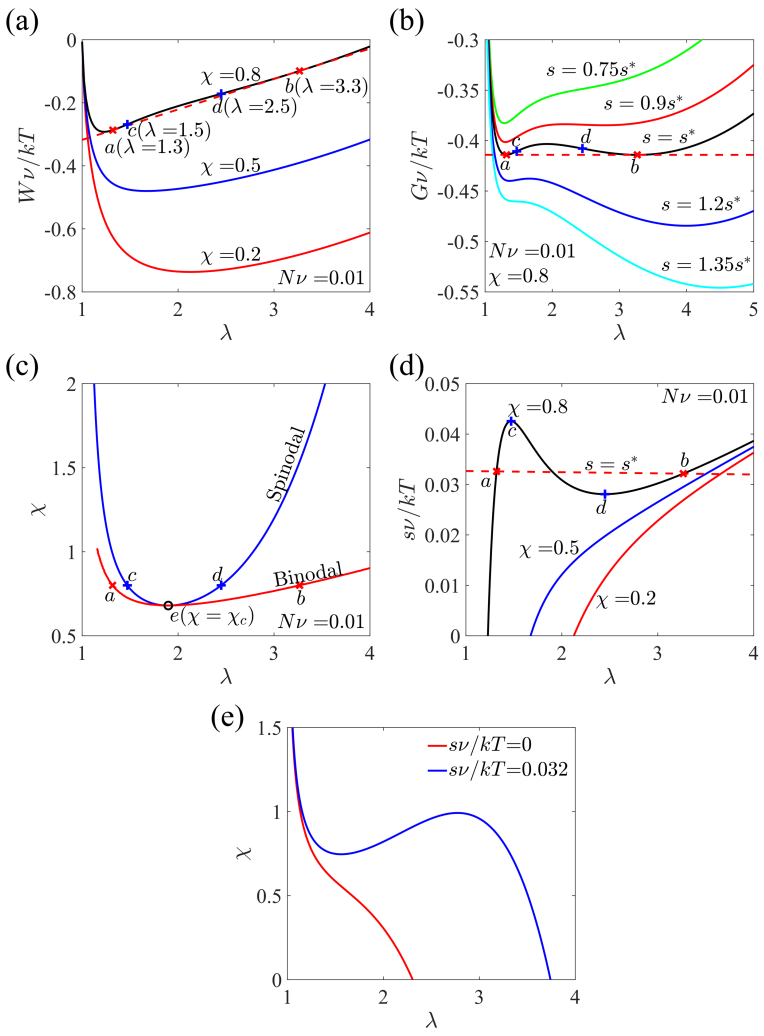

Figure 3.3 A hydrogel subjected to hydrostatic loading is in equilibrium with an external solvent. (a) The free energy W as a function of stretch at various χ. Points a and b are the two intersection points of the $W - \lambda$ curve and the common tangent line (the red dashed line), and points c and d are solutions to Eq. (3.8). (b) The free energy $G = W - 3s\lambda$ as a function of stretch for $\chi = 0.8$ under different values of s. (c) Spinodal and binodal curves with their intersection point e. (d) Nominal stress as a function of stretch at various χ. Points a-d correspond to the same conditions

in (a), (b), (c) and (d). (e) The equilibrium solutions under $s = 0$ (the red curve) and $s = 0.032kT/v$ (the blue curve).

3.3.3 Swelling with constrained uniaxial and biaxial deformation

For a hydrogel with constrained uniaxial deformation, the free energy of the total system is

$$G = \frac{1}{2}NkT\left(\lambda^2 - 1 - 2\ln\lambda\right) + \frac{kT}{v}\left[(\lambda - 1)\ln\frac{\lambda - 1}{\lambda} + \chi\frac{\lambda - 1}{\lambda}\right] - s\lambda - \frac{\mu_w}{v}\lambda. \tag{3.12}$$

The equilibrium condition (3.7) can be rewritten as

$$s + \frac{\mu_w}{v} = NkT\left(\lambda - \frac{1}{\lambda}\right) + \frac{kT}{v}\left(\ln\frac{\lambda - 1}{\lambda} + \frac{1}{\lambda} + \frac{\chi}{\lambda^2}\right). \tag{3.13}$$

Clearly from Eqs. (3.12) and (3.13), the applied stress plays the same role as the chemical potential of the solvent in the equilibrium state for the constrained uniaxial case, which is not true for the constrained biaxial case.

For both the constrained uniaxial and biaxial cases, the phase diagram under $\mu_w = 0$ is shown in Figure 3.4a, where the solid curves correspond to the constrained uniaxial swelling, while the dashed curves correspond to the constrained biaxial case. Under a fixed value of χ, there could exist multiple solutions of stretch λ. The critical interaction parameter χ_c of the biaxial case is lower than that for the uniaxial case, both of which are higher than that of the hydrostatic case (Figure 3.4a & b). This could be understood by the fact that lower-dimensional deformation means a higher degree of anisotropy of the deformation, which leads to higher elastic energy and requires higher χ_c. χ_c increases with the increase of the normalized modulus Nv, which means poorer

solvent is required to achieve phase separation when the network is more densely crosslinked (Figure 3.4b). Figure 3.4c shows the critical stretch λ_c and the corresponding critical volume J_c decrease as Nv increases, while J_c increases but λ_c decreases as the dimension of deformation increases (Figure 3.4c). When χ is beyond χ_c, the stress-stretch curves are non-monotonic for both constrained uniaxial and biaxial cases (Figure 3.4d). Therefore, two phases might coexist for both cases.

It's worth mentioning that Cirillo et al. theoretically showed that two phases could coexist when a hydrogel is under constrained uniaxial deformation subjected to a fixed stress while the chemical potential is zero [120]. Under similar constrained uniaxial deformation, Hennessy et al. also demonstrated that two phases could coexist when a hydrogel is prescribed with a fixed chemical potential while the stress is zero [118]. Our equilibrium equation (3.13) shows the equivalent roles of applying a chemical potential and stress in phase separation of hydrogels with constrained uniaxial swelling. Kim et al. demonstrated composite PNIPAM hydrogels with cofacially aligned nanosheets could rapidly respond to temperature changes [124]. In their experiments, two neighboring paralleled nanosheets confine the deformation of the hydrogel in-between to be constrained uniaxial deformation. Parameter χ increases as temperature increases, leading to an increase of the chemical potential inside the hydrogel. According to our predictions, multiple equilibrium states could exist when a hydrogel with constrained uniaxial deformation is prescribed with a fixed chemical potential. Therefore, the hydrogel may transit from one state to another state, whose deformation is discontinuous and can occur rapidly. Our results could further justify the explanations of Yamamoto et al. on the experiments, which predicted that such constrained hydrogels can undergo discontinous deformation with a constant volume [122].

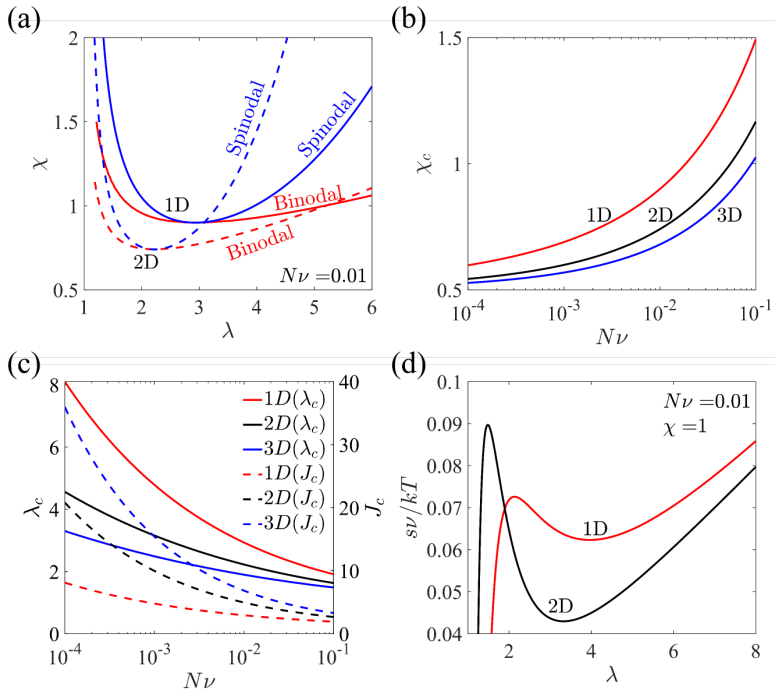

Figure 3.4 A hydrogel is in equilibrium with an external solvent under constrained uniaxial (1D) and biaxial (2D) deformation. (a) Spinodal and binodal curves. (b) Critical interaction parameter χ_c as a function of crosslink density Nv for constrained uniaxial, biaxial, and hydrostatic (3D) deformation. (c) Critical stretch λ_c and the corresponding critical volume J_c as functions of crosslink density Nv. (d) Non-monotonic nominal stress-stretch relations at high χ.

3.4 Numerical Simulations of Phase Separation

Our previous analysis is based on an assumption of homogeneous deformation. However, when a hydrogel is unstable, and separates into two phases, it does not follow homogeneous deformation, but highly inhomogeneous deformation with a large misfit between the two separated phases. In addition, the previous analysis is also not able to predict what the morphology of the

separated phases is and how the phases evolve. To address these problems, the phase-field method is used to simulate the phase behaviors of hydrogels in this section.

3.4.1 Phase-field model

Selecting the concentration of solvent molecules C as the conservative phase-field variable, we introduce the gradient of the concentration to describe a diffuse interface between different phases. Following Hong and Wang, the free energy is assumed to be [116]

$$W = \frac{1}{2}NkT\left(I_1 - 3 - 2\ln J\right) + \frac{\kappa}{2}\left(J - vC - 1\right)^2 + \frac{kT}{v}\left(vC\ln\frac{vC}{vC+1} + \chi\frac{vC}{vC+1}\right) + \frac{\eta}{2}JH_{iK}\frac{\partial C}{\partial X_K}\frac{\partial C}{\partial X_L}H_{iL}, \tag{3.14}$$

where the second term is an energy penalty to enforce the incompressibility (3.1) with κ the bulk modulus, and the last term is an ideal interface energy. The interfacial parameter η in Eq. (3.14) penalizes the formation of sharp interfaces, and plays a role of surface tension. The mixing and interfacial energy defines a characteristic length $l = \sqrt{\eta/vkT}$. The mixing energy in Eq. (3.14) is different from the one used by Hong and Wang, where their mixing energy has double wells under free swelling when χ is large.[116]

By minimizing the total free energy of the system and combining the conservation of the solvent molecules, the stress equilibrium and the evolution equation of the phase field are obtained as[116]

$$\frac{\partial s_{iK}}{\partial X_K} = 0, \tag{3.15}$$

$$\frac{\partial C}{\partial t}+\frac{\partial\left(-\frac{DC}{kT}H_{iK}H_{iL}\frac{\partial\mu}{\partial X_L}\right)}{\partial X_K}=0, \tag{3.16}$$

where

$$\begin{aligned} s_{iK} &= NkT\left(F_{iK}-H_{iK}\right)+\kappa\left(J-vC-1\right)JH_{iK} \\ &\quad +\frac{\eta}{2}JH_{jM}\frac{\partial C}{\partial X_M}\frac{\partial C}{\partial X_L}H_{jL}H_{iK}-\eta JH_{jM}\frac{\partial C}{\partial X_M}\frac{\partial C}{\partial X_L}H_{iL}H_{jK}, \end{aligned} \tag{3.17}$$

$$\mu=kT\left[\ln\frac{vC}{vC+1}+\frac{1}{vC+1}+\chi\frac{1}{(vC+1)^2}\right]-\kappa v\left(J-vC-1\right)-\eta\frac{\partial}{\partial X_L}\left(JH_{iL}H_{iK}\frac{\partial C}{\partial X_K}\right). \tag{3.18}$$

The Cauchy stress is related to the nominal stress by $\sigma_{ij}=s_{iK}F_{jK}/J$. The characteristic length l and the diffusivity D lead to a characteristic time $t_0=l^2/D$. To solve the above equations, chemical and mechanical boundary conditions are further needed. Assuming the hydrogel is always immersed in a pure solvent, then we have

$$\mu=0, \tag{3.19}$$

at the interface between the hydrogel and the environmental solvent. Since the expression of chemical potential μ includes a second derivative of the concentration C, another boundary condition is needed. For all the boundaries, we require

$$\frac{\partial C}{\partial x_i}n_i=0, \tag{3.20}$$

where n_i is the unit outer normal of the boundaries in the current state. For the mechanical boundary conditions, either displacement or traction can be prescribed, which will be given in the following examples.

The weak form of Eqs. (3.15)- (3.18) is implemented into the commercial software COMSOL to determine the temporal evolution of the fields of displacement, concentration and chemical potential. The cubic Lagrange element is used for the discretization of the displacement field, while the linear Lagrange element is used for the discretization of the concentration and chemical potential. The MUMPS solver and an implicit time discretization has been used for computation. Unless otherwise stated, a mesh size equal to the characteristic length has been used, achieving a good convergence of results. To enforce the incompressibility, $\kappa = 1000NkT$ is chosen. Due to the singularity of the chemical potential in the dry state, an intermediate state with zero chemical potential is introduced as the initial state in numerical simulations (Figure 3.1). The total deformation gradient is decomposed as $\mathbf{F} = \mathbf{F}_1\mathbf{F}_0$, where $\mathbf{F}_0$ maps the reference state to the intermediate state, and $\mathbf{F}_1$ maps the intermediate state to the current state. The intermediate state chosen to be homogeneous, and the initial stress obtained from Eq. (3.7) is applied to the hydrogel. In the section 3.4.2 and 3.4.3, we start the simulations with a constant χ of a high value, and the hydrogels in the intermediate state are unstable. As a result, phase separation occurs, and swollen and shrunk phases evolve with time. To trigger the onset of the phase separation, a random small perturbation ranging from $-5 \times 10^{-4}C_0$ to $5 \times 10^{-4}C_0$ is imposed on the initial concentration C_0 for all simulations. The amplitude of the perturbation only influences the speed of the coarsening process in the early stage ($t \sim l^2/D$), and a slightly larger perturbation leads to faster initial coarsening. The initial small perturbation has little influence on the phase evolving process in the

later stage, i.e., statistically equivalent patterns are obtained under different initial perturbations after $t \sim l^2/D$, and identical patterns are obtained after $t \sim L^2/D$ with L the size of the hydrogel.

3.4.2 Phase separation of hydrogels under constrained uniaxial deformation

We start from a hydrogel with two fixed ends and initial stretch $\lambda_0 = 3$, where the length of the hydrogel in the initial state is denoted as L (Figure 3.5). At the two ends of the hydrogel, we impose

$$u = 0, \tag{3.21}$$

where u is the displacement of the hydrogel in the current state with respect to the hydrogel in the initial state. As shown in Figure 3.4a, the hydrogel is unstable when the parameter χ is high, where phase separation is expected to occur. The total deformation gradient of the hydrogel with respect to the reference state is denoted as $\mathbf{F} = diag(\lambda, 1, 1)$.

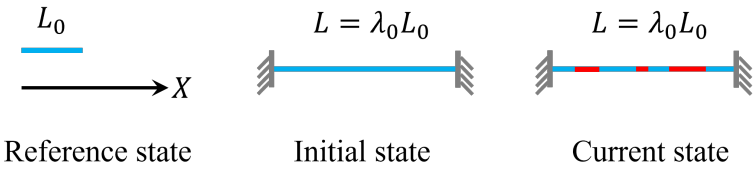

Figure 3.5 Schematic of a hydrogel under constrained uniaxial deformation in the reference, initial and current states. In the current state, the hydrogel undergoes phase separation with different colors representing different stretch values of the swollen and shrunk phases.

The evolution of stretch as a function of the Lagrangian coordinate X associated with the reference state is shown in Figure 3.6a & b for different values of χ. The initial fluctuation grows and coarsens as a function of time. The domains near the boundary grow faster than those in the

bulk, because the gradient of the chemical potential is higher near the boundary than that in the bulk. The hydrogel finally reaches equilibrium after a long time, e.g., $t_1/t_0 = 2 \times 10^7$ in Figure 3.6a. When χ is higher, phase separation occurs easier and faster in the hydrogel. Moreover, more domains are observed during the phase separation process, and the stretch ratio between the swollen and shrunk domains is higher when the hydrogel reaches equilibrium. Figure 3.6c shows the influence of the system size on the distribution of stretch when the hydrogel reaches equilibrium. The red dashed line is the theoretical prediction of the common tangent construction, while the solid lines are the simulation results, which approach the theoretical prediction when the ratio of the sample length to the characteristic length, L/l, is large. On the other hand, when L/l is small, we cannot obtain two phases corresponding to the homogenous solutions, and the stretch distribution cannot be predicted by the common tangent construction. When L/l is small enough, the system is stabilized by the interfacial energy, and phase separation can be suppressed. Figure 3.6d shows the L/l-λ_0 diagram of phase separation at different χ. For a given χ, phase separation occurs above the curve, while phase separation does not occur below the curve. A higher χ is required for the occurrence of phase separation of a smaller system.

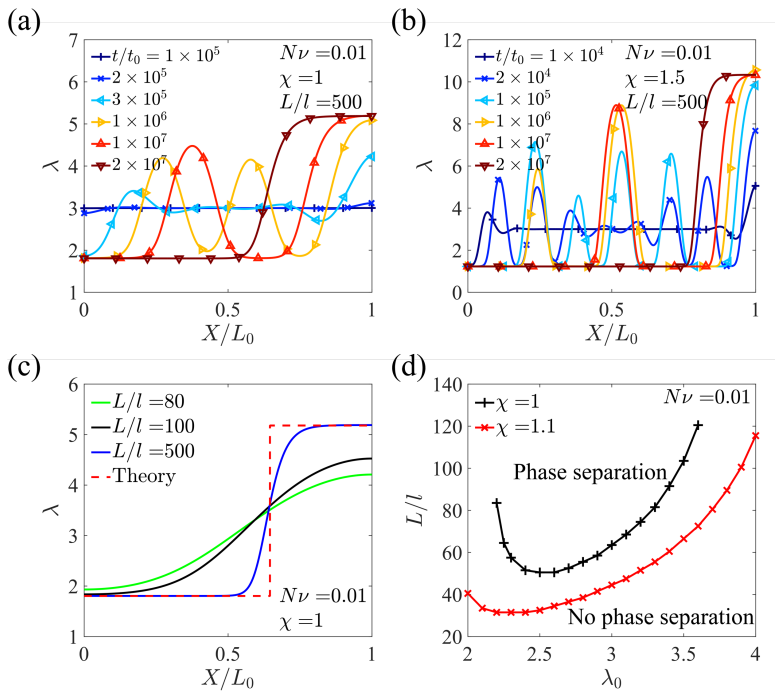

Figure 3.6 The temporal evolution of stretch as a function of the Lagrangian coordinate X associated with the reference state at (a) $\chi = 1$ and (b) $\chi = 1.5$. (c) The equilibrium distribution of stretch for hydrogels with different ratios of the sample length to the characteristic length, L/l. (d) L/l-λ_0 diagram of phase separation at different χ.

3.4.3 Phase separation of hydrogels under constrained biaxial deformation

We next consider that a hydrogel under constrained biaxial deformation with initial stretch λ_0 undergoes phase separation (Figure 3.7). On the boundaries, the hydrogel is assumed to be able to move freely in the parallel direction but have no displacement in the perpendicular direction, i.e. we impose the boundary conditions

$$\begin{cases} u = 0, \sigma_{xy} = 0, & \text{on } X = 0, L_0 \\ v = 0, \sigma_{xy} = 0, & \text{on } Y = 0, L_0 \end{cases}, \tag{3.22}$$

where u and v are the displacements of the hydrogel in the X and Y directions in the current state with respect to the initial state. It's worth mentioning that large mesh size ($\approx 5l$) is used for the simulation of the large sample, where the coarse meshes still give a good convergence of results.

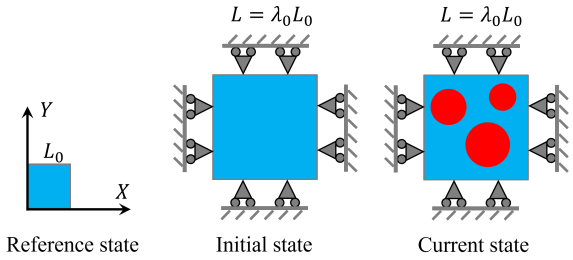

Figure 3.7 Schematic of a hydrogel under constrained biaxial deformation in the reference, initial and current states. In the current state, the hydrogel undergoes phase separation with different colors representing the distribution of the concentration of different phases.

Figure 3.8a is the L/l-λ_0 diagram of phase separation for $\chi = 0.8$, with the different regions in the phase plane showing no phase separation, and phase separation with different morphologies. The three simulation contour plots demonstrate the distribution of the normalized concentration vC for the hydrogel under equilibrium, where the black solid curves correspond to the initial concentrations of the hydrogel, and the mesh grids, which are uniform in the initial state, show the deformation of the hydrogel. Three patterns, solvent rich island, strip, and solvent poor island, are observed. Since the interfacial energy is proportional to the length of the interface between the swollen and shrunk phases, the length of the interface needs to be minimized to reduce the total energy of the system. Therefore, the solvent-rich-island pattern is expected to occur when the solvent concentration of the hydrogel is relatively low, and the solvent-poor-island pattern

occurs when the solvent concentration is relatively high. It is also noted that the deformation of the swollen and shrunk phases in the strip pattern is highly anisotropic. When χ is increased to 2, the boundary between phase separation and no phase separation is significantly lower, indicating phase separation can occur in much smaller hydrogels (Figure 3.8b). Moreover, the solvent-poor-island pattern can occur in a much broader region in the phase plane.

We next plot the concentration distribution along the diagonal A_1A_3 to characterize the solvent-rich-island pattern for different sample sizes L/l (Figure 3.8c). Due to the strain mismatch between the two phases, we see an inhomogeneous distribution of concentration. When the sample size is large, the concentration distribution along the diagonal A_1A_3 is non-monotonic. In the shrunk region, the concentration reaches the minimum close to the interface, and slightly increases when the position is away from the interface until reaching a plateau, indicating a homogeneous shrunk phase. It is noted that the portion of the inhomogeneous region is finite in the shrunk phase (Figure 3.8c). When the sample size becomes smaller, the concentration distribution is smoothened due to the influence of the interfacial energy. The two phases at corners A_1 and A_3 are almost homogeneous and isotropic when the sample size is large enough, while the deformation at corners A_2 and A_4 is anisotropic (Figure 3.8a), which violates the assumption of the constrained biaxial deformation for the homogeneous solutions. The stretch values in *X* direction differ a lot from that in *Y* direction at corner A_2 for hydrogels with different sample sizes (Figure 3.8d). The concentrations of the swollen and shrunk phases at corners A_1 and A_3 are plotted as functions of the sample size (Figure 3.8e), where the concentration of the swollen phase shows particularly strong size-dependent. The dashed lines are obtained by the common tangent construction for the homogeneous solutions, which agrees well with the simulation results when the sample size is

large. The similar size effect on the concentrations of the swollen and shrunk phases is also observed in the solvent-poor-island pattern. Different from the solvent-rich-island and solvent-poor-island patterns, the strip pattern shows a concentration distribution similar to the homogeneous solution of the constrained uniaxial deformation, instead of the constrained biaxial deformation (Figure 3.8f), and the deformation gradient can be assumed to be $\mathbf{F} = diag(\lambda, \lambda_0, 1)$.

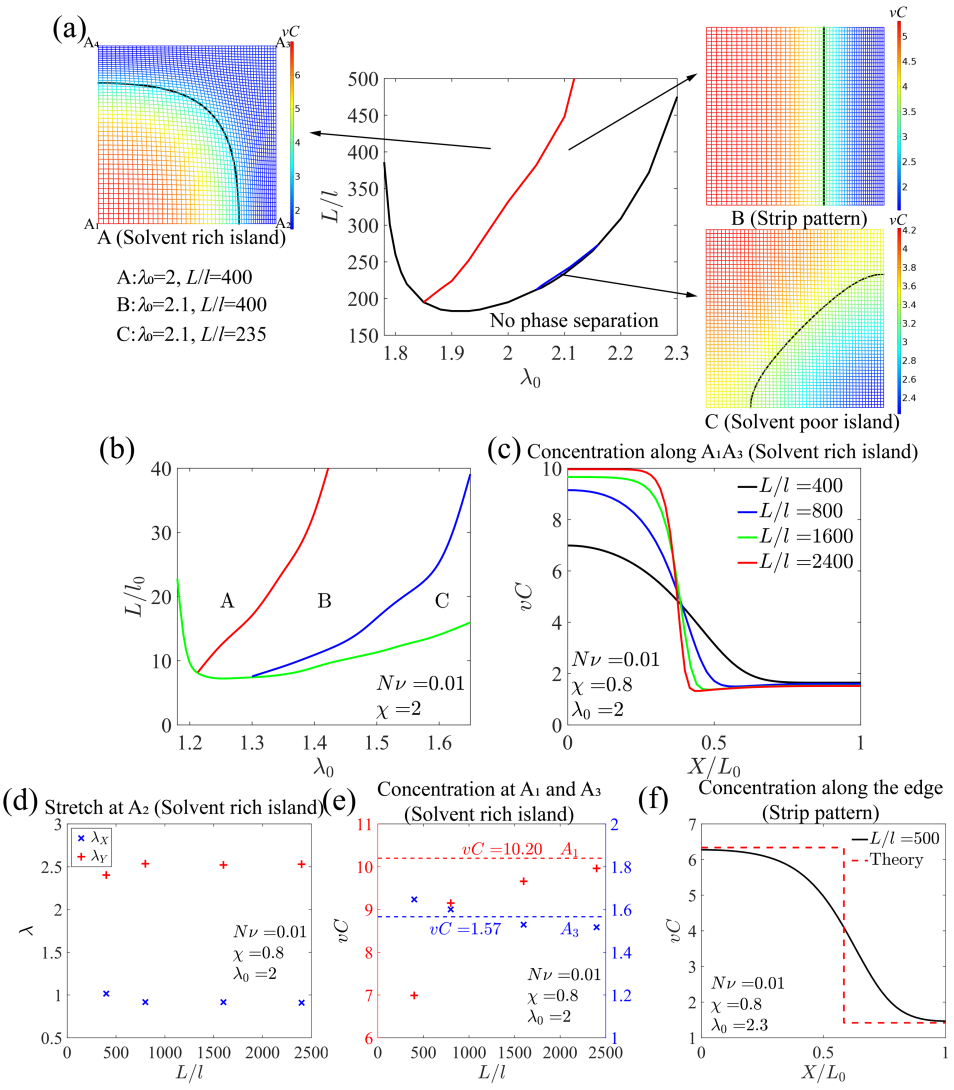

Figure 3.8 (a) L/l-λ_0 phase diagram of phase separation for $\chi = 0.8$. Three patterns, solvent rich island ($\lambda_0 = 2, L/l = 400$), strip ($\lambda_0 = 2.1, L/l = 400$), and solvent poor island ($\lambda_0 = 2.1, L/l = 235$) are shown in snapshots A, B and C, where the color bars represent the normalized concentration vC, and the black solid curves correspond to the initial concentrations. (b) L/l-λ_0 phase diagram of phase separation for $\chi = 2$. (c) The equilibrium distribution of concentration along the diagonal of the hydrogel in the solvent-rich-island pattern with different sizes of the hydrogel L/l and the initial stretch $\lambda_0 = 2$. (d) The stretch values in *X* and *Y* directions at corner A_2 in the solvent-rich-island pattern as functions of the sample size L/l. (e) The concentrations at corners A_1 and A_3 in the solvent-rich-island pattern as functions of the sample size L/l. The dashed lines are predicted by the common tangent construction. (f) The equilibrium distribution of concentration along the edge of the hydrogel in the strip pattern.

3.5 Phase Separation Induced by Quench and Stretch

Since phase separation of a hydrogel is limited by diffusion of solvent molecules, it is expected that the phase behavior of a hydrogel undergoing a phase transition depends on quenching and loading rates. As discussed in Section 3, quenching a hydrogel under a free swelling condition might induce temporary phase separation, while changing the interaction parameter χ slowly induces homogeneous deformation of the hydrogel without phase separation. Similarly, we anticipate and will show that stretching rates can also affect the volume phase transition of hydrogels. Investigating how quenching and stretching rates influence the response of hydrogels can help us explain some experimental phenomena and provide guidance for material and loading designs.

3.5.1 Influence of quenching rate

Here we demonstrate the effect of a quenching rate on phase separation using an example of a hydrogel under constrained uniaxial deformation. As Figure 3.9a shows, the hydrogel is expected to follow different deformation paths depending on the quenching rate. After the hydrogel is allowed to undergo one-dimensionally free swelling in a solvent to reach equilibrium initial stretch λ_0, the system is quenched by a sudden increase of parameter χ, which induces phase separation (Figure 3.9a). We consider a linear increase of χ from $\chi_0 = 0.5$ to $\chi_1 = 1.5$ within time t_1 prior to holding χ as a constant (Figure 3.9b). The initial system size is $L_1 = 500l$. Therefore, the diffusion time scale across the whole hydrogel is $L_1^2/D = 2.5 \times 10^5 t_0$, where t_0 is the diffusion time scale across the characteristic length l. At the two ends of the hydrogel, we impose the boundary conditions as

$$\begin{cases} u = 0, & \text{at } X = 0 \\ \sigma_{xx} = 0, & \text{at } X = L_0 \end{cases} \tag{3.23}$$

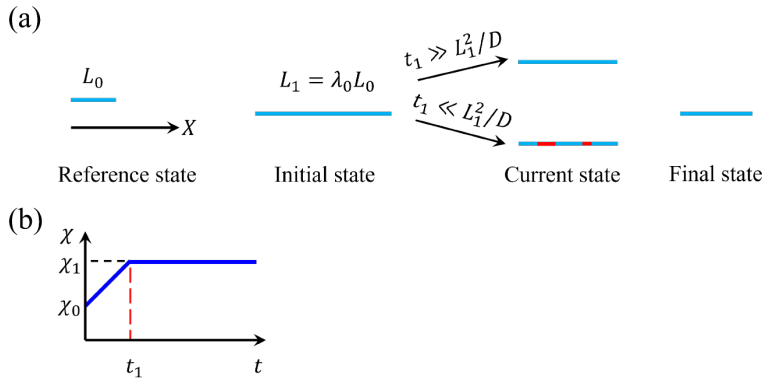

Figure 3.9 (a) Schematic of a hydrogel under constrained uniaxial deformation with different quenching rates. In the current state, the top schematic represents the hydrogel with a single phase when the loading time is much longer than the diffusion time across the whole sample $t_1 \gg L_1^2/D$,

and the bottom schematic represents the hydrogel undergoing phase separation when $t_1 \ll L_1^2/D$. In both cases, the hydrogel eventually reaches equilibrium and becomes homogeneous (final state). (b) Schematic of the change of χ as a function of time.

The evolution of stretch distribution along the length of the hydrogel is plotted at different time for different quenching rates ($t_1/t_0 = 10$ for Figure 3.10a and $t_1/t_0 = 5 \times 10^5$ for Figure 3.10b), where solvent diffuses out of the hydrogel through the two ends. When the quenching rate is higher, more domains are observed during the phase separation process. The maximum stretch (Figure 3.10c & d) and length change (Figure 3.10e & f) are plotted as functions of time for different quenching rates. Although the length monotonically increases with time, the maximum stretch can non-monotonically increase and decrease with time, attributed to phase separation, and the evolution of the swollen phase. The curves are rough under a high quenching rate, due to the coarsening of different domains, while the curves are smooth when the quenching rate is low. When the quenching rate is extremely low, namely t_1 is much larger than the diffusion time across the whole sample ($t_1 \gg L_1^2/D$), the hydrogel almost always reaches equilibrium and remains homogeneous with the change of χ (Figure 3.10d & f), which can be validated by the overlapping of the maximum stretch-time and length change-time curves with those predicted by Eq. (3.13). As a result, phase separation does not occur and the maximum stretch decreases monotonically (Figure 3.10d). Bai and Suzuki experimentally studied the influence of heating rates on the morphologies of weakly ionized PNIPAM hydrogels [110], where the increase of temperature is equivalent to the increase of the parameter χ. They observed that a low heating rate leads to a smooth surface of the hydrogel, while a high heating rate produces a rough surface, which agrees with our simulation results.

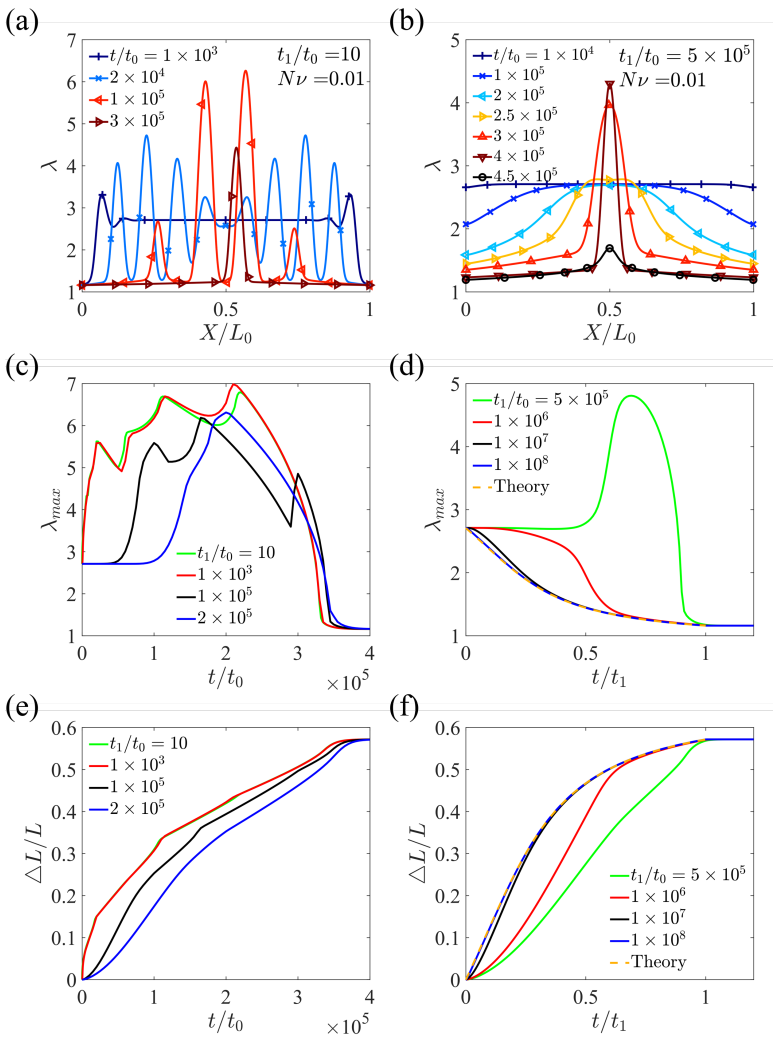

Figure 3.10 The evolution of stretch distribution along the length of the hydrogel at different time under quenching rates of (a) $t_1/t_0 = 10$ and (b) $t_1/t_0 = 500000$. The maximum stretch (c, d) and length change (e, f) as functions of time under different quenching rates.

3.5.2 Influence of stretching rate

We next study the effect of stretching rates on phase transition. A hydrogel first undergoes one-dimensionally free swelling in a solvent to reach equilibrium initial stretch λ_0 (Figure 3.11a). Then it is gradually stretched at a constant rate from the initial state ($L_1 = \lambda_0 L_0$) to the current state with

stretch λ_1 ($L_2 = \lambda_1 L_0$) under a constant χ (Figure 3.11a & b). After the stretch reaches $\lambda_1 = \lambda_m$ at $t = t_1$, it is gradually released to the initial state at the same rate until $t = 2t_1$ (Figure 3.11b). The total deformation gradient of the hydrogel with respect to the reference state is denoted as $\mathbf{F} = diag(\lambda, 1, 1)$.

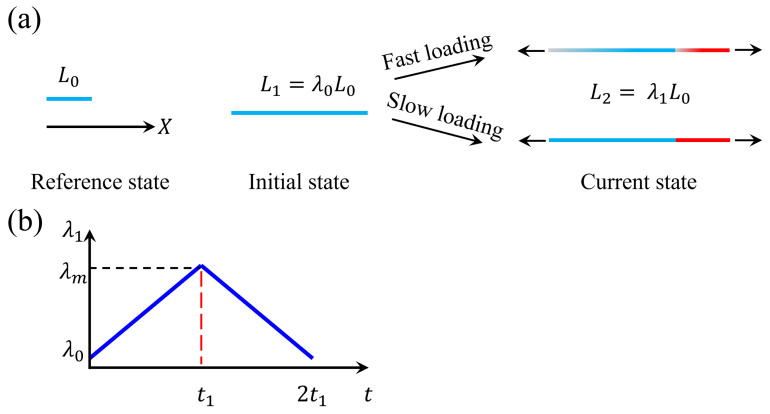

Figure 3.11 (a) Schematic of a hydrogel undergoing constrained uniaxial stretch in the reference, initial and current states. In the current state, the top schematic represents the hydrogel with two inhomogeneous phases when the loading is fast, and the bottom schematic represents the hydrogel with two homogeneous phases when the loading is slow. (b) Schematic of the applied stretch as a function of time.

We consider a hydrogel with $\chi = 1.5$ so that the equilibrium stretch is $\lambda_0 = 1.16$. Then the hydrogel is stretched to $\lambda_m = 20$ within t_1. We introduce a dimensionless parameter m defined as $m = t_1/(L_1^2/D)$, which characterizes how fast the loading is compared to diffusion across the sample. Assuming the ratio of the initial sample length to the interfacial characteristic length is $L_1/l = n$, we obtain $m = t_1/(n^2\, l^2/D) = t_1/(n^2 t_0)$. Here $n = 100$ is chosen in our simulations.

The stress-stretch curves are plotted under different stretching rates, where the blue and black curves represent the loading and unloading processes, respectively (Figure 3.12a & b), while the red solid curve is the homogenous equilibrium solution obtained from Eq. (3.13). As Figure 3.12a, b, c & d show, the hydrogel remains a shrunk phase when the applied stretch λ_1 is low. Upon a critical stretch that corresponds to the spinodal point (see Figure 3.3d, point c), the hydrogel becomes unstable, and the swollen phase appears and coexists with the shrunk phase. The shrunk phase gradually transits into the swollen phase as the applied stretch increases. Finally, the hydrogel becomes a single phase again before the applied stretch approaches the stretch value of the binodal point (see Figure 3.3d, point b). The equilibrium stress-stretch relation under the homogeneous assumption obtained in Eq. (3.13), where the hydrogel is either in the homogeneous shrunk or swollen phase, is used to compare with the numerical results from the phase-field model. When the loading is fast, the stress deviates from the equilibrium solution from Eq. (3.13) with a large hysteresis between loading and unloading (Figure 3.12a). Higher stress is required to drive the solvent into the hydrogel, while lower stress is needed during unloading. When the loading is slow, the numerical results agree with the theoretical prediction in a wide range of stretch (Figure 3.12b). A stress plateau is predicted by the numerical solution in both loading and unloading, and it overlaps with the stress obtained by the common tangent construction (the red dashed line in Figure 3.12b). Figure 3.12c & d demonstrate the stretch distributions at different applied stretches, where the solid blue lines correspond to the loading process and the dashed black lines correspond to the unloading process. The results show that a volume phase transition through phase separation is captured by the phase-field model. For a fast loading with $m = 10^3$, the swollen phase is highly inhomogeneous because it takes time for the diffusion of solvent molecules (Figure 3.12c). In

contrast, the stretch is more homogenously distributed for a slow loading with $m = 5 \times 10^4$ (Figure 3.12d). It is worth mentioning that m is defined based on the diffusion time scale in the initial state, $t_1/(L_1^2/D)$, instead of in the current state, $t_1/(L_2^2/D)$, which leads to the large value of m even for the case of slow loading.

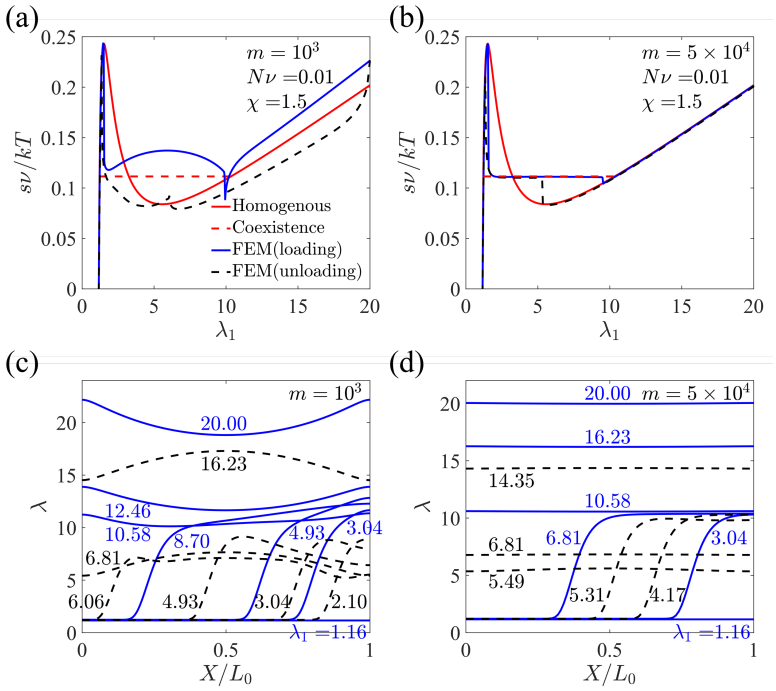

Figure 3.12 Loading, unloading and homogenous equilibrium stress-stretch curves for different ratios of the loading time to the diffusion time across the sample, (a) $m = 1000$ and (b) $m = 50000$. The red dashed line represents the stress and critical stretches obtained by the common tangent construction. Stretch distribution at different applied stretches in loading and unloading for (c) $m = 1000$ and (d) $m = 50000$, where the solid blue lines correspond to the loading process and the dashed black lines correspond to the unloading process.

Similarly, a hydrogel undergoing constrained biaxial deformation with the initial stretch λ_0 at zero stress is gradually stretched equi-biaxially under a constant χ from the initial state ($L_1 = \lambda_0 L_0$) to the current state with stretch λ_1 ($L_2 = \lambda_1 L_0$) in both X and Y directions (Figure 3.13). The initial system size is $L_1 = 50l$.

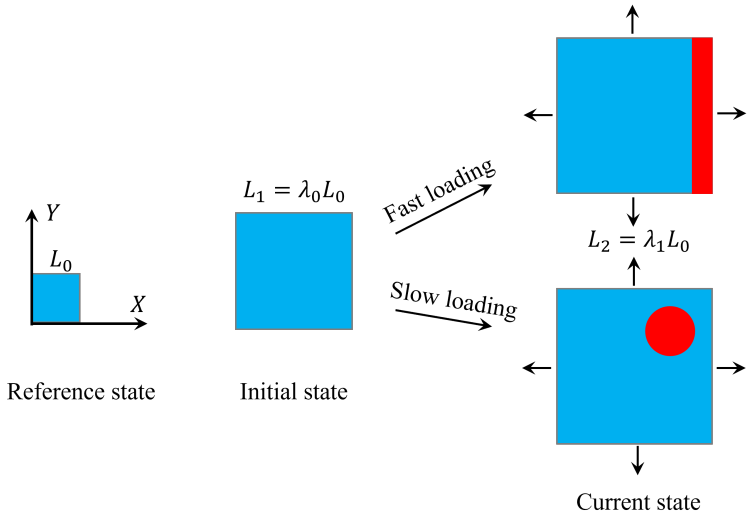

Figure 3.13 Schematic of a hydrogel undergoing constrained biaxial deformation in the reference, initial and current states. In the current state, different loading rates lead to different patterns of the hydrogel.

Figure 3.14a & b show the stress-stretch curves of the hydrogel under different stretching rates $m = 200$ and $m = 10^4$, where m is defined in the same way as that for the uniaxial case. The average nominal stresses along X and Y directions defined as $F_X v/L_0 kT$ and $F_Y v/L_0 kT$, where F_X and F_Y are the total forces on the surfaces in the X and Y directions, are plotted as functions of stretch λ_1 (Figure 3.14a & b). The homogeneous stress-stretch solution predicted by Eq. (3.7) is also plotted for comparison. During the loading process, the morphology evolves with

λ_1, as shown in Figure 3.14c & d, where the black lines represent the boundaries of the initial states. It is noted that different loading rates can lead to different paths of pattern evolution, where the transitions between different patterns lead to sharp changes of stresses (Figure 3.14a, b, c & d). When the loading is fast, the stress obtained from the simulation deviates from the equilibrium solution to Eq. (3.7) after phase separation, due to inhomogeneous solvent distributions. The stresses in the two directions are not equal attributed to the occurrence of the strip pattern (c_1), which eventually evolves to the solvent-poor-island pattern (c_2 & c_3) at high enough λ_1 (Figure 3.14a & c). In contrast, under a slow loading, the solvent-rich-island pattern (d_1) transits to the solvent-poor-island pattern (d_2) as λ_1 increases (Figure 3.14b & d). The morphology is always symmetric with respect to one diagonal, and the stresses in X and Y directions are equal (Figure 3.14b). The stress-stretch relations from the simulation overlap with the theoretical prediction when the hydrogel is either completely in the shrunk or swollen phase. The maximum and minimum concentrations of the hydrogel for different loading rates are plotted as functions of λ_1 for different loading rates (Figure 3.14e & f). When λ_1 is larger than a critical value, the hydrogel under slow loading becomes homogeneous again, with the maximum and minimum concentration almost equal (Figure 3.14f). In contrast, for a fast loading, the maximum concentration is still higher than the minimum concentration when λ_1 is above the critical value, since it takes longer time for solvent to diffuse into the hydrogel to achieve the equilibrium homogeneous state (Figure 3.14e).

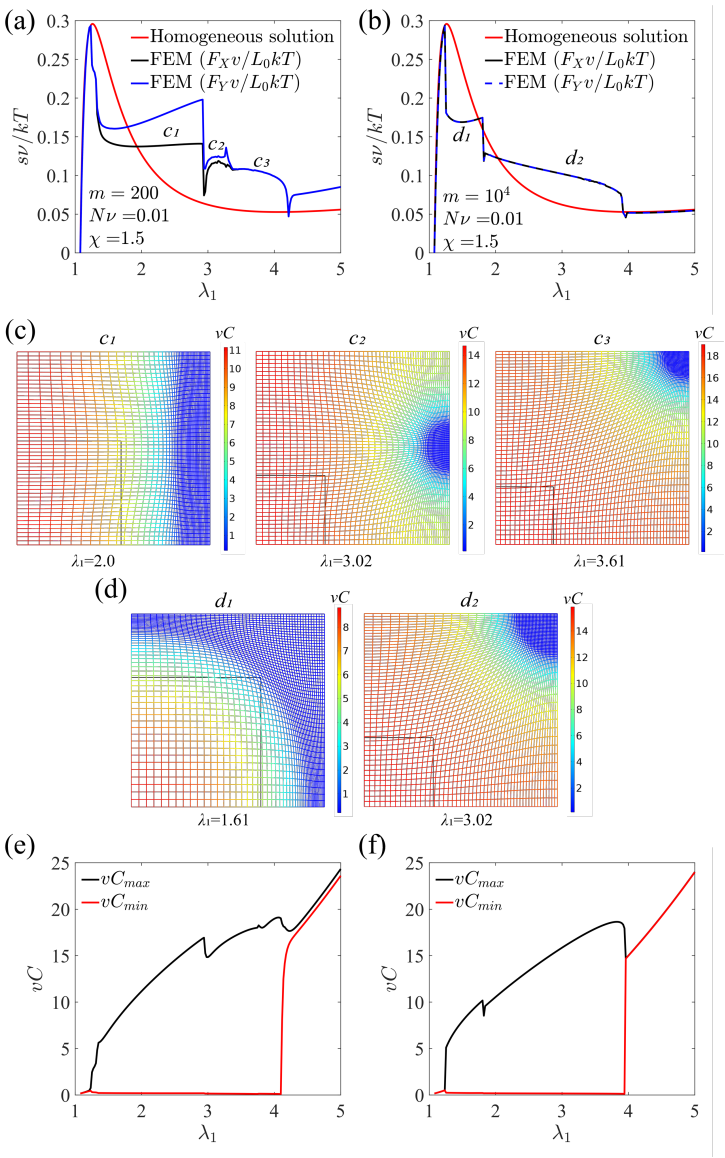

Figure 3.14 Dependence of the normalized stresses in the X and Y directions as functions of stretch λ_1 for the hydrogel subjected to different loading rates (a) $m = 200$ and (b) $m = 10000$. Contour plots of the solvent concentration at different stretches for (c) $m = 200$ and (d) $m = 10000$. Maximum and minimum solvent concentrations as functions of stretch λ_1 for (e) $m = 200$ and (f) $m = 10000$.

3.6 Conclusion

In this chapter, we reveal the underpinning role of mechanical constraints on triggering the volume phase transitions and phase separation of hydrogels. We show that even for a hydrogel that does not phase separate during equilibrium free swelling modeled by the Flory-Rehner free energy with a constant interaction parameter χ, multiple phases can coexist when the hydrogel is subjected to mechanical constraints. We obtain the states of equilibrium for the hydrogel under free swelling, hydrostatic loading, constrained uniaxial deformation, and constrained biaxial deformation, and unravel how mechanical constraints change the convexity of the free energy and monotonicity of the stress-stretch curves. In contrast to the existence of only one homogenous solution under equilibrium free swelling, coexistence of multiple solutions, corresponding to multiple phases, can occur in the hydrogel under the above mentioned mechanical constraints.

By introducing interfacial energy and kinetics of diffusion, we further develop a phase-field model to investigate the pattern evolution in the phase separation of hydrogels under mechanical constraints. For constrained uniaxial deformation, the common tangent construction predicts well the concentrations and fractions of coexisting phases when the hydrogel reaches equilibrium. For constrained biaxial deformation, the two separated phases have large strain misfit, and the homogeneous deformation determined by the common tangent construction is inaccurate, while the concentrations predicted agree quite well with the simulation results when the system size is large enough. As the system size decreases, simulation results deviate from the common tangent predictions. Moreover, the system could be stabilized by the interfacial energy, and phase separation can be suppressed.

We further study the effect of quenching rates and loading rates on the phase behavior of hydrogels. As a result, a quenching rate can significantly influence the pattern evolution of phase separation. Particularly, a fast quenching rate leads to more small domains, resulting in a temporary rough texture of the hydrogel. Although phase coexistence does not occur in a neutral hydrogel under free swelling, fast quenching can trigger temporary phase separation. Similarly, a stretching rate can also influence the pattern evolution of phase separation, and stress-stretch responses. A fast loading results in large hysteresis between loading and unloading stress-stretch curves, and deviation from the theoretical prediction.

Our theoretical predictions are to be experimentally validated. The effect of mechanical constraints on the phase separation of hydrogels that we predicted is consistent with some reported experiments. Matsuo and Tanaka demonstrated that cylindrical PAAm hydrogels immersed in an acetone solution with different concentrations show different stable patterns with coexistence of swollen and shrunk phases [43]. Even though PAAm hydrogels undergo continuous volume transitions [136], the high χ due to the high acetone concentration and the constant volume constraint induced by a dense impermeable skin layer on the surface of the hydrogels lead to phase separation of the hydrogels and morphology changes, consistent with our theory. Regarding the effect of loading rates on phase separation of hydrogels, Bai and Suzuki experimentally observed that heating a weakly ionized PNIPAM hydrogel via a low heating rate leads to a smooth surface of the hydrogel, while a high heating rate produces a rough surface [110], consistent with our simulations. However, experimental results that can be quantitatively compared with our theory are lacking. Since our theory is relatively general, we expect that many hydrogels under mechanical constraints can show rich phase behavior. We here call for more experimental studies

to quantify the phase separation of hydrogels under various mechanical constants and loading conditions.

In summary, our study successfully captures rich phase behavior of neutral hydrogels under different mechanical constraints and dynamic loading conditions. It provides design guidelines for hydrogels with a volume phase transition for various applications.

Chapter 4 A Modified Semisoft Model of Liquid Crystal Elastomers: Application to Elastic and Viscoelastic Responses

LCEs are emerging actuating materials composed of polymer networks and liquid crystal mesogens. A plateau in the stress-strain curve of LCEs, typical of the semisoft characteristics, is commonly observed. Although the classical semisoft model based on compositional fluctuations intends to capture this feature, it does not accurately predict the stress plateau. Moreover, the extended viscoelastic model performs inadequately in predicting stress, deformation, and director rotation. To address these limitations, we phenomenologically modify the semisoft model, applying it to both elastic and viscoelastic responses. The modified model is further implemented in finite element simulations and used to study intriguing inhomogeneous deformation of LCEs. We demonstrate more robust predictions of our model by comparison with experimental results.

4.1 Introduction

LCEs are combinations of polymer networks and liquid crystal mesogens. The coupling between polymer networks and mesogens leads to unusual mechanical properties of LCEs, such as semisoft elasticity and viscoelasticity [26]. LCEs can undergo large deformation in response to various external stimuli [27], including temperature [28], light [29], and electric fields [30]. mechanical stress [31]. As a result, LCEs have many potential applications, including energy dissipation [32-34], robotics [35, 36], actuation [37, 38], and so on.

Of particular interest are monodomain LCEs, where the mesogens are aligned in a certain direction, namely the director. A director can reorient in response to external loading. Bladon, Terentjev [137] proposed the neo-classical elastic energy to describe LCEs by considering the

anisotropy of the network. The energy could capture the soft elastic response, allowing a director to reorient towards a stretch direction under zero stress. A classical semisoft model was further proposed in [138], by adding a semisoft elastic energy term to the neo-classical elastic energy to explain the experimental observation that a finite, albeit small, stress is required to rotate the director, possibly due to variations in chain anisotropy [139]. The energy term has a constant coefficient, the semisoft parameter, to describe the degree of variations. Experimental results demonstrate that a LCE sample under uniaxial tension exhibits a plateau in the stress-stretch curves when the initial director and the loading direction are nearly perpendicular, i.e. the angle between them vary from 75 to 90 degrees [140]. However, the semisoft elasticity model fails to capture such a plateau when the angle deviates from 90 degrees. Here we address this limitation by modifying the semisoft elastic energy term, treating the original semisoft parameter as a function of deformation.

Meanwhile, LCEs are typical viscoelastic materials, and the mechanical responses are highly dependent on the loading rate [68, 141]. Several works have measured the stress, director rotation, and deformation in main-chain nematic LCEs with different initial directors subjected to uniaxial tension at various loading rates [68, 142]. It was shown that the relaxation of director orientation is rapid, with a characteristic timescale of approximately 0.1 seconds, whereas the relaxation time of the network is much larger [69]. Several viscoelastic models have been proposed to model the rate-dependent response. Zhang, Xuan [143] proposed a viscoelastic model that considers both the viscous network and director by adding dissipation terms as a function of the deformation rate and director rotation rate to the free energy. However, such a Kelvin-Voigt model is not suitable for accurately describing large deformation of the polymer network. Wang, Chehade

[70] developed a viscoelastic model using the multiplicative decomposition of the deformation gradient into elastic and viscoelastic parts, and attributed the semisoft effect to the viscous director reorientation. Their predictions have shown qualitative agreement with experiments, capturing the nonmonotonic stress response and stress plateau. Chung, Luo [69] further considered the evolution of the mesogen alignment degree, namely, the order parameter, influenced by the deformation, and applied their model to examine the LCE response under extremely high strain rates. Although they demonstrated good quantitative agreement between the model and experimental results, the model's reliance on empirical fitting between the modulus and director orientation could restrict its application to LCEs with simple deformations. A straightforward viscoelastic model that incorporates realistic parameters derived from experimental measurements remains elusive. Moreover, despite several numerical implementations pertaining to LCEs [143-147], a simple and effective finite element implementation capable of solving numerous equations related to the viscoelastic response of LCEs is still lacking.

In this work, we aim to model the semisoft elasticity and viscoelasticity of LCEs with experimental validation, implement the model in COMSOL, and provide benchmarks for complex deformations. The chapter is organized as follows. Section 2 introduces the experimental methodology and a general continuum framework for LCEs. In Section 3, we present the modified semi-soft model, study homogeneous deformation under uniaxial tension, and validate the elastic predictions. Section 4 extends the model to a framework that includes viscoelastic responses and demonstrates its predictability. Section 5 showcases inhomogeneous deformation of LCEs by the finite element method (FEM) via COMSOL and compares the predictions with our experimental results. Section 6 concludes the chapter.

4. 2 Experimental Methodology and Theoretical Framework

4.2.1 Material and specimen preparation

The main-chain monodomain LCEs were synthesized via a two-stage thiol-acrylate Michael addition-photopolymerization reaction [148]. The diacrylate mesogen, 1,4-Bis-[4-(3-arcyloyoxypropyloxy) benzoyloxy]-2-methylbenzene (RM257, 95%), crosslinker, pentaerythritol tetrakis(3-mercaptopropionate) (PETMP, 95%), chain extender, 2,2-(ethylenedioxy) diethanethiol (EDDET, 95%), catalyst, dipropylamine (DPA, 98%), and photoinitiator, (2-hydroxyethoxy)-2-methylpropiophenone (HHMP, 98%), were used. RM257 (6.4g) was first dissolved in toluene (4g) at 80 ℃ and then cooled to room temperature. EDDET (1.465g), PETMP (0.347g), HHMP (0.041), and DPA solution (0.768g, DPA:toluene = 1:50) were subsequently added to the solution, and thoroughly mixed using a vortex mixer at 3200 rpm for 5 mins. The solution was degassed, poured into a mold, and cured at room temperature for 24 hours. Then the cured film was placed in an oven at 80 ℃ for 24 hours to remove the solvent. Afterward, the film was stretched by two times and exposed to UV light for 1 hour for the second-stage crosslinking process, producing monodomain LCEs with the director in the stretching direction. We cut rectangular strips at different angles with respect to the stretching direction to obtain specimens of different initial directors (Figure 4.2a). A large length-to-width ratio (>5) is adopted to eliminate the boundary effect. The angle between the transverse direction of the specimen and initial director is defined as θ_0 (Figure 4.2a). For the tests of inhomogeneous deformation, a hole was cut from the rectangular specimens (Figure 4.5a).

4.2.2 Uniaxial test

We conducted uniaxial tension tests to LCEs using an Instron universal testing machine (Model 5944). A sample was clamped to two pneumatic grips. The applied stretch and nominal stress are denoted as λ and s, respectively. Experimental data were collected to validate the models in Sections 3 and 5. In Section 3 a relatively low strain rate $0.05\%/s$ was used to validate the elastic model, while in Section 5 strain rates ranged from $0.1\%/s$ to $10\%/s$ to study rate-dependent inhomogeneous deformation.

4.2.3 A general continuum model for LCEs

To model the elastic and viscoelastic responses of LCEs, we follow the approaches by Wang, Chehade [70] and Wei, Cao [68] with some modifications. Supposing a material point of the solid labeled with a coordinate $\mathbf{X}$ moves to a coordinate $\mathbf{x}$ in the current state at time t, the deformation gradient $\mathbf{F}$ is defined as $\mathbf{F} = \partial\mathbf{x}/\partial\mathbf{X}$. The director $\mathbf{n}$ is defined in the current state to describe the mesogen alignment. Since our stretching rate is limited below $10\%/s$ and the timescale for director relaxation is approximately 0.1s, the director is expected to undergo quasistatic reorientation. Therefore, we assume the viscosity originates from the polymer network rather than the director. To describe the viscoelastic response, we parallelly connect the Kelvin-Voigt model and Maxwell model with N branches (Figure 4.1). Compared to the classical generalized Maxwell model, an additional dashpot is added in parallel.

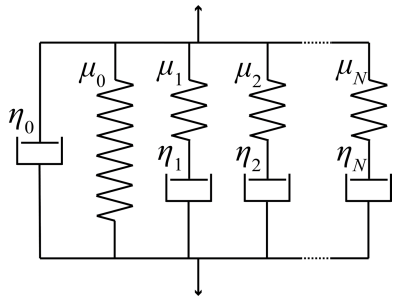

Figure 4.1 Schematic of the rheological model with a viscous branch, an equilibrium branch and N nonequilibrium branches.

In the Maxwell branches, the deformation gradient **F** is multiplicatively decomposed into the elastic part $\mathbf{F}_i^e$ and viscous part $\mathbf{F}_i^v$,

$$\mathbf{F} = \mathbf{F}_i^e \mathbf{F}_i^v \quad \text{for} \quad i = 1,2,\dots,N, \tag{4.1}$$

The free energy density of the material is formulated as a function of the state variables **F**, $\mathbf{F}_i^v$ and **n**,

$$\psi(\mathbf{F}, \mathbf{F}_i^v, \mathbf{n}) = \psi_0(\mathbf{F}, \mathbf{n}) + \sum_{i=1}^{N} \psi_i(\mathbf{F}\mathbf{F}_i^{v-1}, \mathbf{n}), \tag{4.2}$$

where ψ_0 and ψ_i are the free energy densities of the equilibrium branch and nonequilibrium branches, respectively.

Considering an isothermal process and neglecting the body force, the energy balance of the system is

$$\int \dot{\psi} dV + \int \dot{\phi} dV = \int \mathbf{t} \cdot \dot{\mathbf{x}} dA, \tag{4.3}$$

where $\dot{\phi}$ is the dissipated energy per unit time and per unit volume through viscous deformation, **t** is the traction acting on the surface. The thermodynamics requires that the dissipated energy shouldn't decrease, namely, $\dot{\phi} \geq 0$. The dissipation rate is contributed by all the dashpots,

$$\dot{\phi}\left(\dot{\mathbf{F}}, \dot{\mathbf{F}}_i^v\right) = \dot{\phi}_0\left(\dot{\mathbf{F}}\right) + \sum_{i=1}^{N} \dot{\phi}_i\left(\dot{\mathbf{F}}_i^v\right), \tag{4.4}$$

where we assume

$$\dot{\phi}_0\left(\dot{\mathbf{F}}\right) = \frac{\partial \varphi_0\left(\dot{\mathbf{F}}\right)}{\partial \dot{\mathbf{F}}} : \dot{\mathbf{F}}, \tag{4.5}$$

and

$$\dot{\phi}_i\left(\dot{\mathbf{F}}_i^v\right) = \frac{\partial \varphi_i\left(\dot{\mathbf{F}}_i^v\right)}{\partial \dot{\mathbf{F}}_i^v} : \dot{\mathbf{F}}_i^v \ . \tag{4.6}$$

The terms φ_0 and φ_i are usually referred to as the dissipation potential [149].

Organizing Eqs. (4.1-6), we obtain

$$\begin{aligned} &\int \left[-\mathrm{Div}\left(\frac{\partial \psi}{\partial \mathbf{F}} + \frac{\partial \varphi_0}{\partial \dot{\mathbf{F}}} \right) \cdot \dot{\mathbf{x}} + \sum_{i=1}^{N} \left(\frac{\partial \psi_i}{\partial \mathbf{F}_i^v} + \frac{\partial \varphi_i}{\partial \dot{\mathbf{F}}_i^v} \right) : \dot{\mathbf{F}}_i^v + \frac{\partial \psi}{\partial \mathbf{n}} \cdot \dot{\mathbf{n}} \right] \mathrm{d}V \\ &+ \int \left[\left(\frac{\partial \psi}{\partial \mathbf{F}} + \frac{\partial \varphi_0}{\partial \dot{\mathbf{F}}} \right) \cdot \mathbf{N} - \mathbf{t} \right] \cdot \dot{\mathbf{x}} \mathrm{d}A = 0 \end{aligned}, \tag{4.7}$$

where Div denotes the gradient with respect to **X**, and **N** is the unit outward-pointing normal vector. Utilizing the energy balance Eq. (4.7), and the independence of **x**, $\mathbf{F}_i^v$ and **n**, the mechanical equilibrium equation, the evolution of $\mathbf{F}_i^v$, and the equilibrium equation for the director **n** are obtained as follows. By defining the nominal stress **P** as

$$\mathbf{P} = \frac{\partial \psi}{\partial \mathbf{F}} + \frac{\partial \varphi_0}{\partial \dot{\mathbf{F}}}, \tag{4.8}$$

we obtain the mechanical equilibrium and the corresponding boundary condition as

$$\mathrm{Div}\mathbf{P} = 0, \tag{4.9}$$

and

$$\mathbf{P} \cdot \mathbf{N} = \mathbf{t}. \tag{4.10}$$

The evolution of $\mathbf{F}_i^v$ is

$$\frac{\partial \psi}{\partial \mathbf{F}_i^v} + \frac{\partial \varphi_i}{\partial \dot{\mathbf{F}}_i^v} = 0. \tag{4.11}$$

Noticing $\dot{\mathbf{n}}$ cannot be arbitrary due to the relation $\mathbf{n} \cdot \mathbf{n} = 1$, the constraint $\mathbf{n} \cdot \dot{\mathbf{n}} = 0$ must be satisfied. Introducing a Lagrange multiplier $\lambda_{\mathbf{n}}$ to enforce the constraint, we obtain

$$\left(\frac{\partial \psi}{\partial \mathbf{n}} + \lambda_{\mathbf{n}} \mathbf{n} \right) \cdot \dot{\mathbf{n}} = 0, \tag{4.12}$$

and thus,

$$\frac{\partial \psi}{\partial \mathbf{n}} + \lambda_{\mathbf{n}} \mathbf{n} = \mathbf{0}. \tag{4.13}$$

Multiplying the above equation with $\mathbf{n}$, we obtain $\lambda_{\mathbf{n}} = -\frac{\partial \psi}{\partial \mathbf{n}} \cdot \mathbf{n}$. Therefore, the equilibrium equation for the director is

$$\frac{\partial \psi}{\partial \mathbf{n}} = \left(\frac{\partial \psi}{\partial \mathbf{n}} \cdot \mathbf{n} \right) \mathbf{n}. \tag{4.14}$$

In summary, the mechanical equilibrium Eq. (4.9), the constitutive relation Eq. (4.8), the traction boundary condition Eq. (4.10), the evolution of the viscous state variable Eq. (4.11), and the equilibrium equation for the director Eq. (4.14) provide the closed-loop equations necessary to predict the temporal behavior of LCEs subjected to external loading. To solve the equations described above, both the free energy density and the dissipation potential need to be explicitly specified.

4.3 Elastic Response

In this section, we analyze the elastic response of LCEs. We begin by specifying the free energy densities for the equilibrium branch and then apply the model to study homogeneous deformation of a LCE film subjected to uniaxial tension.

4.3.1 A modified semisoft free energy

We only consider the equilibrium brunch for the elastic response. To predict the elastic response of LCEs more accurately, we slightly modify the free energy function proposed by Verwey and Warner [138].

$$\begin{aligned}\psi_0 = &\frac{1}{2}\mu_0\left[tr\left(\mathbf{l}^{-1}\mathbf{F}\mathbf{l}_0\mathbf{F}^T\right)-3-2\log\left(\det\mathbf{F}\right)\right]+\mu_\alpha\left[tr\left(\mathbf{l}^{-1}\mathbf{F}\mathbf{l}_0\mathbf{F}^T\right)-3\right]^2 \\ &+\frac{1}{2}\mu_0 a\left\|\mathbf{n}_\mathbf{F}\right\|^2+\frac{1}{2}K\left(\det\mathbf{F}-1\right)^2\end{aligned}. \tag{4.15}$$

The first term in the free energy, $\frac{1}{2}\mu_0\left[\ tr\left(\mathbf{l}^{-1}\mathbf{F}\mathbf{l}_0\mathbf{F}^T\right)\right]$, is the neo-classical free energy, where μ_0 is the shear modulus, $\mathbf{l}=(r-1)\mathbf{n}\otimes\mathbf{n}+\mathbf{I}$ is the dimensionless shape tensor, and $\mathbf{l}_0=(r-1)\mathbf{n}_0\otimes\mathbf{n}_0+\mathbf{I}$ is the dimensionless initial shape tensor, with r representing the average shape

anisotropy of the network distribution, $\mathbf{n}_0$ the initial director, and $\mathbf{I}$ the identity tensor. Adding the term $\frac{1}{2}\mu_0\left[3-2\log(\det\mathbf{F})\right]$ ensures the total free energy and stress are both zero when $\mathbf{F}=\mathbf{I}$. The term $\mu_\alpha\left[\, tr\left(\mathbf{l}^{-1}\mathbf{F}\mathbf{l}_0\mathbf{F}^T\right)-3\right]^2$ accounts for material stiffening at large deformations, where μ_α is the coefficient of nonlinear elasticity. The next term, $\frac{1}{2}\mu_0 a\left\|\mathbf{n}_\mathbf{F}\right\|^2$, describes the nonideal part due to compositional fluctuation, where a is the semisoft parameter that indicates the degree of chain anisotropy variation, and $\|\mathbf{n}_\mathbf{F}\|^2 = tr[\mathbf{n}\otimes\mathbf{n}\cdot\mathbf{F}(\mathbf{I}-\mathbf{n}_0\otimes\mathbf{n}_0)\mathbf{F}^T]$. The last term represents the bulk energy, controlling compressibility, with K the bulk modulus.

In order to capture the plateau in the stress-strain curves when the initial director and the loading direction are nearly perpendicular, we propose to model a as a function of deformation, instead of a constant, based on the following rationale. From the compositional fluctuation model, the semisoft parameter is given by $\langle 1/r\rangle - 1/\langle r\rangle$, where r is directly related to the mesogen order parameter, and a larger r means better mesogen alignment [138]. Literature shows that the order parameter varies with deformation and this variation is rate-dependent [69, 142]. Supposing r increases from r_0 to $k\cdot r_0$ $(k>1)$, the semisoft parameter decreases from $\langle 1/r_0\rangle - 1/\langle r_0\rangle$ to $(\langle 1/r_0\,\rangle - 1/\langle r_0\,\rangle)/k$. Therefore, a is expected to decrease when a LCE sample is stretched. For simplicity, we don't model the evolution of r. Instead, we treat r as a constant and model a as a function of deformation. The variation degree of chain anisotropy is the strongest at the onset of deformation and the semi-soft elastic contribution gradually weakens when a LCE is further deformed. Here, we assume

$$a = a_t + a_p, \tag{4.16}$$

where a_p is a constant contribution, and

$$a_t = \frac{a_0}{m\left[tr\left(\mathbf{F}^T\mathbf{F}\right)-3\right]+1}, \tag{4.17}$$

is the transient part of the semisoft parameter, with a_0 the semisoft constant without deformation and m a positive scaling factor. The model recovers the conventional semisoft model when a_0 or m equals zero. Supposing a LCE is stretched to the same deformation state at different stretching rates, a should decrease more for slower stretching rates, and the corresponding m should be larger. Nonetheless, we treat m as a constant in this work.

It is important to note that the original free energy is nonconvex [150]. Microstructures such as stripe domains can be predicted when the loading axis is nearly perpendicular to the initial director [151]. Domain walls could also form when a LCE sample is under complex loading conditions, such as near a crack tip [144]. When treating a as a decreasing function of deformation, the free energy may become more nonconvex. To avoid erroneous results, parameters related to a should be chosen carefully.

The nominal stress can be derived from the free energy as

$$\mathbf{P} = \mu_0\left[g_0\mathbf{l}^{-1}\mathbf{F}\mathbf{l}_0 - \mathbf{F}^{-T} + a\mathbf{n}\otimes\mathbf{n}\cdot\mathbf{F}\left(\mathbf{I}-\mathbf{n}_0\otimes\mathbf{n}_0\right) - m\left(a_t^2/a_0\right)\left\|\mathbf{n}_\mathbf{F}\right\|^2\mathbf{F}\right] + KJ\left(J-1\right)\mathbf{F}^{-T}, \tag{4.18}$$

where $g_0 = 1+4\left(\mu_\alpha/\mu_0\right)\left[tr\left(\mathbf{l}^{-1}\mathbf{F}\mathbf{l}_0\mathbf{F}^T\right)-3\right]$ describes the increasing stiffness with deformation, and $J = \det\mathbf{F}$ represents the volume change. It is evident from the stress expression that the

contribution of the transient part of the semisoft contribution to the stress will diminish as the deformation increases.

The derivative of the free energy with respect to the director is

$$\frac{\partial \psi_0}{\partial \mathbf{n}} = \mu_0 \left[g_0 \left(\frac{1}{r} - 1 \right) \mathbf{F} \mathbf{l}_0 \mathbf{F}^T \mathbf{n} + a \mathbf{F} \left(\mathbf{I} - \mathbf{n}_0 \otimes \mathbf{n}_0 \right) \mathbf{F}^T \mathbf{n} \right]. \tag{4.19}$$

4.3.2. Uniaxial tension with homogeneous deformation

We study a LCE film subjected to homogeneous uniaxial tension (Figure 4.2). The deformation gradient is expressed as

$$\mathbf{F} = \begin{bmatrix} \lambda_{11} & 0 & 0 \\ \lambda_{21} & \lambda & 0 \\ 0 & 0 & \lambda_{33} \end{bmatrix}, \tag{4.20}$$

where λ_{11}, λ, λ_{33} are the stretches in X, Y and Z directions, respectively, and λ_{21} is the shear stretch due to director rotation. The director is related to the angle θ via $\mathbf{n} = [\cos\theta, \sin\theta, 0]$. Combined with the conditions that the stress P_{11}, P_{21}, and P_{33} vanish, the deformation and director can be numerically solved through Eqs. (4.10) and (4.14) using Matlab. We assume the LCE is nearly incompressible, $K/\mu_0 \gg 1$.

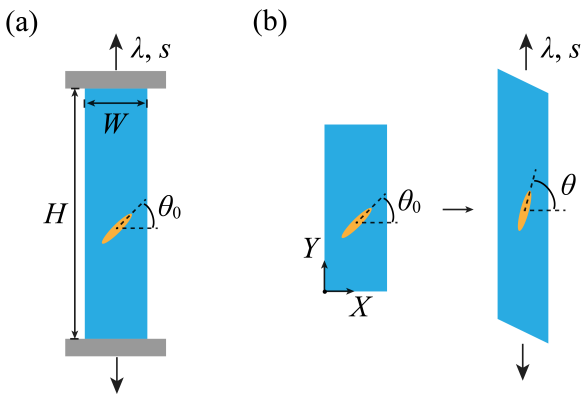

Figure 4.2 (a) Schematic of a LCE film under uniaxial external tension. (b) Schematic configurations of a LCE film before and after a homogeneous deformation under uniaxial tensile stress, with the director angles θ_0 and θ, respectively.

We first compare the theoretical predictions with experimental results. The shear modulus is obtained from the uniaxial test of a LCE sample with an initial angle $\theta_0 = 90°$ (Figure 4.3a). A small initial angle $\theta_0 = 15°$ is of particular interest to validate our model (Figure 4.3b). Theoretical predictions using different forms of a are compared with experimental results, where the black circles represent experimental data and solid lines are obtained from the theoretical model (Figure 4.3b). The parameters used in the model are listed in Table 4.1. A nonmonotonic stress-stretch curve and a stress plateau are clearly observed in experiments. The neo-classical model ($a = 0$) predicts a zero stress plateau, which significantly deviates from the experimental results. The stress from the semisoft model ($a = a_p$) increases monotonically and the model fails to capture the stress plateau. In contrast, the modified semisoft model successfully captures the initial high stiffness and the stress plateau of the semisoft response, aligning well with the experimental

observations. The model is further validated with different initial directors, showing better predictions compared to the original semisoft model (Figure 4.3c). It's also noted that the stress for $\theta_0 = 15°$ is larger than that of $\theta_0 = 30°$ and $45°$ at a low stretch, whereas the stress for $\theta_0 = 15°$ is smaller at a high stretch. A higher stress for smaller θ_0 at low stretch is due to the penalization of the semisoft elasticity, and a lower for smaller θ_0 at high stretch is due to higher spontaneous strain and more director rotation.

The influence of parameter m on stress, shear deformation and director is further investigated (Figure 4.3d, e & f). The initial angle θ_0 is set to be 15° and r is set to be 5. As shown in Figure 4.3d, the model predicts the same initial stiffness for different m when a_0 and a_p are fixed. The stress as well as shear deformation approaches the same value for different positive m ($m > 0$), and the director aligns with the loading axis when the stretch is large. The parameter m controls how fast a_t decays to 0, with a larger m leading to a smaller stress value under a given applied stretch. It's noted that when $m = 0$ and $a_0 > 0$, a becomes a constant $a_0 + a_p$ and the stress and shear deformation approach different values compared to those with $m > 0$. A nonmonotonic stress-stretch curve is predicted for a large m value, indicating the nonconvexity of the free energy and the potential prediction of phase coexistence along the longitudinal direction. To avoid possible impractical theoretical predictions and numerical errors, parameters resulting in a monotonic stress response under homogeneous deformation are suggested.

Table 4.1 Different parameter sets for elastic responses

Parameter set	μ_0 (MPa)	r	a_0	a_p	m	μ_α
P1	0.7	5	0.095	0.045	2	0
P2	0.7	5	0	0.045	N/A	0

P3	0.7	4.2	0	0	N/A	0

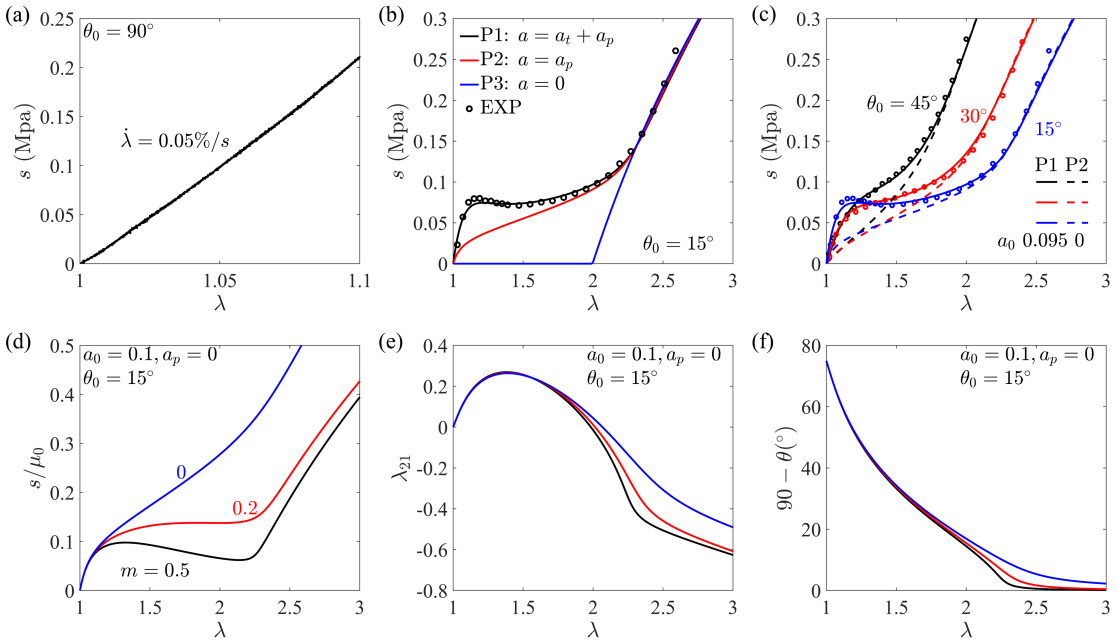

Figure 4.3 Theoretical predictions for elastic responses of LCEs under uniaxial tension compared with experimental results. (a) Experimental stress-stretch curves for a LCE sample with $\theta_0 = 90°$. (b) Stress-stretch curves obtained from experiments and theoretical models with different forms of a. (c) Stress-stretch curves for different initial directors. Influence of parameter m on the (d) stress, (e) shear stretch and (f) director rotation as functions of the stretch.

4.4 Viscoelastic Response

In this section, we apply the modified semisoft free energy to study the viscoelastic response, including the contribution of the nonequilibrium branch in the free energy. We first derive the constitutive relation and evolution equation of $\mathbf{F}_i^v$, and then apply the model to investigate the rate-dependent homogeneous deformation of LCEs under uniaxial tension.

4.4.1 Constitutive relation and evolution equation

The free energy density for the nonequilibrium branch (Figure 4.1) is assumed to follow a form similar to that of the equilibrium branch, and is expressed as

$$\begin{aligned}\psi_i = &\frac{1}{2}\mu_i\left\{\left[tr\left(\mathbf{I}^{-1}\mathbf{F}_i^e\mathbf{l}_0\mathbf{F}_i^{eT}\right)-3-2\log\left(\det\mathbf{F}_i^e\right)\right]+2\frac{\mu_\alpha}{\mu_0}\left[tr\left(\mathbf{I}^{-1}\mathbf{F}_i^e\mathbf{l}_0\mathbf{F}_i^{eT}\right)-3\right]^2\right\},\\ &+\frac{1}{2}\mu_i a_i\left\|\mathbf{n}_{\mathbf{F}_i^e}\right\|^2+\frac{1}{2}K_i\left(\det\mathbf{F}_i^e-1\right)^2\end{aligned} \tag{4.21}$$

where $a_i = a_{ti} + a_p = \dfrac{a_0}{m\left[tr\left(\mathbf{F}_i^{eT}\mathbf{F}_i^e\right)-3\right]+1} + a_p$.

The dissipation potentials are assumed to be

$$\varphi_0 = \frac{1}{8}\eta_0 J\left(\dot{\mathbf{F}}\mathbf{F}^{-1}+\mathbf{F}^{-T}\dot{\mathbf{F}}^T\right):\left(\dot{\mathbf{F}}\mathbf{F}^{-1}+\mathbf{F}^{-T}\dot{\mathbf{F}}^T\right), \tag{4.22}$$

and

$$\varphi_i = \frac{1}{2}\eta_i\left(\dot{\mathbf{F}}_i^v\mathbf{F}_i^{v-1}\right):\left(\dot{\mathbf{F}}_i^v\mathbf{F}_i^{v-1}\right). \tag{4.23}$$

We assume that the viscosity η_i changes nonlinearly with deformation and it follows the relation $\eta_i = \eta_{i,0}g_0$ $(i = 0,1,\ldots,N)$, where $\eta_{i,0}$ is a constant.

Combining Eqs. (4.8) (4.15) (4.21) and (4.22), the nominal stress is obtained as

$$\begin{aligned}\mathbf{P} = &\mu_0\left[g_0\mathbf{I}^{-1}\mathbf{F}\mathbf{l}_0-\mathbf{F}^{-T}+a\mathbf{n}\otimes\mathbf{n}\cdot\mathbf{F}\left(\mathbf{I}-\mathbf{n}_0\otimes\mathbf{n}_0\right)-m\left(a_t^2/a_0\right)\left\|\mathbf{n}_\mathbf{F}\right\|^2\mathbf{F}\right]+KJ(J-1)\mathbf{F}^{-T}\\ &+\frac{1}{2}\eta_0 J\left(\dot{\mathbf{F}}\mathbf{F}^{-1}+\mathbf{F}^{-T}\dot{\mathbf{F}}^T\right)\mathbf{F}^{-T}+\sum_{i=1}^{N}\begin{bmatrix}\mu_i\left(g_i\mathbf{I}^{-1}\mathbf{F}_i^e\mathbf{l}_0-\mathbf{F}_i^{e-T}+a_i\mathbf{n}\otimes\mathbf{n}\cdot\mathbf{F}_i^e\left(\mathbf{I}-\mathbf{n}_0\otimes\mathbf{n}_0\right)\right)\\ -m\mu_i\left(a_{ti}^2/a_0\right)\left\|\mathbf{n}_{\mathbf{F}_i^e}\right\|^2\mathbf{F}_i^e+K_iJ_i^e\left(J_i^e-1\right)\mathbf{F}_i^{e-T}\end{bmatrix}\mathbf{F}_i^{v-T},\end{aligned} \tag{4.24}$$

where $g_i = 1+4\left(\mu_\alpha/\mu_0\right)\left[tr\left(\mathbf{l}^{-1}\mathbf{F}_i^e\mathbf{l}_0\mathbf{F}_i^{eT}\right)-3\right]$ and $J_i^e = \det\mathbf{F}_i^e$.

Utilizing Eqs. (4.11) (4.21) and (4.23), the evolution of $\mathbf{F}_i^v$ is

$$\dot{\mathbf{F}}_i^v = \frac{\mu_i}{\eta_i}\begin{bmatrix} g_i\mathbf{F}_i^{eT}\mathbf{l}^{-1}\mathbf{F}_i^e\mathbf{l}_0\mathbf{F}_i^v - \mathbf{F}_i^v + a_i\left(\mathbf{F}_i^{eT}\mathbf{n}\otimes\mathbf{F}^T\mathbf{n} - \left(\mathbf{F}_i^{eT}\mathbf{n}\cdot\mathbf{n}_0\right)\mathbf{F}_i^{eT}\mathbf{n}\otimes\mathbf{F}_i^{vT}\mathbf{n}_0\right) \\ -m\left(a_{ti}^2/a_0\right)\left\|\mathbf{n}_{\mathbf{F}_i^e}\right\|^2\mathbf{C}_i^e\mathbf{F}_i^v + \dfrac{K_i}{\mu_i}J_i^e\left(J_i^e-1\right)\mathbf{F}_i^v \end{bmatrix}. \tag{4.25}$$

Denoting the relaxation timescale $\tau_i = \eta_{i,0}/\mu_i$, the evolution equation (4.25) is rewritten as

$$\begin{aligned}\tau_i g_0\dot{\mathbf{F}}_i^v = {} & g_i\mathbf{F}_i^{eT}\mathbf{l}^{-1}\mathbf{F}_i^e\mathbf{l}_0\mathbf{F}_i^v - \mathbf{F}_i^v + a_i\left(\mathbf{F}_i^{eT}\mathbf{n}\otimes\mathbf{F}^T\mathbf{n} - \left(\mathbf{F}_i^{eT}\mathbf{n}\cdot\mathbf{n}_0\right)\mathbf{F}_i^{eT}\mathbf{n}\otimes\mathbf{F}_i^{vT}\mathbf{n}_0\right) \\ & -m\left(a_{ti}^2/a_0\right)\left\|\mathbf{n}_{\mathbf{F}_i^e}\right\|^2\mathbf{C}_i^e\mathbf{F}_i^v + \frac{K_i}{\mu_i}J_i^e\left(J_i^e-1\right)\mathbf{F}_i^v\end{aligned}. \tag{4.26}$$

4.4.2. Uniaxial tension with homogeneous deformation

In this section, we predict the response of LCEs under uniaxial tension at different rates, and compare the theoretical results with our previous experiments [68]. We determine the viscosity parameters using the stress relaxation test of a sample with $\theta_0 = 90°$, where the relaxation follows a power law $s = 1.99t^{-0.4} + 0.89$. Since the loading rate we consider ranges from 0.1%/s to 10%/s, we select the timescales from 0.2s to 336s, shown in Table 4.2. The relaxation modulus is expressed as

$$\mu(t) = \mu_0 + \sum_{i=1}^{N}\mu_i\cdot e^{-\frac{t}{\tau_i}}. \tag{4.27}$$

The fitted moduli of nonequilibrium branches are listed in Table 4.2. The equilibrium shear modulus and other parameters are detailed in Table 4.3.

Table 4.2 Viscosity parameters for uniaxial tension with homogeneous deformation

$\tau_i(s)$	0.2	1	6	42	336
μ_i/μ_0	2.641959	1.526881	0.838750	0.383747	0.237739

Table 4.3 Remaining material parameters for uniaxial tension with homogeneous deformation

μ_0(MPa)	r	a_0	a_p	m	K/μ_0	K_i/μ_i	$\eta_{0,0}$(MPa · s)	μ_α
1.591	5.5	0.08	0	0.3	1000	1000	1.6	$1/16$

We analyze homogeneous deformation of an LCE film with a tilted initial director subjected to uniaxial tension at various stretching rate (Figure 4.2b). The mechanical balance (4.10), director equilibrium (4.14) and the evolution of inelastic deformation $\mathbf{F}_i^v$ (4.26) are directly solved using the Distributed ODEs and DAEs Interfaces in COMSOL. We investigate how different loading rates influence the mechanical response. As shown in Figure 4.4, the director rotates towards the stretching direction, inducing a semisoft stress-strain response and large shear deformation. The solid lines are predictions from our viscoelastic model based on the modified semisoft free energy, the dash lines are obtained from the classical semisoft model, and the circles represent experimental data extracted from our previous paper [68]. As expected, higher loading rates result in higher stress. The stress predictions agree well with the experiments under different stretching rate. It is also noted from the experiments that the semisoft region is larger at a lower stretching rate, which could be attributed to higher average shape anisotropy r at a lower stretching rate. Our model shows good prediction of the shear stretch and director orientation at the lower stretching rate. Yet it underestimates the shear deformation at a higher loading rate, potentially due to missing the evolution of r in reality. The theoretical prediction shows that as the stretching rate increases,

both the shear stretch and director rotation decrease because of the delayed response of the director rotation, consistent with the experimental observations. Compared to the conventional semisoft model ($m = 0$), our model achieves larger shear stretch and director rotation for a given applied stretch, and agrees with the experiments better.

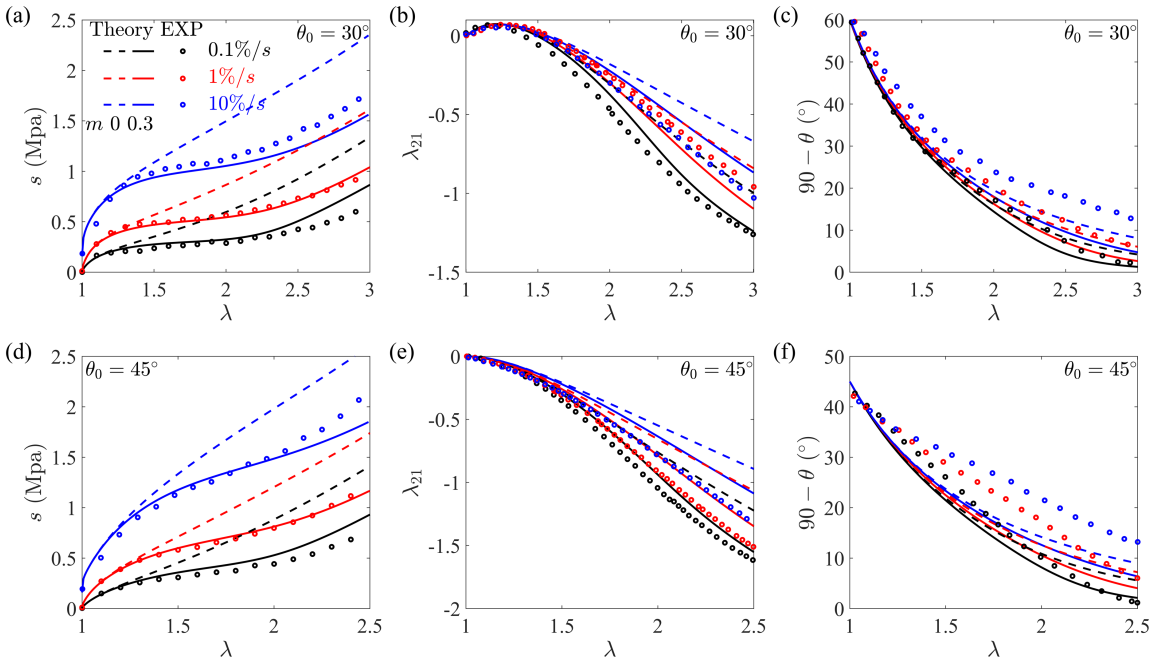

Figure 4.4 Theoretical predictions for viscoelastic responses of LCEs under uniaxial tension compared with experimental results. Dependence of (a)(d) nominal stress, (b)(e) shear stretch and (c)(f) director orientation on external stretch under different stretching rates and initial directors. The experimental data are extracted from our previous paper [68].

4.5 Inhomogeneous Deformation

In this section, we examine the inhomogeneous deformation of a LCE film with a slightly off-center hole subjected to an external uniaxial tension (Figure 4.5a). We first analyze the overall

stress, deformation, and director response under varying loading rates. We then discuss the simulation results using different mesh sizes.

4.5.1 Uniaxial tension of an LCE film with an off-center hole

The sample, with a tilted initial director, is subjected to uniaxial tension at different stretching rates. Cartesian coordinates are defined in the reference configuration (X, Y) and current configuration (x, y). The geometry parameters of the film are defined as: $H = 36mm$, $W = 12mm$, $R = 2.5mm$, and $W_1 = 5.65mm$. The initial director, as depicted in the schematic, is $\theta_0 = 45°$. The viscosity parameters are obtained from a relaxation test of a long LCE rectangular film with $\theta_0 = 90°$. The sample is stretched to 20% strain in 0.1s and held for 3600s. Figure 5b shows the relaxation curve, where the black dots represent experimental data and the red line is fitted through Eq. (4.27). The fitted viscosity parameters as listed in Table 4.4, with additional parameters listed in Table 4.5.

The viscoelastic model under the plane stress condition is implemented in COMSOL. The mechanical equilibrium (4.9), plane stress condition, and evolution equations for the director (4.14) and inelastic deformation (4.26) are implemented using the weak form; the COMSOL file is provided. Linear Lagrange interpolation is used for the displacement field $\boldsymbol{u}$ $(= \boldsymbol{x} - \boldsymbol{X})$ and the director θ, while discontinuous linear Lagrange interpolation is chosen for the inelastic deformation $\mathbf{F}_i^v$ and the out-of-plane stretch λ_{33}. The convergence of stress-stretch response and deformation is achieved through mesh refinement. The influence of the mesh size on the director field is discussed in the next section.

Figure 4.5c compares numerical and experimental stress-stretch responses for different loading rates. Figure 4.5d shows snapshots of the deformation of the film from both experiments and simulations under different applied stretches and loading rates, along with the director distribution $\cos\theta$ from the numerical simulations. Blue lines from the experimental samples and black lines from the simulations, in the *X* and *Y* directions in the reference states, are drawn for comparison. The overall deformation predictions agree well with the experimental results. As the stretch increases, the circular hole becomes more elliptical, and the horizontal lines near the hole rotate due to the shear deformation caused by director rotation (Figure 4.5d & e). The shape of the hole is plotted under different stretches and loading rates, showing that the hole shapes almost overlap for the two different loading rates (Figure 4.5e). At high stretches, the shear deformation near the clamped boundary in the experiments is more significant than that in the simulations, possibly due to sample sliding from the gripper; see the blue line at the top left corner of the sample at $\lambda = 2$. When $\lambda = 2$, the horizontal lines near the hole rotate more at a lower stretching rate, indicating higher shear deformation, and the director distribution near the two sides of the hole is more homogeneous. The hole at the higher loading rate is slightly shorter since it takes time for materials to relax (Figure 4.5e). Our model demonstrates robust predictive capabilities for the mechanical responses of LCEs.

Table 4.4 Viscosity parameters for uniaxial tension with inhomogeneous deformation

$\tau_i(s)$	0.1	0.5	3.5	31.5	346.5
μ_i/μ_0	14.115440	2.565638	0.934889	0.581484	0.338014

Table 4.5 Remaining material parameters for uniaxial tension with homogeneous deformation

μ_0(MPa)	r	a_0	a_p	m	K/μ_0	K_i/μ_i	$\eta_{0,0}$(MPa · s)	μ_α
0.5932	5	0.09	0.0	0.2	1000	1000	1	1/4

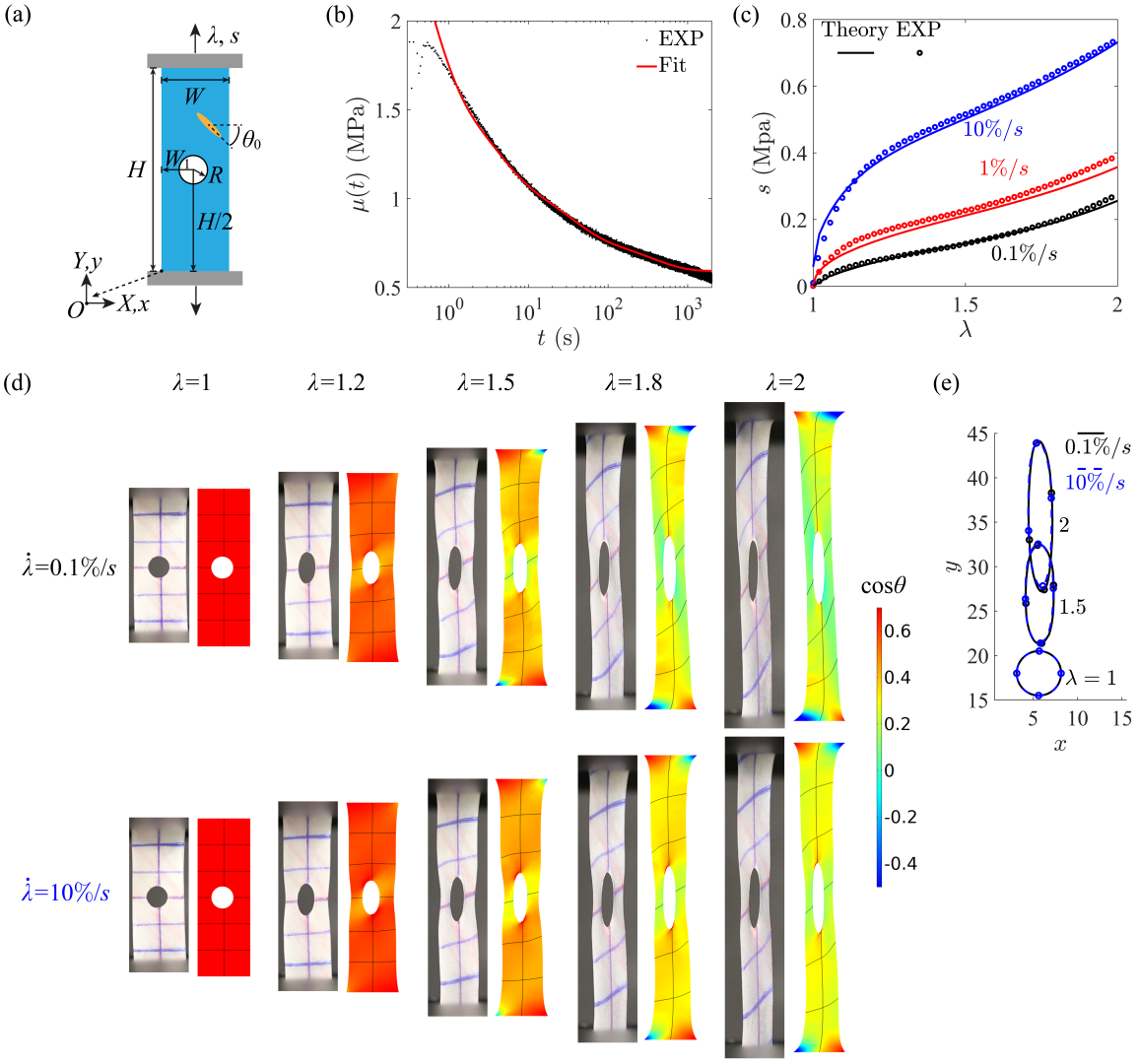

Figure 4.5 (a) Schematic of a LCE film with an off-center hole subjected to uniaxial tension. (b) Experimental and fitted relaxation shear modulus as a function of time. (c) Numerical and experimental stress-stretch responses for different loading rates. (d) Experimental and numerical

results of the deformation under various stretches and loading rates. The color bar represents the director field $cos\,\theta$. (e) Numerical results of the shape of the hole under various stretches and loading rates, with four circles marked on the hole for visualization.

4.5.2 Influence of mesh sizes

It is known that the neoclassical and semisoft free energy densities are nonconvex (Warner, Desimone), which can lead to multiple equilibrium solutions due to director rotation. Consequently, the numerical results may be sensitive to mesh discretization. We examine the director field near the hole using various mesh densities. A typically generated mesh is shown in Figure 4.6a. A polar coordinate system (ρ, θ_ρ) is defined in the reference configuration, with the origin at the center of the hole. The region $(R \leq \rho \leq 1.2R)$ near the hole contains structured meshes, with the maximum mesh size denoted as H_e.

Figure 4.6b shows the director distributions of the sample with two different mesh sizes under an applied stretch of $\lambda = 2$ and at a loading rate $0.1\%/s$. No significant differences are observed except in the top and bottom regions near the hole (Figure 4.6b & c). When the mesh size is small ($H_e = 0.02$), two clear domain walls are seen in these regions, with the director on the opposite sides of the wall rotating in opposite directions (Figure 4.6c & d). The domain walls are very close to the edge of the hole, and their influence on the director distribution decays rapidly along the radial direction (Figure 4.6c & d). Contrary to the existing literature, we observe that mesh refinement doesn't necessarily lead to a converged director distribution. The local director distribution near the domain walls is indeed sensitive to mesh densities. Proper mesh needs to be generated to balance result convergence and computation cost to capture the microstructure.

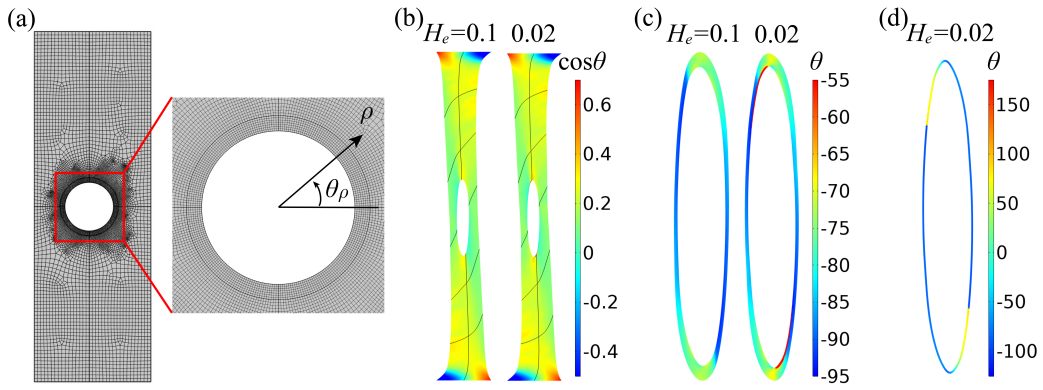

Figure 4.6 (a) A generated mesh and polar coordinates defined in the reference configuration. Director distribution (b) of the sample and (c) near the hole ($R \leq \rho \leq 1.2R$) for two different mesh sizes ($H_e = 0.1$ & 0.02). (d) Director distribution along the edge of the hole ($\rho = R$).

The influence of mesh sizes is further detailed in Figure 4.7. The director angle θ is plotted as a function of the angular coordinate θ_ρ along the edge of the hole for different mesh sizes (Figure 4.7a-e). Figure 4.7a & b show the director distribution along the hole ($\rho = R$) at applied stretches of $\lambda = 1.1$ and $\lambda = 2$ under a slow loading rate of 0.1%/s, respectively. Figure 4.7c provides a zoomed-in view of Figure 4.7b. When the applied stretch is small ($\lambda = 1.1$), the domain wall doesn't form. When the applied stretch is large ($\lambda = 2$), formation of domain walls is observed for small enough mesh sizes. However, the locations of the domain walls slightly shift with the changes in the mesh size. The director does not converge over a large range of θ_ρ, particularly within $-135° \leq \theta_\rho \leq 45°$ and $45° \leq \theta_\rho \leq 135°$, while converges in the remaining regions (Figure 4.7a-c). The influence of the domain wall decays quickly in the radial direction, and the director distribution along the circle $\rho = 1.2R$ shows overall convergence with respect to different mesh sizes (Figure 4.7d). At a high loading rate, formation of domain walls is observed

for a larger mesh size (Figure 4.7e). Figure 4.7f & g show that the simulated shape of the hole for different mesh sizes overlaps at loading rates of $0.1\%/s$ and $10\%/s$, respectively. One possible way to obtain a converged director field is to introduce the Frank energy into the free energy. The introduction of the Frank energy provides a certain length scale, allowing the director to change smoothly across the domain wall. When the mesh size is much smaller than this length scale, the director field could converge with respect to different mesh sizes.

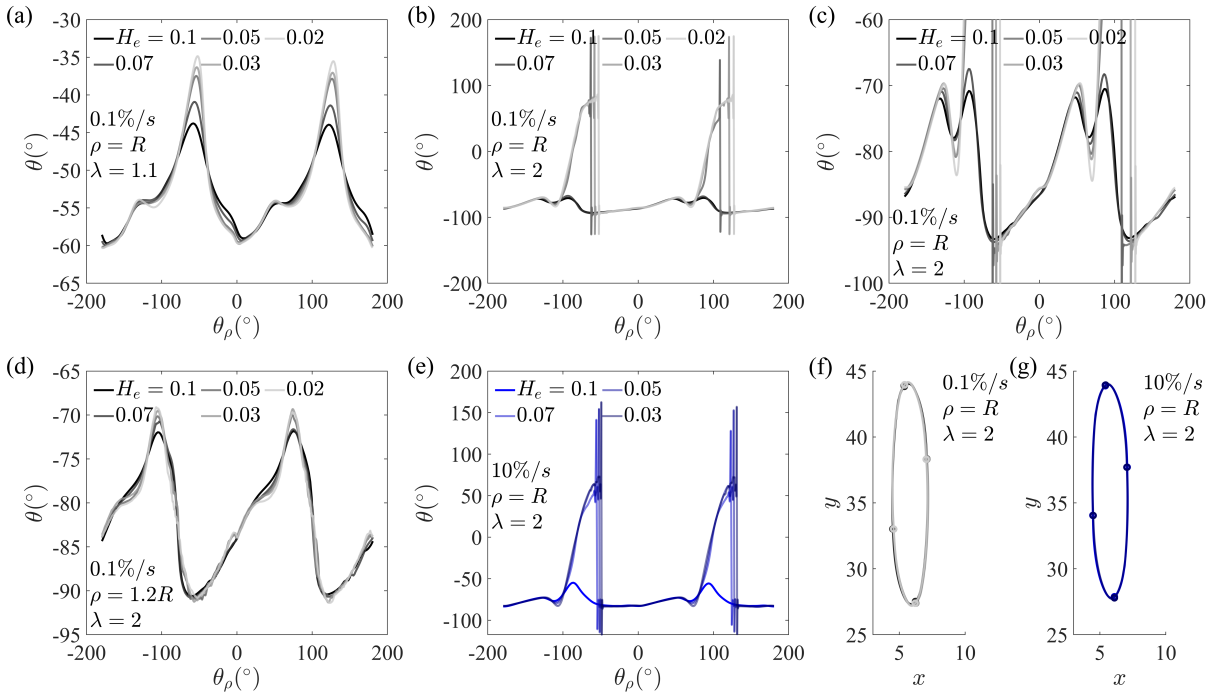

Figure 4.7 Influence of mesh sizes on the director distribution along the hole ($\rho = R$) under an applied stretch of (a) $\lambda = 1.1$ and (b) $\lambda = 2$ at a slow loading rate of $0.1\%/s$. (c) The zoomed-in plot of (b) showing detailed director distributions. Influence of mesh sizes on the director distribution along the circle ($\rho = 1.2R$) under $\lambda = 2$ (d) at the same low loading rate of $0.1\%/s$,

and (e) at a high loading rate of $10\%/s$. Simulated shape of the hole for different mesh sizes under $\lambda = 2$ at loading rates of (f) $0.1\%/s$ and (g) $10\%/s$.

4.6 Conclusion

We have developed a modified semisoft model capable of predicting both elastic and viscoelastic behaviors for LCEs. The classical semisoft elastic energy term was revised by treating the original semisoft parameter a as a function of deformation. We postulate that the non-constant nature of a arises from the varying shape anisotropy r with both deformation and deformation rate, because the order parameter varies. With our modification, the model accurately predicts the stress-stretch curves of LCEs, successfully capturing the stress plateau. We extend the modified free energy to a viscoelastic model and implement it in COMSOL. The model shows overall good predictions of the viscoelastic response.

The modified model and numerical implementation can be further improved in a few aspects. To enhance the agreement between the experiments and theoretical predictions of rate-dependent deformation and director orientation, we can model a as a function of r in accordance with the compositional fluctuation model and consider the evolution of r. Moreover, LCEs can generate large shear deformation under stretching, causing undesired boundary deformation in practical setups. Ensuring proper boundary conditions in both theoretical frameworks and experiments is essential for more accurate predictions. Given the nonconvexity of the free energy, the computational cost might be high to obtain converged results. The additional evolution equation of the inelastic deformation further increases the computational burden.

Chapter 5 Fracture of Liquid Crystal Elastomers

While the mechanical responses of LCEs have been extensively studied, their fracture behavior remains largely unexplored. Specifically, the effect of the deformation-director coupling on LCE fracture paths is unknown, and fracture criteria for LCEs are not yet established. To address this gap, we combine experimental and theoretical approaches to investigate fracture propagation in LCEs. We stretch edge-cracked monodomain LCE samples, recording their stress-strain responses and crack paths under varying initial directors and stretching rates. Our findings reveal that crack propagation paths are highly dependent on both the initial director and the stretching rate. To further understand LCE fracture behavior, we develop a rate-dependent phase-field fracture model, which is validated through experiments and demonstrates the ability to predict complex fracture paths. Our study paves the way for designing LCEs with enhanced fracture properties, beneficial for future applications.

5.1 Introduction

Although the mechanical properties of LCEs have been extensively studied, their fracture behavior remains relatively unknown, possibly due to the complex director rotation of LCEs [144]. The influence of stretching rates further increases the complexity. The effects of the director, stretching rates, and geometry on LCE fracture behavior remain unresolved. For example, the relationship between the liquid crystal alignment and fracture behavior is not fully understood due to insufficient experimental characterizations. Additionally, the absence of established fracture criteria for LCEs makes predicting their fracture behavior under various stretching conditions challenging. Moreover, there is a lack of simulation tools for studying the fracture process of LCEs.

To address these issues, we combine experiments and theoretical approaches to systematically study fracture of monodomain LCEs. We stretch edge-cracked monodomain LCE samples, record their stress-strain relations and crack paths with varying initial directors and stretching rates. We establish fracture criteria that the crack prefers to propagate perpendicular to the director in LCEs and develop a rate-dependent phase-field fracture model to predict crack propagation. Our model is validated through experiments with different geometries and stretching rates, showing its capability to predict complex fracture paths in LCEs.

5.2 Tilted Fracture Path

We conducted fracture tests on LCE samples with a length of $H = 30mm$ and a width of $W = 5mm$ (Figure 5.1a). A sample with a tilted initial director $\theta_0 = 45°$ and a horizontal edged crack of length $l_c = 0.4W$ was subjected to axial tension at two different stretching rates, $\dot{\lambda} = 0.1\%/s$ and $\dot{\lambda} = 10\%/s$. Figure 5.1b shows the stress-stretch curves for both stretching rates, where the red curve corresponds to $0.1\%/s$ and the reddish-grey curve to $10\%/s$. Specific points $(i - v)$ along the lower stretching rate curve $(0.1\%/s)$ mark different stages of deformation and crack propagation, as shown in Figure 5.1c. The nominal stress increases with the applied stretch. At a certain applied stretch, the sample begins to fracture, and then the nominal stress reaches its maximum with increasing stretch, followed by a decrease to zero when the sample is completely broken. In the test, two blue horizontal lines serve as visual references. As the stretch increases, the pre-crack opens asymmetrically, and the blue lines rotate, indicating substantial shear deformation. As images iv and v show, the crack propagates almost horizontally in the deformed configuration. After full relaxation, the fracture path is tilted (Figure 5.1d). We define the fracture

angle θ_c through the average slope of the crack region between $X = 3/5W$ and $X = W$. The final crack orientations differ for the two stretching rates, which whose values are different from the initial director. These observations suggest that stretching rate significantly influences crack propagation path and the overall fracture behavior of the LCE samples.

The observed fracture behavior is quite different from the conventional fiber-reinforced hyperelastic materials, where the fracture path is usually parallel to the fiber direction in the reference configuration [152]. The fracture path in the deformed configuration should be tilted. The deformed fiber orientation is directly calculated by the multiplying of the deformation gradient and the initial fiber orientation. In contrast, the director in LCEs is an additional state variable, whose orientation is determined by an additional governing equation. Since the fracture orientation of LCEs is different from the initial director, it is reasonable to think that the fracture path is related to the current director in the deformed configuration. In addition, the director rotates to the stretched direction. According to our previous uniaxial tension study of LCE samples with homogeneous deformation, when the applied stretch is around 2.5, the director is expected to be almost vertical. From the observation of the horizontal fracture propagation and expected vertical director distribution, we hypothesize that the crack prefers to propagate perpendicular to the director. A recent study of the fracture of blood clots made up of platelets and fibrin has shown that cracks propagate perpendicular to the stretched fiber direction [153, 154], which aligns with our assumption.

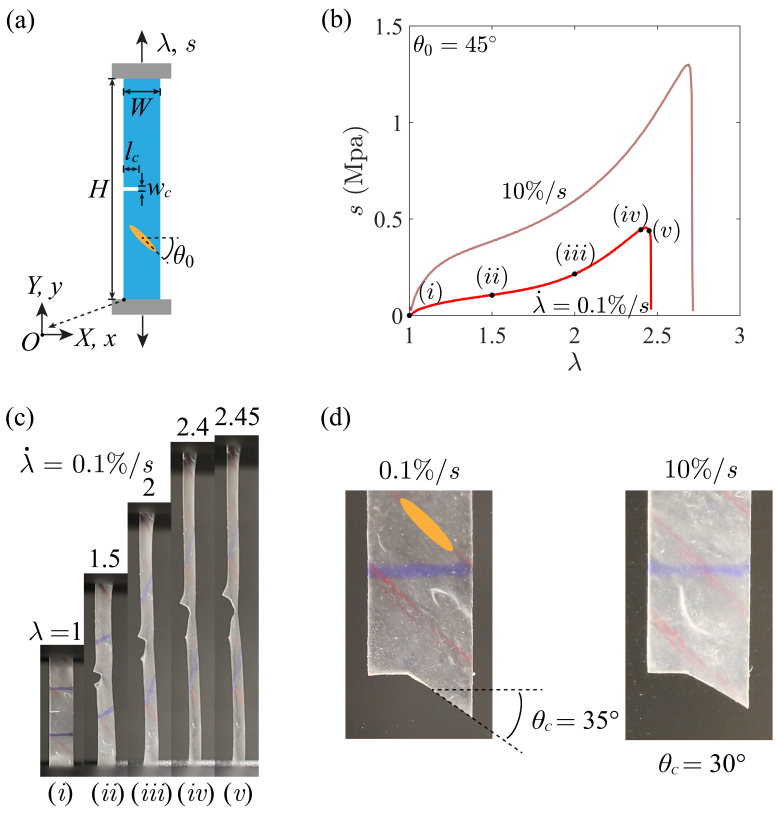

Figure 5.1 (a) Schematic of an LCE sample with a tilted initial director and a horizontal edged crack subjected to uniaxial tension. The initial director is illustrated by the orange ellipse. (b) Stress-stretch responses for two different stretching rates, $\dot{\lambda} = 0.1\%/s$ and $\dot{\lambda} = 10\%/s$. (c) Images showing deformation and crack propagation at different stretches. (d) Relaxed samples with a tilted fracture path under two stretching rates.

5.3 Phase-field Fracture

To quantitatively understand the observed rate-dependent fracture phenomena and predict other possible fracture behaviors, we developed a phase-field fracture model (Appendix A3.3). We constructed a thermodynamically consistent phase-field fracture framework to simulate the fracture process of viscoelastic LCEs. The phase field $d \in [0,1]$ is introduced to describe the

damage degree of the material. With the assumption that the crack prefers to propagate perpendicular to the director, the evolution of the crack phase field d can be formulated. The developed model is implemented in the commercial software COMSOL.

We numerically studied the sample with the same geometry, initial director and boundary conditions as the experiments. Figure 5.2a shows the numerical and experimental comparison of stress-stretch responses for two stretching rates, where the solid lines are obtained from the simulation. The stress-stretch response and the stretch for the onset of fracture obtained from the simulation agree well with the experiments. The snapshots for the numerical deformation and crack propagation of the LCE sample under $\dot{\lambda} = 0.1\%/s$ with the contours of phase field d are shown (Figure 5.2b). The black lines are shown for visual reference. Significant shear deformation is shown with the rotation of the black lines. The deformation and horizontal crack propagation are similar to the experimental observations. The final fracture paths with two stretching rates are shown in Figure 5.2c, where two different fracture angles are obtained, consistent with the experimental findings. It's noted that the numerical prediction under a higher stretching rate underestimates the crack angle quite significantly. The tilted fracture path can be explained by the intriguing deformation and director rotation of LCEs (Figure 5.2b & d). Figure 5.2d shows the x component of the director $\cos\theta$ near the crack tip, where θ is the angle between the director and x axis. Near the crack tip, we can clearly see that $\cos\theta$ is close to 0 in front of the crack tip, which means the director is almost vertical. The vertical director leads to horizontal fracture propagation, based on our assumption that the crack prefers to propagate perpendicular to the director (Figure 5.2b). After the sample fully relaxes, the horizontal fracture path in the deformed configuration

becomes tilted in the reference configuration. The combined shear deformation and the director lead to the tilted fracture path.

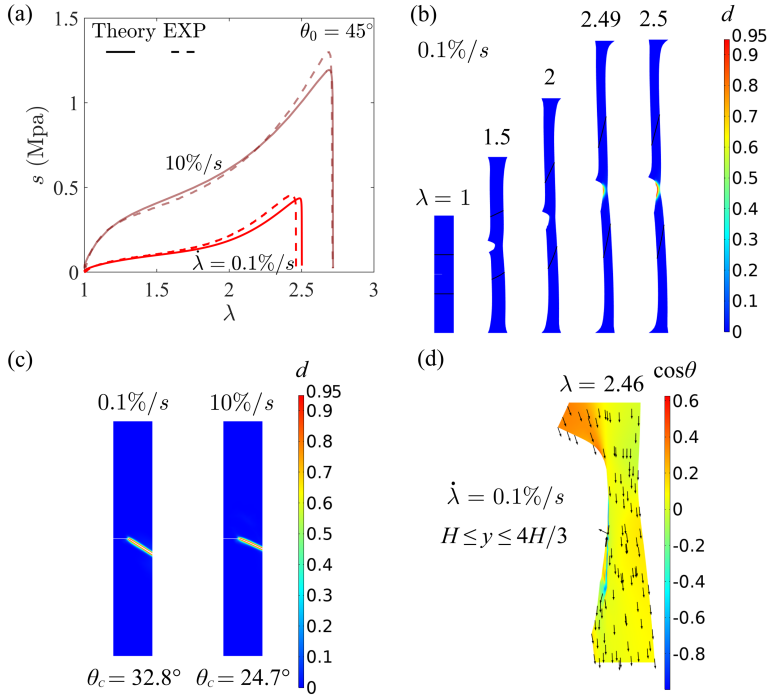

Figure 5.2 (a) Numerical and experimental comparison of stress-stretch responses for different stretching rates. (b) Numerical predictions of the deformation and crack propagation with a stretching rate of $0.1\%/s$. The color bar represents the phase field, and the material with $d > 0.95$ has been removed. (c) Fractured samples with two stretching rates in the reference configuration. (d) Director distribution in front of the crack tip, where the color bar represents the x component of the director $\cos\theta$.

5.4 Influence of Stretching Rates and Initial Directors

We further conducted simulations and experiments to investigate the influence of stretching rates and initial directors. Our model predicts the stress-stretch response and the stretch

for LCEs to fracture completely reasonably well (Figure 5.3a). Nonetheless, some discrepancies are evident. When $\theta_0 = 30°$, the predicted stress is higher than that from the experiments, and the predicted fracture stretch is smaller than the experiments. Conversely, when $\theta_0 = 75°$, the predicted stress is lower than that from the experiments, and the predicted fracture stretch is larger than the experiments. It is also notable that the critical stretch for fracture increases when the stretching rate increases from $0.1\%/s$ to $1\%/s$, and there is no definite trend for the critical stretch when the stretching rate increases from $1\%/s$ to $10\%/s$. More experimental data are provided in Appendix A3.2 (Figure A3.1 & A3.2). In addition, the maximum stress increases with the increases of the initial director. Higher stress but lower stretch is required to break the LCE sample with a higher initial director θ_0. It is noted that for $\theta_0 = 75°$, a quite amount of stretch is needed from the point of maximum applied stress to complete fracture, making the fracture more quasi-brittle.

Figure 5.3b shows the crack angle θ_c from experiments and numerical simulations. From the simulation, the crack angle decreases with the increase of the stretching rate. A similar trend is observed from the experiments, particularly for a smaller initial director ($\theta_0 = 30° \,\&\, 45°$). Combing with our previous viscoelastic study that a higher stretching rate leads to smaller shear deformation, a higher stretching rate should result in a smaller crack angle. The simulation greatly underestimates the crack angle when the stretching rate is high, which can be explained by the significant underestimation of shear stretch under the high stretching rate by our model. Both simulations and experiments show that the crack angle θ_c changes nonmonotonically with the angle of the initial director θ_0, where the crack angle θ_c first increases and then decreases with the increase of θ_0. Despite these differences, our model predicts overall trends consistent with the experimental results. The typical fracture paths from the experiments and simulations under the

stretching rate $1\%/s$ are shown in Figure A3.3. The fracture path with higher θ_0 is more curved, correlating to the quasi-brittle fracture behavior.

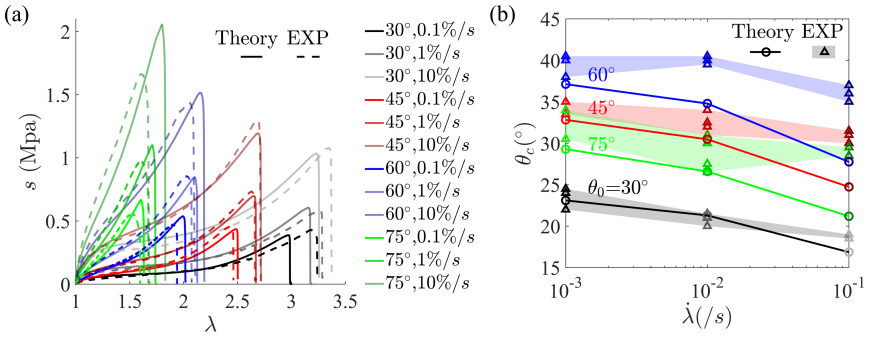

Figure 5.3 (a) Numerical and experimental stress-stretch responses for various initial directors and stretching rates. (b) Fracture angles obtained from experiments and simulations.

5.5 Influence of Geometry

We further explore the influence of geometry using LCE samples with a length of $H = 10mm$ and a width of $W = 15mm$. The initial director is $\theta_0 = 45°$, and the pre-crack length is $l_c = 0.4W$. Figure 5.4a & d show the experimental and numerical results of the deformation and crack propagation under two stretching rates, $\dot{\lambda} = 0.1\%/s$ and $\dot{\lambda} = 10\%/s$. The blue and black lines are for visual reference. At the beginning of the crack propagation, the blue line remains almost horizontal in front of the crack tip, and the crack propagates upward. It is worth mentioning that the lines are slightly titled before the crack propagation (Figure A3.4). The crack tip under the lower stretching rate is more rounded due to the material relaxation. After the fractured sample fully relaxes, the final fracture path exhibits an initial upward trajectory followed by a downward trend (Figure 5.4b). The fracture paths abstracted from experiments and simulations agree relatively well (Figure 5.4c). The initial slope under the higher stretching rate is smaller. Figure

5.4e shows the director distribution in the early stage of the crack propagation, where the director in front of the crack tip is tilted, leading to the upward fracture path in the deformed configuration. Combining the horizontal black line, indicating little shear component λ_{12}, the initial fracture path in the undeformed configuration is expected to exhibit an initial upward trajectory, where the initial slope is highly correlated with the director distribution and deformation state. The subsequent downward trend can be explained similarly to the previous sample with a large length-to-width ratio.

Figure 5.4f shows the numerical and experimental comparison of stress-stretch responses for different stretching rates. The stress response at a lower stretching rate agrees with each other very well. The theoretical results overestimate the critical stretch and maximum stress compared to the experiments at higher stretching rates. In addition, more stretch is required to completely break the sample. These discrepancies indicate a need for a better viscoelastic constitutive model and fracture criterion. Nonetheless, our model shows good overall predictions of the deformation, stress-stretch response, and fracture path.

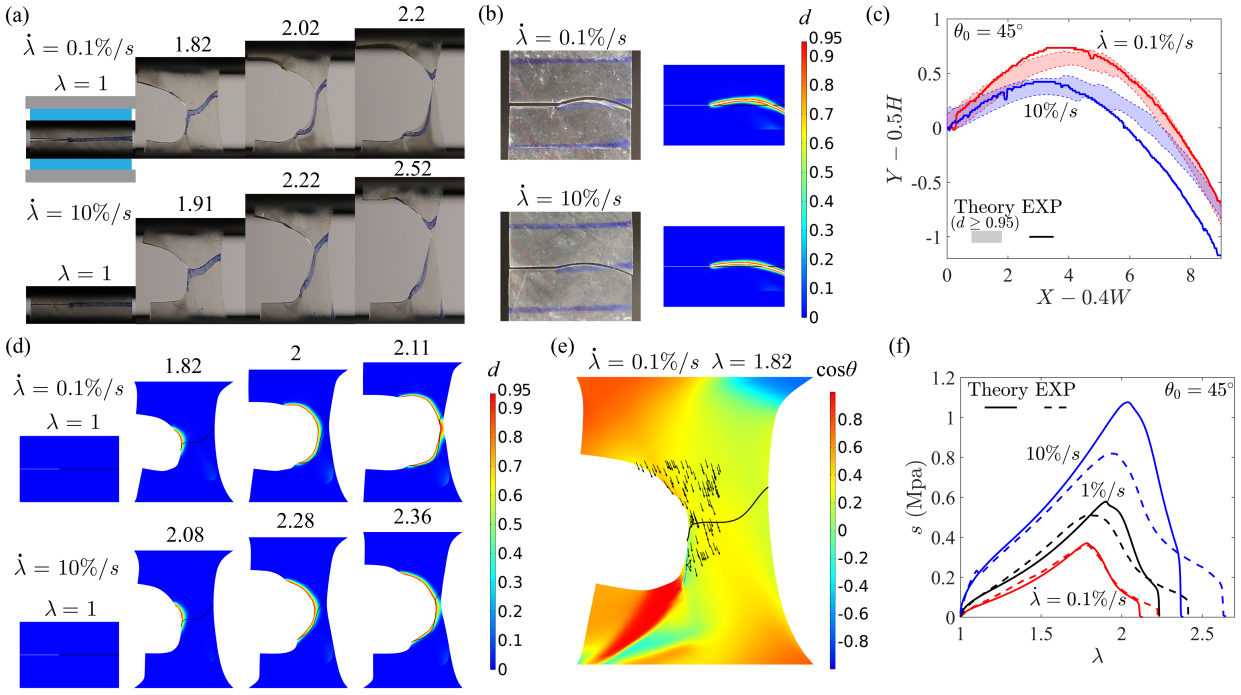

Figure 5.4 (a) Images of deformation and crack propagation at different stretches under two stretching rates, $\dot{\lambda} = 0.1\%/s$ and $\dot{\lambda} = 10\%/s$. The sample near the boundary is obscured by the gripper, as illustrated in the schematic ($\lambda = 1$). (b) Experimental and numerical fractured samples with two stretching rates in the reference configuration. (c) Corresponding fracture paths from experiments and simulations. (d) Numerical predictions of deformation and crack propagation. (e) Corresponding director distribution. (f) Numerical and experimental comparison of stress-stretch responses for different stretching rates.

5.6 Influence of Pre-cracks

We further explore the influence of pre-cracks on the fracture path using two examples, including changing the pre-crack length and introducing two pre-cracks. The height of all samples is 10mm. An initial director orientation of $\theta_0 = 45°$ and a stretching rate of $\dot{\lambda} = 1\%/s$ are used

for both tests. For the single edged crack, the width is $W = 15mm$ and the pre-crack length is $l_c = 0.6W$ (Figure 5.5a). Figure 5.5a shows the experiments and simulations of deformation, crack propagation and final fracture path. The fracture initially propagates upward, and the black and blue lines are tilted upward in the deformed configuration. Compared to the short pre-crack, the slope of the initial upward trajectory is smaller in the reference configuration. The combined deformation and director distribution lead to the fracture path (Figure 5.5b). With further increase of the pre-crack length, an initial downward trajectory should be expected.

Two pre-cracks are introduced to observe the interaction of the cracks, with a width of $W = 20mm$ and a pre-crack length of $l_c = 0.25W$ (Figure 5.5c). The experimental and numerical deformation and fracture propagation are shown in Figure 5.5d & e. Both the blue lines and black lines are tilted downward when the stretch is small. The left pre-crack propagates upward, and the right pre-crack propagates downward, with the blue lines and black lines tilting upward. When the two cracks propagate to the centerline, the blue lines and black lines become almost vertical. In the experiment, the two crack tips do not meet, and the final fracture occurs at one crack tip. In contrast, in the simulation, due to the large damage bands of the model, the two cracks change the crack tip location to the center, and the fracture finally occurs at the center of the sample. Figure 5.5f shows the corresponding experimental and numerical fracture paths in the reference configuration, where the simulation shows a sharp turn of the crack path, indicating the location change of the crack tip. Overall, the simulation can capture the experimental observations.

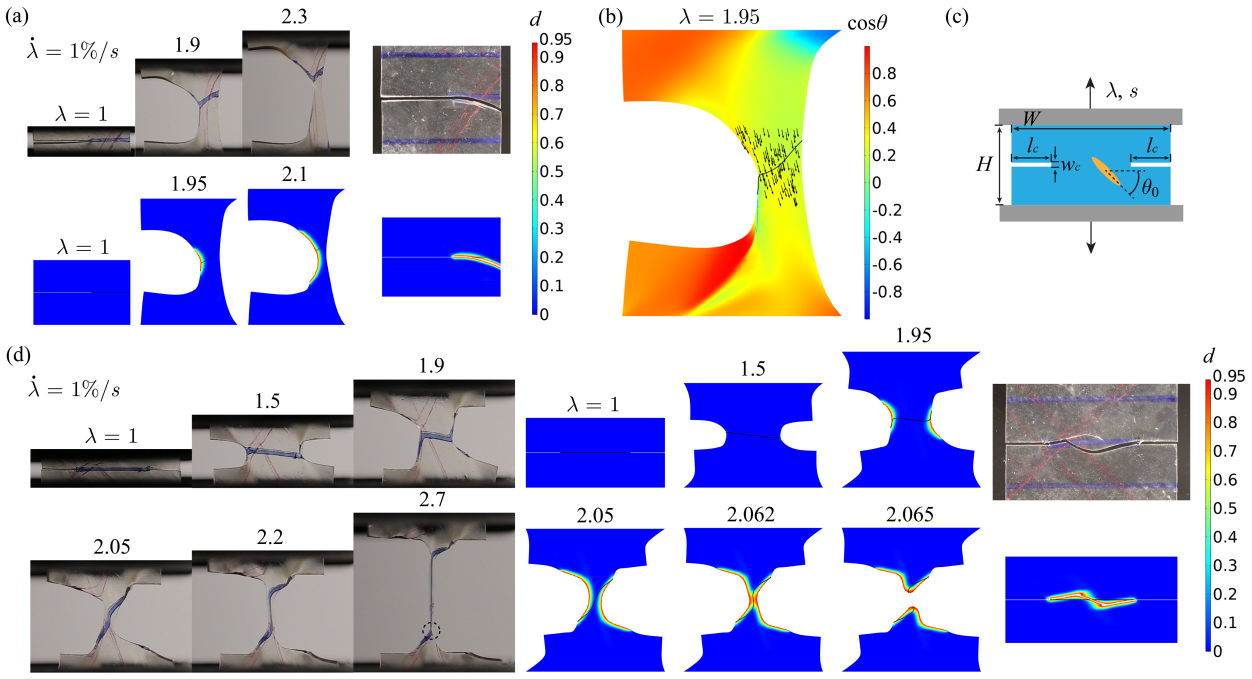

Figure 5.5 (a) Experiments and simulations of deformation, crack propagation and final fracture path. The pre-crack length is $l_c = 0.6W$. (b) Director distribution. (c) Schematic of an LCE sample with two horizontal edged cracks subjected to uniaxial tension. (d) Experimental snapshots and (e) numerical snapshots of deformation and crack propagation at different stretches. (f) Comparison of experimental and numerical fractured samples in the reference configuration.

5.7 Conclusion

The fracture behavior of LCEs has been rarely studied. To address this gap, we combine experiments and theory to investigate fracture propagation in LCEs. We study the influence of stretching rates, initial directors, and geometry on the fracture of LCEs, revealing that LCEs exhibit unusual fracture behavior depending on these factors. We propose that cracks prefer to propagate perpendicular to the director. Our developed phase-field fracture model predicts the crack propagation in LCEs with different initial directors and under varying stretching rates. Our theory

is validated by experiments and demonstrates the capability to predict complex fracture paths in LCEs. We uncover that the crack path is highly correlated with the director distribution and deformation state.

Although our models show overall great predictability, there are many open questions to be answered to better understand the fracture of LCEs. For instance, how can the fracture energy of the LCEs be experimentally measured? What is the influence of the director distribution and stretching rates on fracture energy. The assumption that cracks prefer to propagate perpendicular to the director needs further experimental validation. What is the range of deformation rates that this assumption validates? The assumption should be invalid at extremely high stretching rates, where the director doesn't have time to rotate. Both the viscoelastic and fracture models need further improvement. Accurate predictions of stress, deformation and director rotation under different stretching rates are still lacking. The current fracture model doesn't capture the crack propagation speed well, especially under high stretching rates. Nonetheless, we have obtained promising results. We hope this work paves the way for further studies of LCE fracture and the design of LCEs with superior fracture properties.

Chapter 6 Conclusion and Outlook

6.1 Conclusion

This dissertation has investigated the mechanical instability, phase separation, and fracture in soft materials under extreme loading conditions. The theoretical models, experimental results, and numerical simulations developed in this research have practical applications in designing and developing new materials and structures with extreme mechanical properties. The main contributions are summarized as follows:

In Chapter 2, we use elastic tubes as model systems to investigate postbuckling behaviors that have been elusive so far. We employ a combination of theoretical and numerical methods to study the morphologies, displacement fields, and stress-strain curves near the critical loading of tubes undergoing axial compression. By providing a theoretical solution to the postbuckling problem, this work sheds light on the buckling and postbuckling behavior of thick tubes, laying the foundation for the design of tube structures. Moreover, the developed general method is applicable to other structures exhibiting diverse mechanical instability, thereby contributing to the advancement of related fields.

In Chapter 3, we focus on how mechanical constraints can induce the coexistence of multiple phases in hydrogels that do not exhibit phase separation under equilibrium free swelling. Through a systematic analysis of the states of equilibrium for hydrogels under different mechanical loadings, we reveal the role played by mechanical constraints in altering the convexity of the free energy, thereby resulting in phase coexistence. Moreover, we apply a phase-field model to investigate the pattern evolution of phase separation and predict various patterns and processes of

phase separation under different geometric and material parameters. Our findings provide valuable insights into the rich phase behavior of hydrogels under diverse mechanical constraints and loading conditions, offering critical insights for experimental studies related to the morphological patterns of hydrogels.

In Chapter 4, we develop a modified semisoft model capable of predicting both elastic and viscoelastic behaviors for LCEs. The classical semisoft elastic energy term was revised by treating the original semisoft parameter a as a function of deformation. With our modification, the model accurately predicts the stress-stretch curves of LCEs, successfully capturing the stress plateau. We extend the modified free energy to a viscoelastic model and implement it in COMSOL. The model shows overall good predictions of the viscoelastic response. Our numerical models are provided to study general LCE constitutive behavior.

In Chapter 5, we combine experiments and theory to investigate fracture propagation in LCEs. We study the influence of stretching rates, initial directors, and geometry on the fracture of LCEs, revealing that LCEs exhibit unusual fracture behavior depending on these factors. We propose that cracks prefer to propagate perpendicular to the director. Our developed phase-field fracture model predicts the crack propagation in LCEs with different initial directors and under varying stretching rates. Our theory is validated by experiments and demonstrates the capability to predict complex fracture paths in LCEs. We uncover that the crack path is highly correlated with the director distribution and deformation state. Our study fills the gap of little research on LCE fracture.

6.2 Outlook

There are still many great opportunities to study mechanics of soft materials. Several interesting problems need to be solved in the near future. What is the influence of material laws on structure instability? Can we obtain stable domains with a finite size after phase separation? Can anisotropic phase separation lead to fast macroscopic deformation? What is the fracture criterion for viscoelastic materials? Is the intrinsic fracture energy a constant for a viscoelastic material? How do we measure the fracture energy of monodomain LCEs? How do we model the fracture propagation of stiffening materials?

Firstly, material laws definitely play a role on structure instability. We usually use simple elastic or hyperelastic constitutive model to study the mechanical instability. Some interesting phenomena could occur, such as delayed instability if we use poroelastic or viscoelastic constitutive model, since the material response involves certain time scales. The time evolving response could provide more functionality for the structure. In addition, a new constitutive model adds complexity to theoretical analysis. We can contribute to developing a more general asymptotic model to describe the time evolving response.

Secondly, in our study, the domain always prefers to coarsen when phase separation occurs. However, very recently, researchers experimentally observed elastic arrested phase separation, where the domain size doesn't change over time [155]. The exact mechanism is not clear, and our current model cannot explain the phenomenon either. Possible solutions include introducing nonlocal damage and active force as a function of solvent concentration. We hope we can figure out the mechanism and contribute to the community.

Thirdly, can we increase the response speed of hydrogels through phase separation? There is an intriguing experiment on fast actuation of hydrogels by Takuzo Aida [123]. The authors prepare a composite PNIPA gel with cofacially aligned nanosheets aligned nanosheets. The gel sheet with a thickness of 1 mm shows fast deformation in the order of seconds, which is significantly faster than the typical swelling or shrinking process of hydrogels that usually takes hours. The authors attribute the deformation to the electrostatic force change between the nanosheets. We hypothesize that the fast response is due to the anisotropic phase separation, where the length scale of the initial phase separation doesn't depend on the sample size. If this hypothesis validates, we can design hydrogels with anisotropic phase separation to avoid the drawback of the slow response of hydrogels, which can dramatically broaden the application of hydrogels on actuation.

Last but not least, monodomain LCEs are typically viscoelastic and anisotropic materials, which also show stress stiffening. When studying LCE fracture, it is found there are many questions about fracture of materials with properties different from conventional elastic materials. For LCEs, the director is always evolving with the loading, which makes it difficult to define the fracture energy of LCEs with a certain director. We need to provide a standard or protocol to measure the fracture energy. In addition, we would also like to further work on fracture of viscoelastic and stiffening materials, focusing on developing the fracture criterion and numerical tools.

Appendix 1 Supplementary Materials for Three-dimensional Postbuckling Analysis of Thick Hyperelastic Tubes

A1.1 Expressions of X_i $(i = 1,2,\ldots,7)$

In this appendix, we list the expressions of X_i $\left(i=1,2,\cdots,7\right)$. In the below analysis, the constant a_1 is set as 1. To simplify our expression, we use the following expression

$$\begin{aligned}\mathbf{L}&=\begin{bmatrix} U_{1R,R} & \dfrac{U_{1R,\Theta}-U_{1\Theta}}{R} & U_{1R,Z} \\ U_{1\Theta,R} & \dfrac{U_{1R}+U_{1\Theta,\Theta}}{R} & U_{1\Theta,Z} \\ U_{1Z,R} & \dfrac{U_{1Z,\Theta}}{R} & U_{1Z,Z} \end{bmatrix}=\begin{bmatrix} L_{11}^{(1)} & L_{12}^{(1)} & L_{13}^{(1)} \\ L_{21}^{(1)} & L_{22}^{(1)} & L_{23}^{(1)} \\ L_{31}^{(1)} & L_{32}^{(1)} & L_{33}^{(1)} \end{bmatrix} \\ &=\begin{bmatrix} \bar{L}_{11}^{(1)}\cos n\Theta\cos\eta Z & \bar{L}_{12}^{(1)}\sin n\Theta\cos\eta Z & \bar{L}_{13}^{(1)}\cos n\Theta\sin\eta Z \\ \bar{L}_{21}^{(1)}\sin n\Theta\cos\eta Z & \bar{L}_{22}^{(1)}\cos n\Theta\cos\eta Z & \bar{L}_{23}^{(1)}\sin n\Theta\sin\eta Z \\ \bar{L}_{31}^{(1)}\cos n\Theta\sin\eta Z & \bar{L}_{32}^{(1)}\sin n\Theta\sin\eta Z & \bar{L}_{33}^{(1)}\cos n\Theta\cos\eta Z \end{bmatrix}.\end{aligned} \tag{A1.1.1}$$

The expressions of X_i $\left(i=1,2,\cdots,7\right)$ in Eqs. (2.26)-(2.27) read

$$\begin{aligned}X_1=&\left[p_1\left(\frac{1}{R}\lambda_c L_{11}^{(1)}+\frac{1}{R}\frac{1}{\sqrt{\lambda_c}}L_{33}^{(1)}\right)+\frac{\mu}{\lambda_c}\left(\frac{1}{R}L_{11}^{(1)}L_{33}^{(1)}-\frac{1}{R}L_{31}^{(1)}L_{13}^{(1)}\right)\right] \\ &-\frac{1}{R}\left\{R\left[p_1\left(\lambda_c L_{22}^{(1)}+\frac{1}{\sqrt{\lambda_c}}L_{33}^{(1)}\right)+\frac{\mu}{\lambda_c}\left(L_{22}^{(1)}L_{33}^{(1)}-L_{32}^{(1)}L_{23}^{(1)}\right)\right]\right\}_{,R} \\ &-\left[p_1\left(-\lambda_c\frac{1}{R}L_{21}^{(1)}\right)+\frac{\mu}{\lambda_c}\left(\frac{1}{R}L_{31}^{(1)}L_{23}^{(1)}-\frac{1}{R}L_{33}^{(1)}L_{21}^{(1)}\right)\right]_{,\Theta} \\ &-\left[p_1\left(-\frac{1}{\sqrt{\lambda_c}}L_{31}^{(1)}\right)+\frac{\mu}{\lambda_c}\left(L_{21}^{(1)}L_{32}^{(1)}-L_{31}^{(1)}L_{22}^{(1)}\right)\right]_{,Z},\end{aligned} \tag{A1.1.2}$$

$$
\begin{aligned}
X_2 = &\left[p_1\left(\lambda_c \frac{1}{R} L_{21}^{(1)} \right) + \frac{\mu}{\lambda_c}\left(-\frac{1}{R} L_{31}^{(1)} L_{23}^{(1)} + \frac{1}{R} L_{33}^{(1)} L_{21}^{(1)} \right) \right] \\
&-\frac{1}{R}\left\{ R\left[p_1\left(-\lambda_c L_{12}^{(1)} \right) + \frac{\mu}{\lambda_c}\left(L_{32}^{(1)} L_{13}^{(1)} - L_{33}^{(1)} L_{12}^{(1)} \right) \right] \right\}_{,R} \\
&-\left[p_1\left(\frac{1}{R} \lambda_c L_{11}^{(1)} + \frac{1}{\sqrt{\lambda_c}} \frac{1}{R} L_{33}^{(1)} \right) + \frac{\mu}{\lambda_c}\left(\frac{1}{R} L_{11}^{(1)} L_{33}^{(1)} - \frac{1}{R} L_{31}^{(1)} L_{13}^{(1)} \right) \right]_{,\Theta} \\
&-\left[p_1\left(-\frac{1}{\sqrt{\lambda_c}} L_{32}^{(1)} \right) + \frac{\mu}{\lambda_c}\left(L_{31}^{(1)} L_{12}^{(1)} - L_{32}^{(1)} L_{11}^{(1)} \right) \right]_{,Z},
\end{aligned}
\tag{A1.1.3}
$$

$$
\begin{aligned}
X_3 = &\frac{1}{R}\left\{ R\left[p_1\left(-\frac{1}{\sqrt{\lambda_c}} L_{13}^{(1)} \right) + \frac{\mu}{\lambda_c}\left(L_{12}^{(1)} L_{23}^{(1)} - L_{22}^{(1)} L_{13}^{(1)} \right) \right] \right\}_{,R} \\
&+\left[p_1\left(-\frac{1}{R} \frac{1}{\sqrt{\lambda_c}} L_{23}^{(1)} \right) + \frac{\mu}{\lambda_c}\left(\frac{1}{R} L_{21}^{(1)} L_{13}^{(1)} - \frac{1}{R} L_{23}^{(1)} L_{11}^{(1)} \right) \right]_{,\Theta} \\
&+\left[p_1\left(\frac{1}{\sqrt{\lambda_c}} L_{11}^{(1)} + \frac{1}{\sqrt{\lambda_c}} L_{22}^{(1)} \right) + \frac{\mu}{\lambda_c}\left(L_{11}^{(1)} L_{22}^{(1)} - L_{21}^{(1)} L_{12}^{(1)} \right) \right]_{,Z},
\end{aligned}
\tag{A1.1.4}
$$

$$
X_4 = -\left(\lambda_c L_{11}^{(1)} L_{22}^{(1)} + \frac{1}{\sqrt{\lambda_c}} L_{11}^{(1)} L_{33}^{(1)} + \frac{1}{\sqrt{\lambda_c}} L_{22}^{(1)} L_{33}^{(1)} - \frac{1}{\sqrt{\lambda_c}} L_{31}^{(1)} L_{13}^{(1)} - \frac{1}{\sqrt{\lambda_c}} L_{32}^{(1)} L_{23}^{(1)} - \lambda_c L_{21}^{(1)} L_{12}^{(1)} \right), \tag{A1.1.5}
$$

$$
X_5 = p_1\left(\lambda_c L_{22}^{(1)} + \frac{1}{\sqrt{\lambda_c}} L_{33}^{(1)} \right) + \frac{\mu}{\lambda_c}\left(L_{22}^{(1)} L_{33}^{(1)} - L_{32}^{(1)} L_{23}^{(1)} \right), \tag{A1.1.6}
$$

$$
X_6 = p_1\left(-\lambda_c L_{12}^{(1)} \right) + \frac{\mu}{\lambda_c}\left(L_{32}^{(1)} L_{13}^{(1)} - L_{33}^{(1)} L_{12}^{(1)} \right), \tag{A1.1.7}
$$

$$
X_7 = p_1\left(-\frac{1}{\sqrt{\lambda_c}} L_{13}^{(1)} \right) + \frac{\mu}{\lambda_c}\left(L_{12}^{(1)} L_{23}^{(1)} - L_{22}^{(1)} L_{13}^{(1)} \right). \tag{A1.1.8}
$$

A1.2 Expressions of $X_i^{[3]}$ $(i = 1,2,\ldots,7)$

The expressions of $X_i^{[3]}$ $\left(i=1,2,\cdots,7\right)$ in Eqs. (2.31)-(2.32) read

$$
\begin{aligned}
X_1^{[3]} &= \frac{1}{4}\left[q_1\left(\frac{1}{R}\lambda_c \bar{L}_{11}^{(1)} + \frac{1}{R}\frac{1}{\sqrt{\lambda_c}}\bar{L}_{33}^{(1)} \right) + \frac{\mu}{\lambda_c}\left(\frac{1}{R}\bar{L}_{11}^{(1)}\bar{L}_{33}^{(1)} + \frac{1}{R}\bar{L}_{31}^{(1)}\bar{L}_{13}^{(1)} \right) \right] \\
&-\frac{1}{4}\frac{1}{R}\left\{ R\left[q_1\left(\lambda_c \bar{L}_{22}^{(1)} + \frac{1}{\sqrt{\lambda_c}}\bar{L}_{33}^{(1)} \right) + \frac{\mu}{\lambda_c}\left(\bar{L}_{22}^{(1)}\bar{L}_{33}^{(1)} - \bar{L}_{32}^{(1)}\bar{L}_{23}^{(1)} \right) \right] \right\}_{,R} \\
&-\frac{1}{2}n\left[q_1\left(-\lambda_c \frac{1}{R}\bar{L}_{21}^{(1)} \right) + \frac{\mu}{\lambda_c}\left(-\frac{1}{R}\bar{L}_{31}^{(1)}\bar{L}_{23}^{(1)} - \frac{1}{R}\bar{L}_{33}^{(1)}\bar{L}_{21}^{(1)} \right) \right] \\
&-\frac{1}{2}\eta\left[q_1\left(-\frac{1}{\sqrt{\lambda_c}}\bar{L}_{31}^{(1)} \right) + \frac{\mu}{\lambda_c}\left(-\bar{L}_{21}^{(1)}\bar{L}_{32}^{(1)} - \bar{L}_{31}^{(1)}\bar{L}_{22}^{(1)} \right) \right],
\end{aligned}
\tag{A1.2.1}
$$

$$
\begin{aligned}
X_2^{[3]} &= \frac{1}{4}\left[q_1\left(\lambda_c \frac{1}{R}\bar{L}_{21}^{(1)} \right) + \frac{\mu}{\lambda_c}\left(\frac{1}{R}\bar{L}_{31}^{(1)}\bar{L}_{23}^{(1)} + \frac{1}{R}\bar{L}_{33}^{(1)}\bar{L}_{21}^{(1)} \right) \right] \\
&-\frac{1}{4}\frac{1}{R}\left\{ R\left[q_1\left(-\lambda_c \bar{L}_{12}^{(1)} \right) + \frac{\mu}{\lambda_c}\left(-\bar{L}_{32}^{(1)}\bar{L}_{13}^{(1)} - \bar{L}_{33}^{(1)}\bar{L}_{12}^{(1)} \right) \right] \right\}_{,R} \\
&+\frac{1}{2}n\left[q_1\left(\frac{1}{R}\lambda_c \bar{L}_{11}^{(1)} + \frac{1}{\sqrt{\lambda_c}}\frac{1}{R}\bar{L}_{33}^{(1)} \right) + \frac{\mu}{\lambda_c}\left(\frac{1}{R}\bar{L}_{11}^{(1)}\bar{L}_{33}^{(1)} + \frac{1}{R}\bar{L}_{31}^{(1)}\bar{L}_{13}^{(1)} \right) \right] \\
&-\frac{1}{2}\eta\left[q_1\left(-\frac{1}{\sqrt{\lambda_c}}\bar{L}_{32}^{(1)} \right) + \frac{\mu}{\lambda_c}\left(\bar{L}_{31}^{(1)}\bar{L}_{12}^{(1)} - \bar{L}_{32}^{(1)}\bar{L}_{11}^{(1)} \right) \right],
\end{aligned}
\tag{A1.2.2}
$$

$$
\begin{aligned}
X_3^{[3]} &= \frac{1}{4}\frac{1}{R}\left\{ R\left[q_1\left(-\frac{1}{\sqrt{\lambda_c}}\bar{L}_{13}^{(1)} \right) + \frac{\mu}{\lambda_c}\left(-\bar{L}_{12}^{(1)}\bar{L}_{23}^{(1)} - \bar{L}_{22}^{(1)}\bar{L}_{13}^{(1)} \right) \right] \right\}_{,R} \\
&+\frac{1}{2}n\left[q_1\left(-\frac{1}{R}\frac{1}{\sqrt{\lambda_c}}\bar{L}_{23}^{(1)} \right) + \frac{\mu}{\lambda_c}\left(\frac{1}{R}\bar{L}_{21}^{(1)}\bar{L}_{13}^{(1)} - \frac{1}{R}\bar{L}_{23}^{(1)}\bar{L}_{11}^{(1)} \right) \right] \\
&-\frac{1}{2}\eta\left[q_1\left(\frac{1}{\sqrt{\lambda_c}}\bar{L}_{11}^{(1)} + \frac{1}{\sqrt{\lambda_c}}\bar{L}_{22}^{(1)} \right) + \frac{\mu}{\lambda_c}\left(\bar{L}_{11}^{(1)}\bar{L}_{22}^{(1)} + \bar{L}_{21}^{(1)}\bar{L}_{12}^{(1)} \right) \right],
\end{aligned}
\tag{A1.2.3}
$$

$$X_4^{[3]} = -\frac{1}{4}\left(\lambda_c \bar{L}_{11}^{(1)} \bar{L}_{22}^{(1)} + \frac{1}{\sqrt{\lambda_c}} \bar{L}_{11}^{(1)} \bar{L}_{33}^{(1)} + \frac{1}{\sqrt{\lambda_c}} \bar{L}_{22}^{(1)} \bar{L}_{33}^{(1)} + \frac{1}{\sqrt{\lambda_c}} \bar{L}_{31}^{(1)} \bar{L}_{13}^{(1)} - \frac{1}{\sqrt{\lambda_c}} \bar{L}_{32}^{(1)} \bar{L}_{23}^{(1)} + \lambda \bar{L}_{21}^{(1)} \bar{L}_{12}^{(1)} \right), \quad \text{(A1.2.4)}$$

$$X_5^{[3]} = \frac{1}{4} q_1 \left(\lambda_c \bar{L}_{22}^{(1)} + \frac{1}{\sqrt{\lambda_c}} \bar{L}_{33}^{(1)} \right) + \frac{1}{4} \frac{\mu}{\lambda_c} \left(\bar{L}_{22}^{(1)} \bar{L}_{33}^{(1)} - \bar{L}_{32}^{(1)} \bar{L}_{23}^{(1)} \right), \quad \text{(A1.2.5)}$$

$$X_6^{[3]} = \frac{1}{4} q_1 \left(-\lambda_c \bar{L}_{12}^{(1)} \right) + \frac{1}{4} \frac{\mu}{\lambda_c} \left(-\bar{L}_{32}^{(1)} \bar{L}_{13}^{(1)} - \bar{L}_{33}^{(1)} \bar{L}_{12}^{(1)} \right), \quad \text{(A1.2.6)}$$

$$X_7^{[3]} = \frac{1}{4} q_1 \left(-\frac{1}{\sqrt{\lambda_c}} \bar{L}_{13}^{(1)} \right) + \frac{1}{4} \frac{\mu}{\lambda_c} \left(-\bar{L}_{12}^{(1)} \bar{L}_{23}^{(1)} - \bar{L}_{22}^{(1)} \bar{L}_{13}^{(1)} \right). \quad \text{(A1.2.7)}$$

A1.3 Calculation of displacement field of group [3]

In this appendix, we show how to solve Eqs. (2.31)-(2.32) and obtain the displacement field of group [3]. We introduce two functions $\omega^{[3]}$ and $\psi^{[3]}$, and express functions $f_2^{[3]}(R)$, $g_2^{[3]}(R)$ and $h_2^{[3]}(R)$ as

$$f_2^{[3]}(R) = \frac{1}{\sqrt{\lambda_c}} \left(2\eta \omega_{,R}^{[3]} + \frac{2n}{R} \psi^{[3]} \right), \quad \text{(A1.3.1)}$$

$$g_2^{[3]}(R) = \frac{1}{\sqrt{\lambda_c}} \left(-\frac{4\eta n}{R} \omega^{[3]} - \psi_{,R}^{[3]} \right), \quad \text{(A1.3.2)}$$

$$h_2^{[3]}(R) = \lambda_c \left(-L_{2n}\left(\omega^{[3]} \right) + \frac{X_4^{[3]}}{2\eta} \right). \quad \text{(A1.3.3)}$$

The substitution of expressions (A1.3.1)-(A1.3.3) into Eq. (2-31) ensures the fourth equation of Eq. (2-31) is satisfied automatically.

Inserting (A1.3.3) to the third equation of Eq. (2-31), we obtain

$$\mu\lambda_c{}^2\left(-L_{2n}^2\left(\omega^{[3]}\right)+4\eta^2 L_{2n}\left(\omega^{[3]}\right)\right)+2\eta q_2^{[3]}=\lambda_c X_3^{[3]}-\mu\lambda_c{}^2\left(\frac{\partial^2}{\partial R^2}+\frac{1}{R}\frac{\partial}{\partial R}-\frac{4n^2}{R^2}-4\eta^2\right)\left(\frac{X_4^{[3]}}{2\eta}\right).$$

(A1.3.4)

We use $X_8^{[3]}$ to express the right hand side of Eq. (A1.3.4). Then Eq. (A1.3.4) becomes

$$\mu\lambda_c{}^2\left(-L_{2n}^2\left(\omega^{[3]}\right)+4\eta^2 L_{2n}\left(\omega^{[3]}\right)\right)+2\eta q_2^{[3]}=X_8^{[3]}. \tag{A1.3.5}$$

Substituting (A1.3.1)-(A1.3.3) into the first and second equations of Eq. (2-31), we have

$$\frac{\mu}{\lambda_c}\left[-2\eta\left(L_{2n}\left(\omega^{[3]}\right)\right)_{,R}-2n\frac{1}{R}L_{2n}\left(\psi^{[3]}\right)\right]+\frac{\mu}{\lambda_c}\left[4\eta^2\left(2\eta\omega_{,R}^{[3]}+\frac{2n}{R}\psi^{[3]}\right)\right]+\frac{\partial}{\partial R}q_2^{[3]}=\frac{1}{\sqrt{\lambda_c}}X_1^{[3]}.$$

(A1.3.6)

$$\frac{\mu}{\lambda_c}\left[\left(L_{2n}\left(\psi^{[3]}\right)\right)_{,R}+4\eta n\frac{1}{R}L_{2n}\left(\omega^{[3]}\right)\right]+\frac{\mu}{\lambda_c}\left(-4\eta^2\right)\left(\frac{4\eta n}{R}\omega^{[3]}+\psi_{,R}^{[3]}\right)-\frac{2n}{R}q_2^{[3]}=\frac{1}{\sqrt{\lambda_c}}X_2^{[3]}. \tag{A1.3.7}$$

Using (A1.3.6) and (A1.3.7) to vanish $q_2^{[3]}$, we obtain

$$L_{2n}^2\left(\psi^{[3]}\right)-4\eta^2 L_{2n}\left(\psi^{[3]}\right)=\frac{\sqrt{\lambda_c}}{\mu R}\left[2nX_1^{[3]}+\frac{\partial\left(RX_2^{[3]}\right)}{\partial R}\right]. \tag{A1.3.8}$$

We use $X_9^{[3]}$ to represent the right hand of Eq. (A1.3.8). Then Eq. (A1.3.8) becomes

$$L_{2n}^2\left(\psi^{[3]}\right)-4\eta^2 L_{2n}\left(\psi^{[3]}\right)=X_9^{[3]}. \tag{A1.3.9}$$

We introduce a function

$$\phi^{[3]} = L_{2n}\left(\psi^{[3]}\right). \tag{A1.3.10}$$

Inserting (A1.3.10) into (A1.3.9), we obtain

$$L_{2n}\left(\phi^{[3]}\right) - 4\eta^2\phi^{[3]} = X_9^{[3]}. \tag{A1.3.11}$$

The solution to (A1.3.11) can be separated into two parts

$$\phi^{[3]} = \phi_0^{[3]} + \phi_p^{[3]}, \tag{A1.3.12}$$

where $\phi_0^{[3]}$ represents the homogenous solution and $\phi_p^{[3]}$ represents the particular solution. The homogenous solution to Eq. (A1.3.11) can be written as

$$\phi_0^{[3]} = 4\eta^2\left[c_1^{[3]}I_{2n}\left(2\eta R\right) + c_2^{[3]}K_{2n}\left(2\eta R\right)\right]. \tag{A1.3.13}$$

Knowing the homogenous solution, we obtain the particular solution to Eq. (A1.3.11)

$$\phi_p^{[3]} = -K_{2n}\left(2\eta R\right)\int_{R_0}^{R} sI_{2n}\left(2\eta s\right)X_9^{[3]}\left(s\right)ds + I_{2n}\left(2\eta R\right)\int_{R_0}^{R} sK_{2n}\left(2\eta s\right)X_9^{[3]}\left(s\right)ds, \tag{A1.3.14}$$

where R_0 is a constant and we have used the Wronskian relation $I_{2n}\left(2\eta s\right)\frac{\partial K_{2n}\left(2\eta s\right)}{\partial s} - K_{2n}\left(2\eta s\right)\frac{\partial I_{2n}\left(2\eta s\right)}{\partial s} = -\frac{1}{s}$.

After we insert (A1.3.12) into (A1.3.10), Eq. (A1.3.10) can be written as

$$L_{2n}\left(\psi^{[3]}\right) = \phi_0^{[3]} + \phi_p^{[3]}. \tag{A1.3.15}$$

The solution to Eq. (A1.3.15) can be

$$\psi^{[3]} = \psi_0^{[3]} + \psi_{p1}^{[3]} + \psi_{p2}^{[3]}. \tag{A1.3.16}$$

where $\psi_0^{[3]}$ represents the homogenous solution. $\psi_{p1}^{[3]}$ and $\psi_{p2}^{[3]}$ are two parts of the particular solution. They can be written separately as

$$\psi_0^{[3]} = c_3^{[3]} R^{2n} + c_4^{[3]} R^{-2n}, \tag{A1.3.17}$$

$$\psi_{p1}^{[3]} = c_1^{[3]} I_{2n}\left(2\eta R\right) + c_2^{[3]} K_{2n}\left(2\eta R\right), \tag{A1.3.18}$$

$$\psi_{p2}^{[3]} = -R^{-2n}\int_{R_0}^{R} \frac{1}{4n} s^{2n+1} \phi_p^{[3]} ds + R^{2n}\int_{R_0}^{R} \frac{1}{4n} s^{-2n+1} \phi_p^{[3]} ds. \tag{A1.3.19}$$

Omitting $q_2^{[3]}$ by using (A1.3.5) and (A1.3.7), we can obtain

$$\begin{aligned} &\left(L_{2n} - 4\eta^2\right)\left(L_{2n} - 4\eta^2\rho^2\right)\omega^{[3]} \\ &= \frac{1}{2n\mu{\lambda_c}^2}\left[2\eta\frac{\mu}{\lambda_c} R\left(L_{2n}\left(\psi^{[3]}\right) - 4\eta^2\psi^{[3]}\right)_{,R} - \left(2\eta R\frac{1}{\sqrt{\lambda_c}} X_2^{[3]} + 2nX_8^{[3]}\right)\right]. \end{aligned} \tag{A1.3.20}$$

The term $L_{2n}\left(\psi^{[3]}\right) - 4\eta^2\psi^{[3]}$ can be expressed as

$$L_{2n}\left(\psi^{[3]}\right) - 4\eta^2\psi^{[3]} = \phi_p^{[3]} - 4\eta^2\psi_{p2}^{[3]} - 4\eta^2\left(c_3^{[3]} R^{2n} + c_4^{[3]} R^{-2n}\right). \tag{A1.3.21}$$

Then, Eq. (A1.3.20) becomes

$$\begin{aligned}&\left[\left(L_{2n}-4\eta^2\right)\left(L_{2n}-4\eta^2\rho^2\right)\omega^{[3]}\right]\\&=\frac{1}{2n\mu{\lambda_c}^2}\left[2\eta\frac{\mu}{\lambda_c}R\left(\phi_p^{[3]}-4\eta^2\psi_{p2}^{[3]}\right)_{,R}-\left(2\eta R\frac{1}{\sqrt{\lambda_c}}X_2^{[3]}+2nX_8^{[3]}\right)\right]\\&+8\eta^3\rho^2\left(-c_3^{[3]}R^{2n}+c_4^{[3]}R^{-2n}\right).\end{aligned}\tag{A1.3.22}$$

We use $X_{10}^{[3]}$ to represent one part of the right hand side of Eq. (A1.3.22), which does not include the unknown constant $c_3^{[3]}$ and $c_4^{[3]}$,

$$X_{10}^{[3]}=\frac{1}{2n\mu{\lambda_c}^2}\left[2\eta\frac{\mu}{\lambda_c}R\left(\phi_p^{[3]}-4\eta^2\psi_{p2}^{[3]}\right)_{,R}-\left(2\eta R\frac{1}{\sqrt{\lambda_c}}X_2^{[3]}+2nX_8^{[3]}\right)\right].\tag{A1.3.23}$$

Then Eq. (A1.3.22) becomes

$$\left(L_{2n}-4\eta^2\right)\left(L_{2n}-4\eta^2\rho^2\right)\omega^{[3]}=X_{10}^{[3]}+8\eta^3\rho^2\left(-c_3^{[3]}R^{2n}+c_4^{[3]}R^{-2n}\right).\tag{A1.3.34}$$

We introduce another function

$$\varphi^{[3]}=\left(L_{2n}-4\eta^2\rho^2\right)\omega^{[3]}.\tag{A1.3.25}$$

Then Eq. (A1.3.24) becomes

$$\left(L_{2n}-4\eta^2\right)\varphi^{[3]}=X_{10}^{[3]}+8\eta^3\rho^2\left(-c_3^{[3]}R^{2n}+c_4^{[3]}R^{-2n}\right).\tag{A1.3.26}$$

The solution to Eq. (A1.3.26) can be separated into three parts

$$\varphi^{[3]}=\varphi_0^{[3]}+\varphi_{p1}^{[3]}+\varphi_{p2}^{[3]}.\tag{A1.3.27}$$

The homogeneous solution is

$$\varphi_0^{[3]} = a_3^{[3]} I_{2n}\left(2\eta R\right) + a_4^{[3]} K_{2n}\left(2\eta R\right). \tag{A1.3.28}$$

The other two parts of particular solution can be obtained as

$$\varphi_{p1}^{[3]} = -K_{2n}\left(2\eta R\right)\int_{R_0}^{R} sI_{2n}\left(2\eta s\right) X_{10}^{[3]}\left(s\right)ds + I_{2n}\left(2\eta R\right)\int_{R_0}^{R} sK_{2n}\left(2\eta s\right) X_{10}^{[3]}\left(s\right)ds, \tag{A1.3.29}$$

$$\varphi_{p2}^{[3]} = 2\eta\rho^2\left(c_3^{[3]} R^{2n} - c_4^{[3]} R^{-2n}\right). \tag{A1.3.30}$$

Inserting Eq. (A1.3.27) into Eq. (A1.3.25), we obtain

$$\left(L_{2n} - 4\eta^2\rho^2\right)\omega^{[3]} = \varphi_0^{[3]} + \varphi_{p1}^{[3]} + \varphi_{p2}^{[3]}. \tag{A1.3.31}$$

The solution to Eq. (A1.3.31) can be separated into four parts

$$\omega^{[3]} = \omega_0^{[3]} + \omega_{p1}^{[3]} + \omega_{p2}^{[3]} + \omega_{p3}^{[3]}. \tag{A1.3.32}$$

The homogeneous solution is

$$\omega_0^{[3]} = a_1^{[3]} I_{2n}\left(2\rho\eta R\right) + a_2^{[3]} K_{2n}\left(2\rho\eta R\right). \tag{A1.3.33}$$

The other three parts of the particular solution are

$$\begin{aligned}
\omega_{p1}^{[3]} = {} & a_3^{[3]}\Big[-K_{2n}\left(2\rho\eta R\right)\int_{R_0}^{R} sI_{2n}\left(2\rho\eta s\right) I_{2n}\left(2\eta s\right)ds \\
& + I_{2n}\left(2\rho\eta R\right)\int_{R_0}^{R} sK_{2n}\left(2\rho\eta s\right) I_{2n}\left(2\eta s\right)ds\Big] \\
& + a_4^{[3]}\Big[-K_{2n}\left(2\rho\eta R\right)\int_{R_0}^{R} sI_{2n}\left(2\rho\eta s\right) K_{2n}\left(2\eta s\right)ds \\
& + I_{2n}\left(2\rho\eta R\right)\int_{R_0}^{R} sK_{2n}\left(2\rho\eta s\right) K_{2n}\left(2\eta s\right)ds\Big],
\end{aligned} \tag{A1.3.34}$$

$$\omega_{p2}^{[3]} = -K_{2n}\left(2\rho\eta R\right)\int_{R_0}^{R} sI_{2n}\left(2\rho\eta s\right)\varphi_{p1}^{[3]}\left(s\right)ds + I_{2n}\left(2\rho\eta R\right)\int_{R_0}^{R} sK_{2n}\left(2\rho\eta s\right)\varphi_{p1}^{[3]}\left(s\right)ds, \tag{A1.3.35}$$

$$\omega_{p3}^{[3]} = \frac{1}{2\eta}\left(-c_3^{[3]}R^{2n} + c_4^{[3]}R^{-2n}\right). \tag{A1.3.36}$$

Substituting (A1.3.16) and (A1.3.32) into (A1.3.1)-(A1.3.3), we find that R^{2n} and R^{-2n} give null displacement field, which means the variation of parameters $c_3^{[3]}$ and $c_4^{[3]}$ does not influence the displacement field. Therefore, we set $c_3^{[3]}$ and $c_4^{[3]}$ as 0. We set constant R_0 as 1. Then, the parameters $c_i^{[3]}$ and $a_j^{[3]}$ $\left(i=1,2; j=1,2,3,4\right)$ can be solved by substituting (A1.3.1)-(A1.3.3) into the boundary conditions (2.32) at $R=A$ and $R=B$, after which functions $f_2^{[3]}\left(R\right)$, $g_2^{[3]}\left(R\right)$ and $h_2^{[3]}\left(R\right)$ are obtained. $q_2^{[3]}$ can be calculated from Eq. (2.31). From Eq. (2.33), the displacement field of group [3], $\mathbf{U}_2^{[3]}$ is known. The calculation of the displacement field of other groups is similar to the procedure described above.

A1.4 Equations of group [2]

In this appendix, we list the linear differential equations of group [2]. The governing equations are

$$\mu\left(\frac{1}{R^2}-\frac{1}{R}\frac{\partial}{\partial R}-\frac{\partial^2}{\partial R^2}+4\eta^2\right)f_2^{[2]}+\sqrt{\lambda_c}\frac{\partial}{\partial R}q_2^{[2]}=X_1^{[2]}, \tag{A1.4.1}$$

$$\mu\left(\frac{1}{R^2}-\frac{1}{R}\frac{\partial}{\partial R}-\frac{\partial^2}{\partial R^2}+4\eta^2\right)g_2^{[2]}=0, \tag{A1.4.2}$$

$$\mu\left(\frac{\partial^2}{\partial R^2}+\frac{1}{R}\frac{\partial}{\partial R}-4\eta^2\right)h_2^{[2]}+2\eta\frac{1}{\lambda_c}q_2^{[2]}=X_2^{[2]}, \tag{A1.4.3}$$

$$\sqrt{\lambda_c} f_{2,R}^{[2]} + \sqrt{\lambda_c}\frac{f_2^{[2]}}{R} + \frac{1}{\lambda_c} 2\eta h_2^{[2]} = X_3^{[2]}. \tag{A1.4.4}$$

The boundary conditions at $R = A$ and $R = B$ are

$$\mu\left(f_{2,R}^{[2]}\right) - \sqrt{\lambda_c} q_2^{[2]} - \mu\left[\frac{f_2^{[2]}}{R} + \left(\frac{1}{\lambda_c\sqrt{\lambda_c}}\right) 2\eta h_2^{[2]}\right] = X_4^{[2]}, \tag{A1.4.5}$$

$$\mu\left(g_{2,R}^{[2]}\right) + \mu\left(\frac{-g_2^{[2]}}{R}\right) = 0, \tag{A1.4.6}$$

$$\mu\left(h_{2,R}^{[2]}\right) - \mu\frac{1}{\lambda_c\sqrt{\lambda_c}}\left(2\eta f_2^{[2]}\right) = X_5^{[2]}. \tag{A1.4.7}$$

The expressions of $X_i^{[2]}$ $\left(i = 1, 2, \cdots, 5\right)$ are

$$\begin{aligned} X_1^{[2]} = {} & \frac{1}{4}\left[q_1\left(\frac{1}{R}\lambda_c \bar{L}_{11}^{(1)} + \frac{1}{R}\frac{1}{\sqrt{\lambda_c}}\bar{L}_{33}^{(1)}\right) + \frac{\mu}{\lambda_c}\left(\frac{1}{R}\bar{L}_{11}^{(1)}\bar{L}_{33}^{(1)} + \frac{1}{R}\bar{L}_{31}^{(1)}\bar{L}_{13}^{(1)}\right)\right] \\ & -\frac{1}{4}\frac{1}{R}\left\{R\left[q_1\left(\lambda_c \bar{L}_{22}^{(1)} + \frac{1}{\sqrt{\lambda_c}}\bar{L}_{33}^{(1)}\right) + \frac{\mu}{\lambda_c}\left(\bar{L}_{22}^{(1)}\bar{L}_{33}^{(1)} + \bar{L}_{32}^{(1)}\bar{L}_{23}^{(1)}\right)\right]\right\}_{,R} \\ & -\frac{1}{2}\eta\left[q_1\left(-\frac{1}{\sqrt{\lambda_c}}\bar{L}_{31}^{(1)}\right) + \frac{\mu}{\lambda_c}\left(\bar{L}_{21}^{(1)}\bar{L}_{32}^{(1)} - \bar{L}_{31}^{(1)}\bar{L}_{22}^{(1)}\right)\right], \end{aligned} \tag{A1.4.8}$$

$$\begin{aligned} X_2^{[2]} = {} & \frac{1}{4}\frac{1}{R}\left\{R\left[q_1\left(-\frac{1}{\sqrt{\lambda_c}}\bar{L}_{13}^{(1)}\right) + \frac{\mu}{\lambda_c}\left(\bar{L}_{12}^{(1)}\bar{L}_{23}^{(1)} - \bar{L}_{22}^{(1)}\bar{L}_{13}^{(1)}\right)\right]\right\}_{,R} \\ & -\frac{1}{2}\eta\left[q_1\left(\frac{1}{\sqrt{\lambda_c}}\bar{\eta}_{11}^{(1)} + \frac{1}{\sqrt{\lambda_c}}\bar{\eta}_{22}^{(1)}\right) + \frac{\mu}{\lambda_c}\left(\bar{L}_{11}^{(1)}\bar{L}_{22}^{(1)} - \bar{L}_{21}^{(1)}\bar{L}_{12}^{(1)}\right)\right], \end{aligned} \tag{A1.4.9}$$

$$X_3^{[2]} = -\frac{1}{4}\left(\lambda_c \bar{L}_{11}^{(1)} \bar{L}_{22}^{(1)} + \frac{1}{\sqrt{\lambda_c}} \bar{L}_{11}^{(1)} \bar{L}_{33}^{(1)} + \frac{1}{\sqrt{\lambda_c}} \bar{L}_{22}^{(1)} \bar{L}_{33}^{(1)} + \frac{1}{\sqrt{\lambda_c}} \bar{L}_{31}^{(1)} \bar{L}_{13}^{(1)} + \frac{1}{\sqrt{\lambda_c}} \bar{L}_{32}^{(1)} \bar{L}_{23}^{(1)} - \lambda_c \bar{L}_{21}^{(1)} \bar{L}_{12}^{(1)} \right), \quad \text{(A1.4.10)}$$

$$X_4^{[2]} = \frac{1}{4} q_1 \left(\lambda_c \bar{L}_{22}^{(1)} + \frac{1}{\sqrt{\lambda_c}} \bar{L}_{33}^{(1)} \right) + \frac{1}{4} \frac{\mu}{\lambda_c} \left(\bar{L}_{22}^{(1)} \bar{L}_{33}^{(1)} + \bar{L}_{32}^{(1)} \bar{L}_{23}^{(1)} \right), \quad \text{(A1.4.11)}$$

$$X_5^{[2]} = \frac{1}{4} q_1 \left(-\frac{1}{\sqrt{\lambda_c}} \bar{L}_{13}^{(1)} \right) + \frac{1}{4} \frac{\mu}{\lambda_c} \left(\bar{L}_{12}^{(1)} \bar{L}_{23}^{(1)} - \bar{L}_{22}^{(1)} \bar{L}_{13}^{(1)} \right). \quad \text{(A1.4.12)}$$

A1.5 Calculation of displacement field of group [2]

In this appendix, we show how Eqs. (A1.4.1)-(A1.4.7) are solved.

The displacement field of group [2] can be denoted as

$$\mathbf{U}_2^{[2]} = \left(U_{2R}^{[2]}, U_{2\Theta}^{[2]}, U_{2Z}^{[2]}, p_2^{[2]} \right) = \begin{pmatrix} f_2^{[2]}(R)\cos 2\eta Z \\ g_2^{[2]}(R)\cos 2\eta Z \\ h_2^{[2]}(R)\sin 2\eta Z \\ q_2^{[2]}(R)\cos 2\eta Z \end{pmatrix}^T . \quad \text{(A1.5.1)}$$

From the governing equations and boundary conditions, we can easily see $g_2^{[2]} = 0$.

We introduce one function $\omega^{[2]}$ and express functions $f_2^{[2]}(R)$ and $h_2^{[2]}(R)$ as

$$f_2^{[2]}(R) = \frac{1}{\sqrt{\lambda_c}} \left(2\eta \omega_{,R}^{[2]} \right), \quad \text{(A1.5.2)}$$

$$h_2^{[2]}(R) = \lambda_c \left(-L_0\left(\omega^{[2]} \right) + \frac{X_3^{[2]}}{2\eta} \right). \quad \text{(A1.5.3)}$$

The introduction of (A1.5.2) and (A1.5.3) ensures Eq. (A1.4.4) is satisfied automatically.

Inserting (A1.5.3) to (A1.4.3), we obtain

$$\mu\lambda_c{}^2\left(-L_0^2\left(\omega^{[2]}\right)+4\eta^2 L_0\left(\omega^{[2]}\right)\right)+2\eta q_2^{[2]}=\lambda_c X_2^{[2]}-\mu\lambda_c{}^2\left(\frac{\partial^2}{\partial R^2}+\frac{1}{R}\frac{\partial}{\partial R}-4\eta^2\right)\left(\frac{X_3^{[2]}}{2\eta}\right). \tag{A1.5.4}$$

We use $X_6^{[2]}$ to express the right hand of Eq. (A1.5.4). Then Eq. (A1.5.4) becomes

$$\mu\lambda_c{}^2\left(-L_0^2\left(\omega^{[2]}\right)+4\eta^2 L_0\left(\omega^{[2]}\right)\right)+2\eta q_2^{[2]}=X_6^{[2]}. \tag{A1.5.5}$$

Using (A1.4.1) and (A1.5.5) to vanish $q_2^{[2]}$, we obtain

$$\left[\left(L_0-4\eta^2\right)\left(L_0-4\eta^2\rho^2\right)\omega^{[2]}\right]_{,R}=\frac{1}{\mu\lambda_c{}^2}\left(2\eta\frac{1}{\sqrt{\lambda_c}}X_1^{[2]}-X_{6,R}^{[2]}\right). \tag{A1.5.6}$$

We represent the right hand of Eq. (A1.5.6) as $X_7^{[2]}$. The integration of Eq. (A1.5.6) gives

$$\left(L_0-4\eta^2\right)\left(L_0-4\eta^2\rho^2\right)\omega^{[2]}=\int_{R_0}^{R}X_7^{[2]}(s)\,ds+c_1^{[2]}. \tag{A1.5.7}$$

The constant $c_1^{[2]}$ does not influence the displacement field. We set $c_1^{[2]}$ as 0.

We use $X_8^{[2]}$ to represent the right hand of Eq. (A1.5.7) and introduce a function

$$\varphi^{[2]}=\left(L_0-4\eta^2\rho^2\right)\omega^{[2]}. \tag{A1.5.8}$$

Eq. (A1.5.7) becomes

$$\left(L_0-4\eta^2\right)\varphi^{[2]}=X_8^{[2]}. \tag{A1.5.9}$$

The solution to (A1.5.9) can be separated into two parts

$$\varphi^{[2]} = \varphi_0^{[2]} + \varphi_p^{[2]}. \tag{A1.5.10}$$

The homogeneous solution is

$$\varphi_0^{[2]} = a_3^{[2]} I_0\left(2\eta R\right) + a_4^{[2]} K_0\left(2\eta R\right). \tag{A1.5.11}$$

The particular solution is

$$\varphi_p^{[2]} = -K_0\left(2\eta R\right)\int_{R_0}^{R} sI_0\left(2\eta s\right) X_8^{[2]}\left(s\right)ds + I_0\left(2\eta R\right)\int_{R_0}^{R} sK_0\left(2\eta s\right) X_8^{[2]}\left(s\right)ds. \tag{A1.5.12}$$

After we insert Eq. (A1.5.10) into Eq. (A1.5.8), Eq. (A1.5.8) becomes

$$\left(L_0 - 4\eta^2\rho^2\right)\omega^{[2]} = \varphi_0^{[2]} + \varphi_p^{[2]}. \tag{A1.5.13}$$

The solution to Eq. (A1.5.13) can be separated into three parts

$$\omega^{[2]} = \omega_0^{[2]} + \omega_{p1}^{[2]} + \omega_{p2}^{[2]}. \tag{A1.5.14}$$

The homogeneous solution is

$$\omega_0^{[2]} = a_1^{[2]} I_0\left(2\rho\eta R\right) + a_2^{[2]} K_0\left(2\rho\eta R\right). \tag{A1.5.15}$$

The other two parts of the particular solution are

$$\begin{aligned}\omega_{p1}^{[2]} = {} & a_3^{[2]}\left[-K_0\left(2\rho\eta R\right)\int_{R_0}^{R} sI_0\left(2\rho\eta s\right) I_0\left(2\eta s\right)ds + I_0\left(2\rho\eta R\right)\int_{R_0}^{R} sK_0\left(2\rho\eta s\right) I_0\left(2\eta s\right)ds\right] \\ & + a_4^{[2]}\left[-K_0\left(2\rho\eta R\right)\int_{R_0}^{R} sI_0\left(2\rho\eta s\right) K_0\left(2\eta s\right)ds + I_0\left(2\rho\eta R\right)\int_{R_0}^{R} sK_0\left(2\rho\eta s\right) K_0\left(2\eta s\right)ds\right],\end{aligned} \tag{A1.5.16}$$

$$\omega_{p2}^{[2]} = -K_0\left(2\rho\eta R\right)\int_{R_0}^{R} sI_0\left(2\rho\eta s\right)\varphi_p^{[2]}\left(s\right)ds + I_0\left(2\rho\eta R\right)\int_{R_0}^{R} sK_0\left(2\rho\eta s\right)\varphi_p^{[2]}\left(s\right)ds. \tag{A1.5.17}$$

The parameters $a_i^{[2]}$ $\left(i=1,2,3,4\right)$ can be solved by the boundary conditions (A1.4.5) and (A1.4.7). Then the displacement field of group [2] can be obtained.

A1.6 Equations of group [1]

In this appendix, we list the linear differential equations of group [1]. The governing equations are

$$\mu\left(\frac{1}{R^2}-\frac{1}{R}\frac{\partial}{\partial R}-\frac{\partial^2}{\partial R^2}+\frac{4n^2}{R^2}\right)f_2^{[1]}+\mu\left(\frac{4n}{R^2}\right)g_2^{[1]}+\sqrt{\lambda_c}\frac{\partial}{\partial R}q_2^{[1]}=X_1^{[1]}, \tag{A1.6.1}$$

$$\mu\left(\frac{1}{R^2}-\frac{1}{R}\frac{\partial}{\partial R}-\frac{\partial^2}{\partial R^2}+\frac{4n^2}{R^2}\right)g_2^{[1]}+\mu\left(\frac{4n}{R^2}\right)f_2^{[1]}-\sqrt{\lambda_c}\frac{2n}{R}q_2^{[1]}=X_2^{[1]}, \tag{A1.6.2}$$

$$\mu\left(\frac{\partial^2}{\partial R^2}+\frac{1}{R}\frac{\partial}{\partial R}-\frac{4n^2}{R^2}\right)h_2^{[1]}=0, \tag{A1.6.3}$$

$$\sqrt{\lambda_c}f_{2,R}^{[1]}+\sqrt{\lambda_c}\frac{f_2^{[1]}+2ng_2^{[1]}}{R}=X_3^{[1]}. \tag{A1.6.4}$$

The boundary conditions are

$$\mu\left(f_{2,R}^{[1]}\right)-\sqrt{\lambda_c}q_2^{[1]}-\mu\left(\frac{f_2^{[1]}+2ng_2^{[1]}}{R}\right)=X_4^{[1]}, \tag{A1.6.5}$$

$$\mu\left(g_{2,R}^{[1]}\right)+\mu\left(\frac{-2nf_2^{[1]}-g_2^{[1]}}{R}\right)=X_5^{[1]}, \tag{A1.6.6}$$

$$\mu\left(h_{2\ ,R}^{[1]}\right)=0\,. \tag{A1.6.7}$$

The expressions of $X_i^{[1]}\ \left(i=1,2,\cdots,5\right)$ are

$$\begin{aligned}X_1^{[1]}=&\frac{1}{4}\left[q_1\left(\frac{1}{R}\lambda_c\bar{L}_{11}^{(1)}+\frac{1}{R}\frac{1}{\sqrt{\lambda_c}}\bar{L}_{33}^{(1)}\right)+\frac{\mu}{\lambda_c}\left(\frac{1}{R}\bar{L}_{11}^{(1)}\bar{L}_{33}^{(1)}-\frac{1}{R}\bar{L}_{31}^{(1)}\bar{L}_{13}^{(1)}\right)\right]\\&-\frac{1}{4}\frac{1}{R}\left\{R\left[q_1\left(\lambda_c\bar{L}_{22}^{(1)}+\frac{1}{\sqrt{\lambda_c}}\bar{L}_{33}^{(1)}\right)+\frac{\mu}{\lambda_c}\left(\bar{L}_{22}^{(1)}\bar{L}_{33}^{(1)}+\bar{L}_{32}^{(1)}\bar{L}_{23}^{(1)}\right)\right]\right\}_{,R}\\&-\frac{1}{2}n\left[q_1\left(-\lambda_c\frac{1}{R}\bar{L}_{21}^{(1)}\right)+\frac{\mu}{\lambda_c}\left(\frac{1}{R}\bar{L}_{31}^{(1)}\bar{L}_{23}^{(1)}-\frac{1}{R}\bar{L}_{33}^{(1)}\bar{L}_{21}^{(1)}\right)\right],\end{aligned} \tag{A1.6.8}$$

$$\begin{aligned}X_2^{[1]}=&\frac{1}{4}\left[q_1\left(\lambda_c\frac{1}{R}\bar{L}_{21}^{(1)}\right)+\frac{\mu}{\lambda_c}\left(-\frac{1}{R}\bar{L}_{31}^{(1)}\bar{L}_{23}^{(1)}+\frac{1}{R}\bar{L}_{33}^{(1)}\bar{L}_{21}^{(1)}\right)\right]\\&-\frac{1}{4}\frac{1}{R}\left[R\left[q_1\left(-\lambda_c\bar{L}_{12}^{(1)}\right)+\frac{\mu}{\lambda_c}\left(\bar{L}_{32}^{(1)}\bar{L}_{13}^{(1)}-\bar{L}_{33}^{(1)}\bar{L}_{12}^{(1)}\right)\right]\right]_{,R}\\&+\frac{1}{2}n\left[q_1\left(\frac{1}{R}\lambda_c\bar{L}_{11}^{(1)}+\frac{1}{\sqrt{\lambda_c}}\frac{1}{R}\bar{L}_{33}^{(1)}\right)+\frac{\mu}{\lambda_c}\left(\frac{1}{R}\bar{L}_{11}^{(1)}\bar{L}_{33}^{(1)}-\frac{1}{R}\bar{L}_{31}^{(1)}\bar{L}_{13}^{(1)}\right)\right],\end{aligned} \tag{A1.6.9}$$

$$X_3^{[1]}=-\frac{1}{4}\left(\lambda_c\bar{L}_{11}^{(1)}\bar{L}_{22}^{(1)}+\frac{1}{\sqrt{\lambda_c}}\bar{L}_{11}^{(1)}\bar{L}_{33}^{(1)}+\frac{1}{\sqrt{\lambda_c}}\bar{L}_{22}^{(1)}\bar{L}_{33}^{(1)}-\frac{1}{\sqrt{\lambda_c}}\bar{L}_{31}^{(1)}\bar{L}_{13}^{(1)}+\frac{1}{\sqrt{\lambda_c}}\bar{L}_{32}^{(1)}\bar{L}_{23}^{(1)}+\lambda_c\bar{L}_{21}^{(1)}\bar{L}_{12}^{(1)}\right), \tag{A1.6.10}$$

$$X_4^{[1]}=\frac{1}{4}q_1\left(\lambda_c\bar{L}_{22}^{(1)}+\frac{1}{\sqrt{\lambda_c}}\bar{L}_{33}^{(1)}\right)+\frac{1}{4}\frac{\mu}{\lambda_c}\left(\bar{L}_{22}^{(1)}\bar{L}_{33}^{(1)}+\bar{L}_{32}^{(1)}\bar{L}_{23}^{(1)}\right), \tag{A1.6.11}$$

$$X_5^{[1]}=\frac{1}{4}q_1\left(-\lambda_c\bar{L}_{12}^{(1)}\right)+\frac{1}{4}\frac{\mu}{\lambda_c}\left(\bar{L}_{32}^{(1)}\bar{L}_{13}^{(1)}-\bar{L}_{33}^{(1)}\bar{L}_{12}^{(1)}\right). \tag{A1.6.12}$$

A1.7 Calculation of displacement field of group [1]

In this appendix, we show how Eqs. (A1.6.1)-(A1.6.7) are solved.

The displacement field of group [1] can be denoted as

$$\mathbf{U}_2^{[1]} = \left(U_{2R}^{[1]}, U_{2\Theta}^{[1]}, U_{2Z}^{[1]}, p_2^{[1]}\right) = \begin{pmatrix} f_2^{[1]}(R)\cos 2n\Theta \\ g_2^{[1]}(R)\sin 2n\Theta \\ h_2^{[1]}(R)\cos 2n\Theta \\ q_2^{[1]}(R)\cos 2n\Theta \end{pmatrix}^T . \tag{A1.7.1}$$

From the governing equations and boundary conditions, we can easily see $h_2^{[1]} = 0$.

We introduce one function $\psi^{[2]}$ and express functions $f_2^{[1]}(R)$ and $g_2^{[1]}(R)$ as

$$f_2^{[1]}(R) = \frac{1}{\sqrt{\lambda_c}}\left(\frac{2n}{R}\psi^{[1]}\right), \tag{A1.7.2}$$

$$g_2^{[1]}(R) = \frac{1}{\sqrt{\lambda_c}}\left(\frac{R}{2n}X_3^{[1]} - \psi_{,R}^{[1]}\right). \tag{A1.7.3}$$

The introduction of (A1.7.2) and (A1.7.3) ensures Eq. (A1.6.4) is satisfied automatically.

Substitution of (A1.7.2) and (A1.7.3) into (A1.6.1) gives

$$\frac{\mu}{\lambda_c}\left(-2n\frac{1}{R}L_{2n}\left(\psi^{[1]}\right)\right) + \frac{\partial}{\partial R}q_2^{[1]} = \frac{1}{\sqrt{\lambda_c}}X_1^{[1]} - \frac{\mu}{\lambda_c}\left(\frac{4n}{R^2}\right)\left(\frac{R}{2n}X_3^{[1]}\right). \tag{A1.7.4}$$

We use $X_6^{[1]}$ to express the right hand of Eq. (A1.7.4). Then Eq. (A1.7.4) becomes

$$\frac{\mu}{\lambda_c}\left(-2n\frac{1}{R}L_{2n}\left(\psi^{[1]}\right)\right) + \frac{\partial}{\partial R}q_2^{[1]} = X_6^{[1]}. \tag{A1.7.5}$$

After we substitute (A1.7.2) and (A1.7.3) into (A1.6.2), (A1.6.2) becomes

$$\frac{\mu}{\lambda_c}\left(L_{2n}\left(\psi^{[1]}\right)\right)_{,R}-\frac{2n}{R}q_2^{[1]}=\frac{1}{\sqrt{\lambda_c}}X_2^{[1]}-\frac{\mu}{\lambda_c}\left(\frac{1}{R^2}-\frac{1}{R}\frac{\partial}{\partial R}-\frac{\partial^2}{\partial R^2}+\frac{4n^2}{R^2}\right)\left(\frac{R}{2n}X_3^{[1]}\right). \tag{A1.7.6}$$

We use $X_7^{[1]}$ to express the right hand of Eq. (A1.7.6). Then Eq. (A1.7.6) becomes

$$\frac{\mu}{\lambda_c}\left(L_{2n}\left(\psi^{[1]}\right)\right)_{,R}-\frac{2n}{R}q_2^{[1]}=X_7^{[1]}. \tag{A1.7.7}$$

Using (A1.7.5) and (A1.7.7) to vanish $q_2^{[1]}$, we obtain

$$L_{2n}^2\left(\psi^{[1]}\right)=\frac{\lambda_c}{\mu R}\left(2nX_6^{[1]}+X_7^{[1]}+RX_{7,R}^{[1]}\right). \tag{A1.7.8}$$

We use $X_8^{[1]}$ to express the right hand of Eq. (A1.7.8). Then Eq. (A1.7.8) becomes

$$L_{2n}^2\left(\psi^{[1]}\right)=X_8^{[1]}. \tag{A1.7.9}$$

We introduce a function

$$\phi^{[1]}=L_{2n}\left(\psi^{[1]}\right). \tag{A1.7.10}$$

Then (A1.7.9) becomes

$$L_{2n}\left(\phi^{[1]}\right)=X_8^{[1]}. \tag{A1.7.11}$$

The solution to (A1.7.11) can be separated into two parts

$$\phi^{[1]}=\phi_0^{[1]}+\phi_p^{[1]}. \tag{A1.7.12}$$

The homogenous solution to Eq. (A1.7.11) can be written as

$$\phi_0^{[1]} = c_1^{[1]} R^{2n} + c_2^{[1]} R^{-2n}. \tag{A1.7.13}$$

The particular solution to Eq. (A1.7.11) can be written as

$$\phi_p^{[1]} = -R^{-2n} \int_{R_0}^{R} \frac{1}{4n} s^{2n+1} X_8^{[1]}(s) ds + R^{2n} \int_{R_0}^{R} \frac{1}{4n} s^{-2n+1} X_8^{[1]}(s) ds. \tag{A1.7.14}$$

Inserting (A1.7.12) into (A1.7.10), we obtain

$$L_{2n}\left(\psi^{[1]}\right) = \phi_0^{[1]} + \phi_p^{[1]}. \tag{A1.7.15}$$

The solution to Eq. (A1.7.15) can be

$\psi^{[1]} = \psi_0^{[1]} + \psi_{p1}^{[1]} + \psi_{p2}^{[1]}$, where $\psi_0^{[1]}$ represents the homogenous solution, and $\psi_{p1}^{[1]}$ and $\psi_{p2}^{[1]}$ are the two parts of the particular solution. They can be written separately as

$$\psi_0^{[1]} = c_3^{[1]} R^{2n} + c_4^{[1]} R^{-2n}, \tag{A1.7.16}$$

$$\psi_{p1}^{[1]} = c_1^{[1]} \left(-R^{-2n} \int_{R_0}^{R} \frac{1}{4n} s^{4n+1} ds + R^{2n} \int_{R_0}^{R} \frac{1}{4n} s ds \right) + c_2^{[1]} \left(-R^{-2n} \int_{R_0}^{R} \frac{1}{4n} s ds + R^{2n} \int_{R_0}^{R} \frac{1}{4n} s^{-4n+1} ds \right), \tag{A1.7.17}$$

$$\psi_{p2}^{[1]} = -R^{-2n} \int_{R_0}^{R} \frac{1}{4n} s^{2n+1} \phi_p^{[1]} ds + R^{2n} \int_{R_0}^{R} \frac{1}{4n} s^{-2n+1} \phi_p^{[1]} ds. \tag{A1.7.18}$$

The parameters $c_i^{[1]}$ $(i = 1,2,3,4)$ can be solved by the boundary conditions (A1.6.5) and (A1.6.6). Then the displacement field of group [1] can be obtained.

A1.8 Equations of group [0]

In this appendix, we list the linear differential equations of group [0]. The governing equations are

$$\mu\left(\frac{1}{R^2}-\frac{1}{R}\frac{\partial}{\partial R}-\frac{\partial^2}{\partial R^2}\right)f_2^{[0]}+\sqrt{\lambda_c}\,\frac{\partial}{\partial R}q_2^{[0]}=X_1^{[0]}, \tag{A1.8.1}$$

$$\mu\left(\frac{1}{R^2}-\frac{1}{R}\frac{\partial}{\partial R}-\frac{\partial^2}{\partial R^2}\right)g_2^{[0]}=0, \tag{A1.8.2}$$

$$\mu\left(\frac{\partial^2}{\partial R^2}+\frac{1}{R}\frac{\partial}{\partial R}\right)h_2^{[0]}=0, \tag{A1.8.3}$$

$$\sqrt{\lambda_c}f_2^{[0]}{}_{,R}+\sqrt{\lambda_c}\,\frac{f_2^{[0]}}{R}=X_2^{[0]}. \tag{A1.8.4}$$

The boundary conditions at $R=A$ and $R=B$ are

$$\mu\left(f_2^{[0]}{}_{,R}\right)-\sqrt{\lambda_c}q_2^{[0]}-\mu\left(\frac{f_2^{[0]}}{R}\right)=X_3^{[0]}, \tag{A1.8.5}$$

$$\mu\left(g_2^{[0]}{}_{,R}\right)+\mu\left(\frac{-g_2^{[0]}}{R}\right)=0, \tag{A1.8.6}$$

$$\mu\left(h_2^{[0]}{}_{,R}\right)=0. \tag{A1.8.7}$$

The expressions of $X_i^{[0]}\ \left(i=1,2,3\right)$ are

$$X_1^{[0]}=\frac{1}{4}\left[q_1\left(\frac{1}{R}\lambda_c\bar{L}_{11}^{(1)}+\frac{1}{R}\frac{1}{\sqrt{\lambda_c}}\bar{L}_{33}^{(1)}\right)+\frac{\mu}{\lambda_c}\left(\frac{1}{R}\bar{L}_{11}^{(1)}\bar{L}_{33}^{(1)}-\frac{1}{R}\bar{L}_{31}^{(1)}\bar{L}_{13}^{(1)}\right)\right]$$
$$-\frac{1}{4}\frac{1}{R}\left\{R\left[q_1\left(\lambda_c\bar{L}_{22}^{(1)}+\frac{1}{\sqrt{\lambda_c}}\bar{L}_{33}^{(1)}\right)+\frac{\mu}{\lambda_c}\left(\bar{L}_{22}^{(1)}\bar{L}_{33}^{(1)}-\bar{L}_{32}^{(1)}\bar{L}_{23}^{(1)}\right)\right]\right\}_{,R}, \tag{A1.8.8}$$

$$X_2^{[0]}=-\frac{1}{4}\left(\lambda_c\bar{L}_{11}^{(1)}\bar{L}_{22}^{(1)}+\frac{1}{\sqrt{\lambda_c}}\bar{L}_{11}^{(1)}\bar{L}_{33}^{(1)}+\frac{1}{\sqrt{\lambda_c}}\bar{L}_{22}^{(1)}\bar{L}_{33}^{(1)}-\frac{1}{\sqrt{\lambda_c}}\bar{L}_{31}^{(1)}\bar{L}_{13}^{(1)}-\frac{1}{\sqrt{\lambda_c}}\bar{L}_{32}^{(1)}\bar{L}_{23}^{(1)}-\lambda_c\bar{L}_{21}^{(1)}\bar{L}_{12}^{(1)}\right), \tag{A1.8.9}$$

$$X_3^{[0]}=\frac{1}{4}q_1\left(\lambda_c\bar{L}_{22}^{(1)}+\frac{1}{\sqrt{\lambda_c}}\bar{L}_{33}^{(1)}\right)+\frac{1}{4}\frac{\mu}{\lambda_c}\left(\bar{L}_{22}^{(1)}\bar{L}_{33}^{(1)}-\bar{L}_{32}^{(1)}\bar{L}_{23}^{(1)}\right). \tag{A1.8.10}$$

A1.9 Calculation of displacement field of group [0]

In this appendix, we show how Eqs. (A1.8.1)-(A1.8.7) are solved.

The displacement field of group [0] can be denoted as

$$\mathbf{U}_2^{[0]}=\left(U_{2R}^{[0]},U_{2\Theta}^{[0]},U_{2Z}^{[0]},p_2^{[0]}\right)=\begin{pmatrix}f_2^{[0]}(R)\\ g_2^{[0]}(R)\\ h_2^{[0]}(R)\\ q_2^{[0]}(R)\end{pmatrix}^T. \tag{A1.9.1}$$

From the governing equations and boundary conditions, we can easily see $h_2^{[0]}=0$ and $g_2^{[0]}=0$.

From Eq. (A1.8.4), $f_2^{[0]}$ can be calculated as

$$f_2^{[0]}=\frac{1}{R}\left(\int_{R_0}^{R}s\frac{1}{\sqrt{\lambda_c}}X_2^{[0]}(s)\,ds+c_1^{[0]}\right). \tag{A1.9.2}$$

After we substitute (A1.9.2) to (A1.8.1), $q_2^{[0]}$ can be calculated as

$$q_2^{[0]} = \int_{R_0}^{R} \left(\frac{1}{\sqrt{\lambda_c}} X_1^{[0]} + \mu \frac{1}{\lambda_c} X_2^{[0]}{}_{,R} \right) ds + c_2^{[0]}. \tag{A1.9.3}$$

Substituting (A1.9.2) and (A1.9.3) to the boundary condition (A1.8.5), we can obtain the parameters $c_1^{[0]}$ and $c_2^{[0]}$. Then the displacement field of group [0] is known.

A1.10 Postbuckling analysis of the barreling mode

For the barreling mode, by setting n as 0, letting the displacement field of group [3] equal the displacement field of group [2] and the displacement field of group [1] equal the displacement field of group [0], and removing $U_{2\Theta}$ in Eq. (29), we rewrite the particular solution of $\mathbf{U}_2$ as

$$\begin{cases} U_{2R} = f_2^{[0]}(R) + f_2^{[1]}(R) + f_2^{[2]}(R)\cos 2\eta Z + f_2^{[3]}(R)\cos 2\eta Z = 2\left[f_2^{[0]}(R) + f_2^{[2]}(R)\cos 2\eta Z \right], \\ U_{2Z} = h_2^{[0]}(R) + h_2^{[1]}(R) + h_2^{[2]}(R)\sin 2\eta Z + h_2^{[3]}(R)\sin 2\eta Z = 2\left[h_2^{[0]}(R) + h_2^{[2]}(R)\sin 2\eta Z \right], \\ p_2 = q_2^{[0]}(R) + q_2^{[1]}(R) + q_2^{[2]}(R)\cos 2\eta Z + q_2^{[3]}(R)\cos 2\eta Z = 2\left[q_2^{[0]}(R) + q_2^{[2]}(R)\cos 2\eta Z \right]. \end{cases}$$

(A1.10.1)

All the postbuckling analysis for the Euler buckling mode in the main text and appendix is still valid for the barreling mode. The particular solution of $\mathbf{U}_2$ for the barreling mode can be obtained as Appendix A1.5 and 1.9.

A1.11 The influence of geometric imperfections

In this appendix, we show two examples about the influence of geometric imperfections on the buckling and postbuckling behavior of tubes using FEA. The buckling mode with an amplitude

δ_0 is introduced into the simulations as an imperfection; specifically, the imperfection amplitude $\delta_0/(B-A)=2\%$ is chosen here. Figure A1.11a and A1.11b show the average nominal stress-strain curves of tube structures in the vicinity of the buckling point. The blue curves are the theoretical predictions for the perfect tubes, while the black curves are the simulation results for the corresponding imperfect tubes. When $A/B=0.6$ and $B/H=0.1$, the tube undergoes snap-through buckling. The introduction of the imperfection smoothens the stress-strain curve, and reduces the critical stress by 2%, although the reduction of the critical strain is as small as 0.3%. When $A/B=0.6$ and $B/H=0.2$, the tube undergoes snap-back buckling. When the imperfection is introduced, both the critical strain and stress are significantly reduced by 6.5% and 10.5%, respectively.

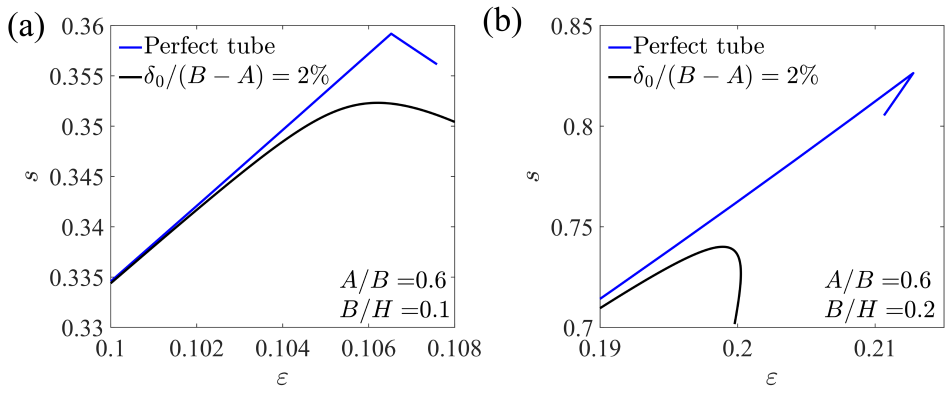

Figure A1.11. The postbuckling stress-strain relation for axially compressed tubes with fixed $A/B=0.6$ and different B/H: (a) $B/H=0.1$, (b) $B/H=0.2$. The blue curves correspond to perfect tubes and the black curves correspond to imperfect tubes with imperfection amplitude $\delta_0/(B-A)=2\%$.

Appendix 2 Supplementary Materials for Mechanics Underpinning Phase Separation of Hydrogels

In this appendix, we study phase behavior of hydrogels with $\chi = \chi_1 + \chi_2\phi$. The interaction parameters χ for many hydrogels depend on their polymer concentration ϕ. Here we demonstrate that our analysis can be easily extended to different $\chi(\phi)$ functions. A representative linear $\chi - \phi$ relation, $\chi = \chi_1 + \chi_2\phi$ with positive χ_1 and χ_2 constants, is adopted. We study the phase behavior of the hydrogel under free swelling and swelling under hydrostatic loading, and demonstrate that similar to a hydrogel with a constant χ, mechanical constraints can induce phase separation in hydrogels with non-constant χ.

A2.1 Free Swelling

When the hydrogel is under free swelling, we have $s = 0$. Similar to the main text, using the swelling ratio J as a variable, the free energy of the hydrogel is written as

$$W = \frac{1}{2}NkT\left(3J^{2/3} - 3 - 2\ln J\right) + \frac{kT}{v}\left[(J-1)\ln\frac{J-1}{J} + \chi_1\frac{J-1}{J} + \chi_2\frac{J-1}{J^2}\right]. \tag{A2.1}$$

When the hydrogel is in equilibrium, we obtain

$$\frac{\partial W}{\partial J} = NkT\left(J^{-\frac{1}{3}} - \frac{1}{J}\right) + \frac{kT}{v}\left[\ln\frac{J-1}{J} + \frac{1}{J} + \frac{\chi_1}{J^2} + \chi_2\left(\frac{2}{J^3} - \frac{1}{J^2}\right)\right] = \frac{\mu_w}{v}. \tag{A2.2}$$

The stability of the system is determined by the following equation,

$$\frac{\partial^2 W}{\partial J^2} = NkT\left(-\frac{1}{3}J^{-\frac{4}{3}} + J^{-2}\right) + \frac{kT}{v}\left[\frac{1}{(J-1)J^2} - \frac{2\chi_1}{J^3} + 2\chi_1\left(1 - \frac{3}{J}\right)\frac{1}{J^3}\right] = 0. \tag{A2.3}$$

A2.2 Swelling under Hydrostatic Loading

We consider a hydrogel under a hydrostatic loading immersed in a solvent with $\mu_w = 0$. The total free energy of the system is

$$G = \frac{d}{2} NkT\left(\lambda^2 - 1 - 2\ln\lambda\right) + \frac{kT}{v}\left[(\lambda^d - 1)\ln\frac{\lambda^d - 1}{\lambda^d} + \chi_1 \frac{\lambda^d - 1}{\lambda^d} + \chi_2 \frac{\lambda^d - 1}{\lambda^{2d}}\right] - ds\lambda, \tag{A2.4}$$

where $d = 3$. The equilibrium condition is rewritten as

$$\frac{\partial G}{\partial \lambda} = dNkT\left(\lambda - \frac{1}{\lambda}\right) + d\frac{kT}{v}\left(\lambda^{d-1}\ln\frac{\lambda^d - 1}{\lambda^d} + \frac{1}{\lambda} + \chi_1 \frac{1}{\lambda^{d+1}} - \chi_2 \frac{\lambda^d - 2}{\lambda^{2d+1}}\right) - ds = 0. \tag{A2.5}$$

The corresponding stability condition becomes

$$\begin{aligned}\frac{\partial^2 G}{\partial \lambda^2} = dNkT\left(1 + \frac{1}{\lambda^2}\right) + d\frac{kT}{v}\Bigg[&(d-1)\lambda^{d-2}\ln\frac{\lambda^d - 1}{\lambda^d} + \frac{d\lambda^{d-2}}{\lambda^d - 1} - \frac{1}{\lambda^2} - (d+1)\frac{\chi_1}{\lambda^{d+2}} \\ &+ \chi_2 \frac{1}{\lambda^{d+2}}\left((d+1) - (4d+2)\frac{1}{\lambda^d}\right)\Bigg] = 0\end{aligned} \tag{A2.6}$$

We first consider free swelling. The solutions to Eq. (A2.2) and to Eq. (A2.3), J as functions of χ_1, for three different χ_2 are plotted in Figure A2.a-A2.c, respectively. The equilibrium solutions and the spinodal curves at $\chi_2 = 0.1$ in Figure A1.a show the similar trend to that in Figure 3.2b. When $\chi_2 = 0.4$, the spinodal curve in red becomes non-monotonic, where χ_1 first decreases, then increases, and decreases again as the swelling ratio J increases. The black curve of the equilibrium solutions for $\mu_w = 0$ is also always below the spinodal curve in red, and therefore, there is only one equilibrium solution for a given χ_1. The green curve of the equilibrium solutions for $\mu_w = 0.0025kT$ intersects with the spinodal curve at three points, and therefore, there exist two stable equilibrium solutions for certain range of χ_1. The blue curve of the equilibrium solutions

when $\mu_w = 0.015kT$ also shows the similar trend with that in Figure 3.2b. When $\chi_2 = 0.7$, the black curve of the equilibrium solutions for $\mu_w = 0$ becomes non-monotonic, and there are two points of intersection with the spinodal curve, for χ_1 between which two phases can coexist.

Next, solving Eq. (A2.6), we show the spinodal curves of a hydrogel subjected to hydrostatic loading, λ as functions of χ_1, at different values of χ_2 in Figure A2.d. The curves with non-zero χ_2 show a similar trend to that with a zero χ_2. Setting $\chi_1 = 0.8$ and solving Eq. (A2.5), we plot the nominal stress s as a function of λ at different values of χ_2 in Figure A2.e. All the stress-stretch curves are non-monotonic. Though the hydrogel under free swelling may show different phase behaviors at different values of χ_2 (Figure A2.a-A2.c), the swelling behaviors are similar when external loading is applied (Figure A2.d-A2.e). Therefore, the effects of mechanical constraints on triggering phase separation of hydrogels are carefully studied in the main text for constant χ.

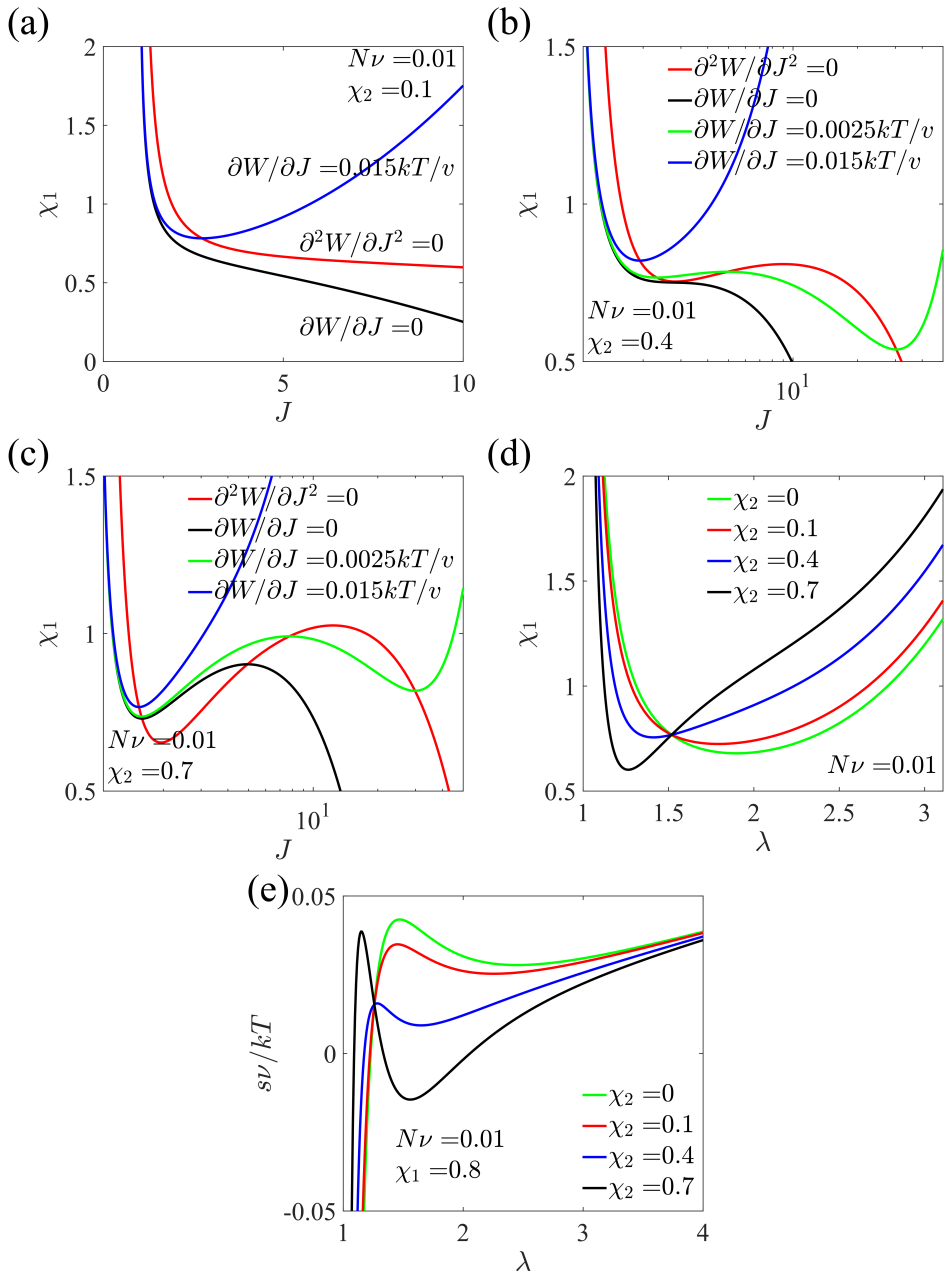

Figure A2 The equilibrium solutions and the spinodal curves of a hydrogel under equilibrium free swelling at (a) $\chi_2 = 0.1$, (b) $\chi_2 = 0.4$ and (c) $\chi_2 = 0.7$. (d) The spinodal curves of a hydrogel subjected to hydrostatic loading at various χ_2. (e) Nominal stress as a function of stretch for a hydrogel subjected to hydrostatic loading at various χ_2.

Appendix 3 Supplementary Materials for Fracture of Liquid Crystal Elastomers

A3.1 Material and Specimen Preparation

The main-chain monodomain LCEs were synthesized via a two-stage thiol-acrylate Michael addition-photopolymerization reaction [148]. The chemicals used include diacrylate mesogen, 1,4-Bis-[4-(3-arcyloyoxypropyloxy) benzoyloxy]-2-methylbenzene (RM257, 95%), crosslinker, pentaerythritol tetrakis(3-mercaptopropionate) (PETMP, 95%), chain extender, 2,2-(ethylenedioxy) diethanethiol (EDDET, 95%), catalyst, dipropylamine (DPA, 98%) and photoinitiator, (2-hydroxyethoxy)-2-methylpropiophenone (HHMP, 98%). RM257 (6.4g) was first dissolved in toluene (4g) at 80 ℃ and then cooled to room temperature. EDDET (1.465g), PETMP (0.347g), HHMP (0.041g), and DPA solution (DPA:toluene = 1:50, 0.768g in total) were subsequently added and thoroughly mixed using a vortex mixer at 3200rpm for 15mins. The solution was then degassed, poured into a mold, and cured at room temperature for 24 hours in the absence of light. After curing, the film was placed in an oven at 80 ℃ for 24 hours to remove the solvent. The film was then stretched to twice its original length and exposed to UV light for 1 hour to complete the second-stage crosslinking process. The specimens were cut into rectangular shapes with a pre-crack, each with a certain initial director (Figure 5.1a).

A3.2 Supplementary Figures

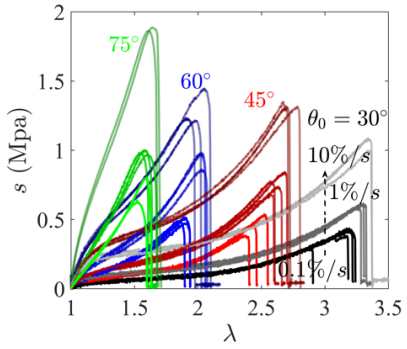

Figure A3.1 Stress-stretch curves of various samples. The fixed ratio of the applied stretch in the second cross-linking step is around 88~89%.

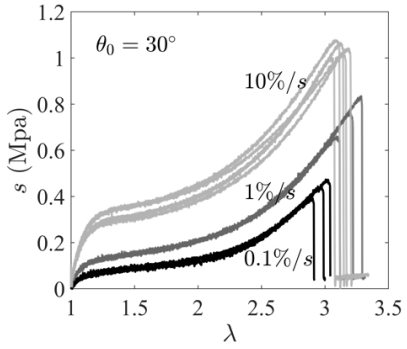

Figure A3.2 Stress-stretch curves of nonmonotonic stretch. The fixed ratio of the applied stretch in the second cross-linking step is about 85%.

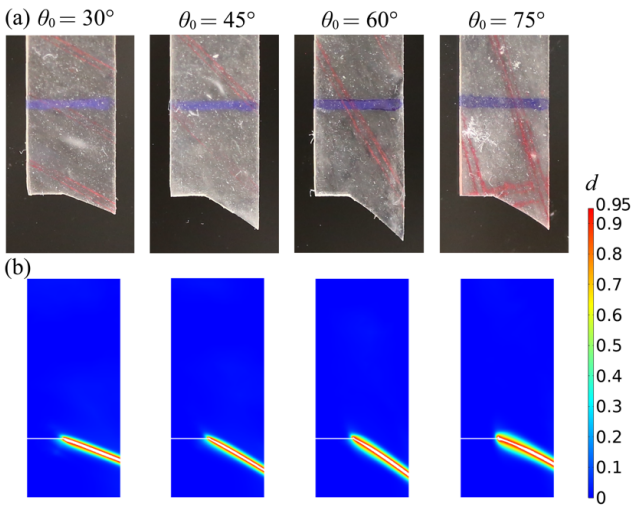

Figure A3.3 Fracture paths from (a) experiments and (b) simulations for different initial directors under the stretching rate $\dot{\lambda} = 1\%/s$.

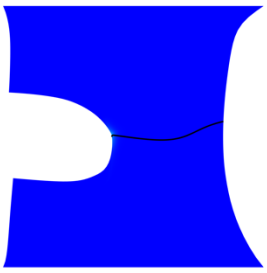

Figure A3.4 Tilted black line in front of the crack tip under $\lambda = 1.5$ and $\dot{\lambda} = 0.1\%/s$.

A3.3 Phase-field fracture model

We have developed a thermodynamically consistent phase-field fracture framework to simulate the fracture process of viscoelastic LCEs. Much of the theory below follows our previous work. Unlike other fracture model such as XFEM or cohesive zone model, the phase-field method uses a phase-field variable to implicitly trace interfaces without dealing with a sharp boundary, which is ideal for the LCE fracture with complex fracture paths [156]. The phase field $d \in [0,1]$ is introduced to describe the damage degree of the material. The director $\mathbf{n} = (cos\theta, sin\theta, 0)$ is

defined in the current state to describe the liquid crystal alignment, where θ is the angle between the director and x axis in the deformed configuration. We assume the viscosity originates from the network instead of the director. Using our developed viscoelastic model, we employ a rheological model by connecting the Kelvin-Voigt model and Maxwell model with N branches in parallel. The deformation gradient $\mathbf{F}$ in the Maxwell branches is decomposed to the elastic and viscous parts, $\mathbf{F} = \mathbf{F}_i^e \mathbf{F}_i^v$ $(i = 1,2,\dots,N)$. The free energy density of the material is formulated as a function of the state variables $\mathbf{F}$, $\mathbf{F}_i^v$, $\mathbf{n}$, and d,

$$\psi(\mathbf{F},\mathbf{F}_i^v,\mathbf{n},d) = g(d)\left[\psi_0(\mathbf{F},\mathbf{n}) + \sum_{i=1}^{N}\psi_i(\mathbf{F}\mathbf{F}_i^{v-1},\mathbf{n})\right], \tag{A3.1}$$

where $g(d)$ is the degradation function describing the material degradation due to damage, ψ_0 and ψ_i are the intact free energy densities of the equilibrium branch and nonequilibrium branches respectively. We use the phase-field regularized cohesive zone model developed to describe the quasi-brittle fracture [157, 158], where the degradation function is assumed to be

$$g(d) = \frac{(1-d)^2}{(1-d)^2 + a_1 d(1-0.5d)}, \tag{A3.2}$$

where $a_1 = \frac{2}{\pi}\frac{b_{ch}}{b_0}$ with a phase field length scale b_0 for numerical regularization and the fractocohesive length b_{ch}.

The free energy density of the equilibrium branch is

$$\begin{aligned}\psi_0 = {} & \frac{1}{2}\mu_0\left[tr\left(\mathbf{I}^{-1}\mathbf{F}\mathbf{I}_0\mathbf{F}^T\right) - 3 - 2\log(\det\mathbf{F})\right] + \mu_\alpha\left[tr\left(\mathbf{I}^{-1}\mathbf{F}\mathbf{I}_0\mathbf{F}^T\right) - 3\right]^2 \\ & + \frac{1}{2}\mu_0 a\left\|\mathbf{n}_\mathbf{F}\right\|^2 + \frac{1}{2}K(\det\mathbf{F} - 1)^2\end{aligned}, \tag{A3.3}$$

where μ_0 is the shear modulus, μ_α is a coefficient of nonlinear elasticity, K is the bulk modulus, $a = \frac{a_0}{m[tr(\mathbf{F}^T\mathbf{F})-3]+1}$ with a_0 being the semisoft parameter and m being a positive scaling factor, $\|\mathbf{n_F}\|^2 = tr[\mathbf{n}\otimes\mathbf{n}\cdot\mathbf{F}(\mathbf{I}-\mathbf{n}_0\otimes\mathbf{n}_0)\mathbf{F}^T]$, $\mathbf{l} = (r-1)\mathbf{n}\otimes\mathbf{n}+\mathbf{I}$ is the dimensionless shape tensor, and $\mathbf{l}_0 = (r-1)\mathbf{n}_0\otimes\mathbf{n}_0+\mathbf{I}$ is the dimensionless initial shape tensor, where r represents the average shape anisotropy of the network distribution, $\mathbf{n}_0 = (cos\theta_0, -sin\theta_0, 0)$ is the initial director with θ_0 being the angle between the director and x axis in the initial state (Figure 5.1a), and $\mathbf{I}$ is the identity tensor.

The free energy density for the nonequilibrium branch is

$$\begin{aligned}\psi_i = &\frac{1}{2}\mu_i\left\{\left[tr\left(\mathbf{l}^{-1}\mathbf{F}_i^e\mathbf{l}_0\mathbf{F}_i^{eT}\right)-3-2\log\left(\det\mathbf{F}_i^e\right)\right]+2\frac{\mu_\alpha}{\mu_0}\left[tr\left(\mathbf{l}^{-1}\mathbf{F}_i^e\mathbf{l}_0\mathbf{F}_i^{eT}\right)-3\right]^2\right\},\\ &+\frac{1}{2}\mu_i a_i\left\|\mathbf{n}_{\mathbf{F}_i^e}\right\|^2+\frac{1}{2}K_i\left(\det\mathbf{F}_i^e-1\right)^2\end{aligned} \tag{A3.4}$$

where μ_i is the shear modulus of the i-th branch, K_i is the parameter controlling the incompressibility of $\mathbf{F}_i^e$, $a_i = \frac{a_0}{m\left[tr\left(\mathbf{F}_i^{eT}\mathbf{F}_i^e\right)-3\right]+1}$, and $\left\|\mathbf{n}_{\mathbf{F}_i^e}\right\|^2 = tr[\mathbf{n}\otimes\mathbf{n}\cdot\mathbf{F}_i^e(\mathbf{I}-\mathbf{n}_0\otimes\mathbf{n}_0)\mathbf{F}_i^{eT}]$.

Considering an isothermal process and neglecting the body force, the energy balance of the system is

$$\int\dot{\psi}dV+\int\dot{\phi}dV=\int\mathbf{t}\cdot\dot{\mathbf{x}}dA, \tag{A3.5}$$

where $\dot{\phi}$ is the dissipated energy per unit time and per unit volume through viscous deformation and fracture, $\mathbf{t}$ is the traction acting on the surface. Thermodynamics requires the dissipated energy shouldn't decrease, namely, $\dot{\phi}\geq 0$.

The dissipation rate is contributed from the dashpot and fracture process,

$$\dot{\phi}\left(\dot{\mathbf{F}},\dot{\mathbf{F}}_i^v,d\right)=\dot{\phi}_0\left(\dot{\mathbf{F}},d\right)+\sum_{i=1}^{N}\dot{\phi}_i\left(\dot{\mathbf{F}}_i^v,d\right)+\dot{\phi}_f, \tag{A3.6}$$

where $\dot{\phi}_0$ is the dissipation rate from the dashpot of the Kelvin-Voigt model, $\dot{\phi}_i$ is from the dashpot of the i-th branch of the Maxwell model, and $\dot{\phi}_f$ is due to fracture.

We assume

$$\dot{\phi}_0\left(\dot{\mathbf{F}}\right)=g(d)\frac{\partial\varphi_0\left(\dot{\mathbf{F}}\right)}{\partial\dot{\mathbf{F}}}:\dot{\mathbf{F}}, \tag{A3.7}$$

and

$$\dot{\phi}_i\left(\dot{\mathbf{F}}_i^v\right)=g(d)\frac{\partial\varphi_i\left(\dot{\mathbf{F}}_i^v\right)}{\partial\dot{\mathbf{F}}_i^v}:\dot{\mathbf{F}}_i^v. \tag{A3.8}$$

The term φ_i is the so-called dissipation potential [149]. We assume the following form

$$\varphi_0=\frac{1}{8}\eta_0 J\left(\dot{\mathbf{F}}\mathbf{F}^{-1}+\mathbf{F}^{-T}\dot{\mathbf{F}}^T\right):\left(\dot{\mathbf{F}}\mathbf{F}^{-1}+\mathbf{F}^{-T}\dot{\mathbf{F}}^T\right), \tag{A3.9}$$

and

$$\varphi_i=\frac{1}{2}\eta_i\left(\dot{\mathbf{F}}_i^v\mathbf{F}_i^{v-1}\right):\left(\dot{\mathbf{F}}_i^v\mathbf{F}_i^{v-1}\right), \tag{A3.10}$$

where η_0 is a viscosity constant, $J=det\mathbf{F}$, and η_i is the viscosity changing nonlinearly with deformation.

Organizing Eqs. (A3.1-A3.10), we obtain

$$\int\left[-\mathrm{Div}\left(\frac{\partial\psi}{\partial\mathbf{F}}+g(d)\frac{\partial\varphi_0}{\partial\dot{\mathbf{F}}}\right)\cdot\dot{\mathbf{x}}+g(d)\sum_{i=1}^{N}\left(\frac{\partial\psi_i}{\partial\mathbf{F}_i^v}+\frac{\partial\varphi_i}{\partial\dot{\mathbf{F}}_i^v}\right):\dot{\mathbf{F}}_i^v+\frac{\partial\psi}{\partial\mathbf{n}}\cdot\dot{\mathbf{n}}+\left(\frac{\partial\psi}{\partial d}\dot{d}+\dot{\phi}_f\right)\right]\mathrm{d}V$$
$$+\int\left[\left(\frac{\partial\psi}{\partial\mathbf{F}}+g(d)\frac{\partial\varphi_0}{\partial\dot{\mathbf{F}}}\right)\cdot\mathbf{N}-\mathbf{t}\right]\cdot\dot{\mathbf{x}}\mathrm{d}A=0 \quad . \tag{A3.11}$$

The mechanical equilibrium equation, the evolution of $\mathbf{F}_i^v$, and the equilibrium equation for the director $\mathbf{n}$ can be obtained as follows.

The mechanical equilibrium and the corresponding boundary condition are

$$\mathrm{Div}\mathbf{P}=0\,, \tag{A3.12}$$

and

$$\mathbf{P}\cdot\mathbf{N}=\mathbf{t}\,, \tag{A3.13}$$

where the nominal stress $\mathbf{P}$ is defined as

$$\mathbf{P}=\frac{\partial\psi}{\partial\mathbf{F}}+g(d)\frac{\partial\varphi_0}{\partial\dot{\mathbf{F}}}\,. \tag{A3.14}$$

The evolution of $\mathbf{F}_i^v$ is

$$\frac{\partial\psi}{\partial\mathbf{F}_i^v}+\frac{\partial\varphi_i}{\partial\dot{\mathbf{F}}_i^v}=0\,. \tag{A3.15}$$

The equilibrium equation for the director is

$$\frac{\partial\psi}{\partial\mathbf{n}}=\left(\frac{\partial\psi}{\partial\mathbf{n}}\cdot\mathbf{n}\right)\mathbf{n}\,. \tag{A3.16}$$

The fracture process is governed by

$$\frac{\partial \psi}{\partial d}\dot{d}+\dot{\phi}_f=0, \tag{A3.17}$$

where the thermodynamics requirement $\dot{\phi}_f \geq 0$ is satisfied when $\dot{d} \geq 0$, since $\frac{\partial g(d)}{d} < 0$.

Instead of using Eq. (A3.17), we describe the fracture process based on the finding that the fracture propagation is determined by the competition between the equilibrium elastic energy and intrinsic fracture energy [159], with the following form

$$\frac{\partial g(d)}{\partial d}\psi_0\dot{d}+G_c\dot{\gamma}=0, \tag{A3.18}$$

where G_c is the intrinsic fracture energy and the crack surface density function γ is expressed as,

$$\gamma=\frac{1}{\pi}\left[\frac{1}{b_0}\left(2d-d^2\right)+b_0\nabla d\cdot\mathbf{A}\cdot\nabla d\right], \tag{A3.19}$$

where $\mathbf{A}$ is the second order structural tensor related to the director orientation, where the exact form $\mathbf{A}=\mathbf{I}+\alpha\mathbf{F}^{-1}\mathbf{n}_{\perp}\otimes\mathbf{F}^{-1}\mathbf{n}_{\perp}$ is derived in Appendix A3.4 based on the assumption that the crack prefers to propagate perpendicular to the director, α representing the coefficient of anisotropy of the fracture energy, and $\mathbf{n}_{\perp}$ being the unit vector perpendicular to the director.

Combining Eqs. (A3.3), (A3.4), (A3.9) and (A3.14), the nominal stress is

$$\mathbf{P}=g(d)\left\{\begin{array}{l}\mu_0\left[g_0\mathbf{l}^{-1}\mathbf{F}\mathbf{l}_0-\mathbf{F}^{-T}+a\mathbf{n}\otimes\mathbf{n}\cdot\mathbf{F}\left(\mathbf{I}-\mathbf{n}_0\otimes\mathbf{n}_0\right)-m\left(a^2/a_0\right)\left\|\mathbf{n}_{\mathbf{F}}\right\|^2\mathbf{F}\right]\\ +KJ(J-1)\mathbf{F}^{-T}+\frac{1}{2}\eta_0 J\left(\dot{\mathbf{F}}\mathbf{F}^{-1}+\mathbf{F}^{-T}\dot{\mathbf{F}}^{T}\right)\mathbf{F}^{-T}\\ +\sum_{i=1}^{N}\left[\begin{array}{l}\mu_i\left(g_i\mathbf{l}^{-1}\mathbf{F}_i^{e}\mathbf{l}_0-\mathbf{F}_i^{e-T}+a_i\mathbf{n}\otimes\mathbf{n}\cdot\mathbf{F}_i^{e}\left(\mathbf{I}-\mathbf{n}_0\otimes\mathbf{n}_0\right)\right)\\ -m\mu_i\left(a_i^2/a_0\right)\left\|\mathbf{n}_{\mathbf{F}_i^{e}}\right\|^2\mathbf{F}_i^{e}+K_iJ_i^{e}\left(J_i^{e}-1\right)\mathbf{F}_i^{e-T}\end{array}\right]\mathbf{F}_i^{v-T}\end{array}\right\}, \tag{A3.20}$$

where $g_0 = 1+4\left(\mu_\alpha/\mu_0\right)\left[tr\left(\mathbf{I}^{-1}\mathbf{F}\mathbf{l}_0\mathbf{F}^T\right)-3\right]$ and $g_i = 1+4\left(\mu_\alpha/\mu_0\right)\left[tr\left(\mathbf{I}^{-1}\mathbf{F}_i^e\mathbf{l}_0\mathbf{F}_i^{eT}\right)-3\right]$ decribe the nonlinear dependence of the stiffness on the deformation, and $J_i^e = \det\mathbf{F}_i^e$.

Utilizing Eqs. (A3.4), (A3.10) and (A3.15), the evolution of $\mathbf{F}_i^v$ is

$$\dot{\mathbf{F}}_i^v = \frac{\mu_i}{\eta_i}\begin{bmatrix} g_i\mathbf{F}_i^{eT}\mathbf{I}^{-1}\mathbf{F}_i^e\mathbf{l}_0\mathbf{F}_i^v - \mathbf{F}_i^v + a_i\left(\mathbf{F}_i^{eT}\mathbf{n}\otimes\mathbf{F}^T\mathbf{n} - \left(\mathbf{F}_i^{eT}\mathbf{n}\cdot\mathbf{n}_0\right)\mathbf{F}_i^{eT}\mathbf{n}\otimes\mathbf{F}_i^{vT}\mathbf{n}_0\right) \\ -m\left(a_i^2/a_0\right)\left\|\mathbf{n}_{\mathbf{F}_i^e}\right\|^2\mathbf{C}_i^e\mathbf{F}_i^v + \frac{K_i}{\mu_i}J_i^e\left(J_i^e-1\right)\mathbf{F}_i^v \end{bmatrix}. \tag{A3.21}$$

We assume that the viscosity η_i follows the relation $\eta_i = \eta_{i,0}g_0$ $(i = 0,1,\dots,N)$, where $\eta_{i,0}$ is a constant.

The evolution of the phase field is

$$\frac{\partial g(d)}{\partial d}\frac{\psi_0}{G_c} + \frac{1}{\pi}\left[\frac{1}{b_0}(2-2d) - 2b_0\nabla\cdot(\mathbf{A}\cdot\nabla d)\right] = 0. \tag{A3.22}$$

In ensure the irreversibility of the phase field, the history variable

$$\mathrm{H} = \max_{\tau\in[0,t]}\left\{\frac{\psi_0(\tau)}{G_c(\tau)}\right\} \tag{A3.23}$$

is introduced [160, 161], where we assume the intrinsic fracture energy is rate-dependent [162, 163], expressed as

$$G_c = \left[\sqrt{G_{c0}} + \beta\log\left(r_d/r_{d0}\right)\right]^2, \tag{A3.24}$$

where $r_d = \frac{1}{2}\sqrt{(\dot{\mathbf{F}}\mathbf{F}^{-1} + \mathbf{F}^{-T}\dot{\mathbf{F}}^{T}) : (\dot{\mathbf{F}}\mathbf{F}^{-1} + \mathbf{F}^{-T}\dot{\mathbf{F}}^{T})}$ represents the deformation rate, β is a scaling factor, and G_{c0} is the reference fracture energy with the reference deformation rate r_{d0}.

The fracture response is governed by the mechanical equilibrium equation (A3.12), the evolution of $\mathbf{F}_i^v$ (A3.21), the equilibrium equation for the director $\mathbf{n}$ (A3.16), and the evolution of the phase field d (A3.22). The model is implemented in COMSOL. The implementation details and material parameters are described in Appendix A3.5.

A3.4 Derivation of the Anisotropic Crack Geometric Function

We simply assume the material is incompressible, with $J = det\mathbf{F} \equiv 1$. To realize that the crack prefers to propagate perpendicular to the director, the crack surface is assumed to be the following form

$$\Gamma = \int \frac{1}{\pi}\left[\frac{1}{b_0}(2d - d^2) + b_0 \nabla d \cdot \nabla d + \alpha b_0 J\left(\nabla_x d \cdot \mathbf{n}_\perp\right)^2\right] dV, \tag{A3.25}$$

where α is the coefficient of anisotropy of the fracture energy. The first two terms correspond to the isotropic crack surface density function, and the additional term adds the energy penalty for crack that does not propagate perpendicular to the director. To reduce the fracture energy, large value of α can lead to

$$\nabla_x d \cdot \mathbf{n}_\perp = 0, \tag{A3.26}$$

which means the damage gradient is parallel to the director. Namely, the crack path is perpendicular to the director. We rewrite the above form

$$\Gamma = \int \frac{1}{\pi}\left[\frac{1}{b_0}(2d-d^2)+b_0\nabla d\cdot\nabla d+\alpha b_0\nabla_x d\cdot(\mathbf{n}_\perp\otimes\mathbf{n}_\perp)\cdot\nabla_x d\right]dV$$
$$= \int \frac{1}{\pi}\left[\frac{1}{b_0}(2d-d^2)+b_0\nabla d\cdot\nabla d+\alpha b_0(\nabla d\cdot\mathbf{F}^{-1})\cdot(\mathbf{n}_\perp\otimes\mathbf{n}_\perp)\cdot(\nabla d\cdot\mathbf{F}^{-1})\right]dV. \quad \text{(A3.27)}$$
$$= \int \frac{1}{\pi}\left[\frac{1}{b_0}(2d-d^2)+b_0\nabla d\cdot(\mathbf{I}+\alpha\mathbf{F}^{-1}\mathbf{n}_\perp\otimes\mathbf{F}^{-1}\mathbf{n}_\perp)\cdot\nabla d\right]dV$$

Then we obtained the expression of the structural tensor **A** in Eq. (A3.19).

A3.5 Implementation Details and Material Parameters

The developed model is implemented in COMSOL under plane stress conditions. The mechanical equilibrium, plane stress condition, and equations for the director, inelastic deformation and phase field are implemented using the weak form. Linear Lagrange interpolation is used for the displacement field, the director θ and the phase field, and discontinuous linear Lagrange interpolation is used for the inelastic deformation $\mathbf{F}_i^v$ and the out-of-plane stretch λ_{33}. An additional equation for the phase field can be implemented easily based on our previously provided COMSOL file. In the simulation, the thickness of the crack is $w_c = 0.5b_0$. In order to avoid fracture from boundary, when solving the phase field, only the region within $1/6H \leq Y \leq 5/6H$ is solved for the long sample and $1/5H \leq Y \leq 4/5H$ for the short sample. Converged results are obtained through mesh refinement. The mesh size around the fracture path is smaller than $0.5b_0$.

Similar to our work in Chapter 4, the viscosity parameters are determined by the stress relaxation test. The corresponding parameters and parameters related to the constitutive relations

are listed in the tables. For the parameters related to the fracture, we set the following parameters $b_0 = 0.1mm$, $b_{ch} = 1mm$, $\alpha = 20$, $G_{c0} = 589.2N/m$, $\beta = 0.08$, and $r_{d0} = \sqrt{\frac{3}{2}} \times 10^{-3}/s$.

Table 1. Viscosity parameters for fracture experiments

$\tau_i(s)$	0.1	0.5	3.5	31.5	346.5
μ_i/μ_0	10.910671	2.985292	1.368842	0.583728	0.282026

Table 2. Other material parameters for fracture experiments

μ_0(MPa)	r	a_0	m	K/μ_0	K_i/μ_i	$\eta_{0,0}$(MPa · s)	μ_α
0.3928	5.5	0.07	0.3	1000	1000	0.1964	1/2

Table 3. Parameters related to fracture properties

b_0(mm)	b_{ch}(mm)	α	G_{c0} (N/m)	$\beta(\sqrt{N/m})$	r_{d0} (s^{-1})
0.1	1	20	589.2	0.08	$\sqrt{1.5} \times 10^{-3}$

Reference

1. Yuk, H., B. Lu, and X. Zhao, *Hydrogel bioelectronics.* Chemical Society Reviews, 2019. **48**(6): p. 1642-1667.

2. Lim, H.R., et al., *Advanced soft materials, sensor integrations, and applications of wearable flexible hybrid electronics in healthcare, energy, and environment.* Advanced Materials, 2020. **32**(15): p. 1901924.

3. Wu, W., *Stretchable electronics: functional materials, fabrication strategies and applications.* Science and Technology of Advanced Materials, 2019. **20**(1): p. 187-224.

4. Huang, S., et al., *Flexible electronics: stretchable electrodes and their future.* Advanced Functional Materials, 2019. **29**(6): p. 1805924.

5. Polygerinos, P., et al., *Soft robotics: Review of fluid-driven intrinsically soft devices; manufacturing, sensing, control, and applications in human-robot interaction.* Advanced Engineering Materials, 2017. **19**(12): p. 1700016.

6. Majidi, C., *Soft-matter engineering for soft robotics.* Advanced Materials Technologies, 2019. **4**(2): p. 1800477.

7. Whitesides, G.M., *Soft robotics.* Angewandte Chemie International Edition, 2018. **57**(16): p. 4258-4273.

8. Cianchetti, M., et al., *Biomedical applications of soft robotics.* Nature Reviews Materials, 2018. **3**(6): p. 143-153.

9. Gorissen, B., et al., *Inflatable soft jumper inspired by shell snapping.* Science Robotics, 2020. **5**(42): p. eabb1967.

10. Ono, T., et al., *Lipophilic polyelectrolyte gels as super-absorbent polymers for nonpolar organic solvents.* Nature materials, 2007. **6**(6): p. 429-433.

11. Li, S., et al., *Digital light processing of liquid crystal elastomers for self-sensing artificial muscles.* Science Advances, 2021. **7**(30): p. eabg3677.

12. Flory, P.J. and J. Rehner Jr, *Statistical mechanics of cross-linked polymer networks I. Rubberlike elasticity.* The journal of chemical physics, 1943. **11**(11): p. 512-520.

13. Treloar, L.R.G., *The elasticity of a network of long-chain molecules—II.* Transactions of the Faraday Society, 1943. **39**: p. 241-246.

14. Zanchet, A., et al., *Use of styrene butadiene rubber industrial waste devulcanized by microwave in rubber composites for automotive application.* Materials & Design, 2012. **39**: p. 437-443.

15. Guerra, N.B., et al., *Biomedical applications of natural rubber latex from the rubber tree Hevea brasiliensis.* Materials Science and Engineering: C, 2021. **126**: p. 112126.

16. Rahimi, A. and A. Mashak, *Review on rubbers in medicine: Natural, silicone and polyurethane rubbers.* Plastics, rubber and composites, 2013. **42**(6): p. 223-230.

17. O'Halloran, A., F. O'malley, and P. McHugh, *A review on dielectric elastomer actuators, technology, applications, and challenges.* Journal of Applied Physics, 2008. **104**(7).

18. Romasanta, L.J., M.A. López-Manchado, and R. Verdejo, *Increasing the performance of dielectric elastomer actuators: A review from the materials perspective.* Progress in Polymer Science, 2015. **51**: p. 188-211.

19. Bastola, A.K. and M. Hossain, *A review on magneto-mechanical characterizations of magnetorheological elastomers.* Composites Part B: Engineering, 2020. **200**: p. 108348.

20. Kim, Y., et al., *Printing ferromagnetic domains for untethered fast-transforming soft materials.* Nature, 2018. **558**(7709): p. 274-279.

21. Li, Y., et al., *A state-of-the-art review on magnetorheological elastomer devices.* Smart materials and structures, 2014. **23**(12): p. 123001.

22. Calvert, P., *Hydrogels for soft machines.* Advanced materials, 2009. **21**(7): p. 743-756.

23. Osada, Y. and J.P. Gong, *Soft and wet materials: polymer gels.* Advanced Materials, 1998. **10**(11): p. 827-837.

24. Beebe, D.J., et al., *Functional hydrogel structures for autonomous flow control inside microfluidic channels.* Nature, 2000. **404**(6778): p. 588.

25. Peppas, N.A., et al., *Hydrogels in biology and medicine: from molecular principles to bionanotechnology.* Advanced materials, 2006. **18**(11): p. 1345-1360.

26. Warner, M. and E.M. Terentjev, *Liquid crystal elastomers*. Vol. 120. 2007: Oxford university press.

27. Herbert, K.M., et al., *Synthesis and alignment of liquid crystalline elastomers.* Nature Reviews Materials, 2022. **7**(1): p. 23-38.

28. White, T.J. and D.J. Broer, *Programmable and adaptive mechanics with liquid crystal polymer networks and elastomers.* Nature materials, 2015. **14**(11): p. 1087-1098.

29. Bisoyi, H.K. and Q. Li, *Light-driven liquid crystalline materials: from photo-induced phase transitions and property modulations to applications.* Chemical Reviews, 2016. **116**(24): p. 15089-15166.

30. Fowler, H.E., et al., *Liquid crystal elastomers with enhanced directional actuation to electric fields.* Advanced Materials, 2021. **33**(43): p. 2103806.

31. Ohzono, T., et al., *Internal constraints and arrested relaxation in main-chain nematic elastomers.* nature communications, 2021. **12**(1): p. 787.

32. Traugutt, N.A., et al., *Liquid-crystal-elastomer-based dissipative structures by digital light processing 3D printing.* Advanced Materials, 2020. **32**(28): p. 2000797.

33. Mistry, D., et al., *Soft elasticity optimises dissipation in 3D-printed liquid crystal elastomers.* Nature communications, 2021. **12**(1): p. 6677.

34. Saed, M.O., et al., *Impact damping and vibration attenuation in nematic liquid crystal elastomers.* Nature communications, 2021. **12**(1): p. 6676.

35. Kotikian, A., et al., *Untethered soft robotic matter with passive control of shape morphing and propulsion.* Science robotics, 2019. **4**(33): p. eaax7044.

36. He, Q., et al., *Electrospun liquid crystal elastomer microfiber actuator.* Science robotics, 2021. **6**(57): p. eabi9704.

37. Ohm, C., M. Brehmer, and R. Zentel, *Liquid crystalline elastomers as actuators and sensors.* Advanced materials, 2010. **22**(31): p. 3366-3387.

38. Iamsaard, S., et al., *Conversion of light into macroscopic helical motion.* Nature chemistry, 2014. **6**(3): p. 229-235.

39. Chen, Y. and L. Jin, *Snapping-back buckling of wide hyperelastic columns.* Extreme Mechanics Letters, 2019: p. 100600.

40. Wang, Q. and X. Zhao, *Beyond wrinkles: Multimodal surface instabilities for multifunctional patterning.* Mrs Bulletin, 2016. **41**(2): p. 115-122.

41. Chen, Y. and L. Jin, *Reusable energy-absorbing architected materials harnessing snapping-back buckling of wide hyperelastic columns.* Advanced Functional Materials, 2021. **31**(31): p. 2102113.

42. Pal, A., et al., *Exploiting mechanical instabilities in soft robotics: control, sensing, and actuation.* Advanced Materials, 2021. **33**(19): p. 2006939.

43. Matsuo, E.S. and T. Tanaka, *Patterns in shrinking gels.* Nature, 1992. **358**(6386): p. 482.

44. Lee, S. and M. Pharr, *Sideways and stable crack propagation in a silicone elastomer.* Proceedings of the National Academy of Sciences, 2019. **116**(19): p. 9251-9256.

45. Zhang, G., et al., *Hydrogels of arrested phase separation simultaneously achieve high strength and low hysteresis.* Science Advances, 2023. **9**(26): p. eadh7742.

46. Wang, M., et al., *Tough and stretchable ionogels by in situ phase separation.* Nature Materials, 2022: p. 1-7.

47. Shen, T., et al., *Nonsteady fracture of transient networks: The case of vitrimer.* Proceedings of the National Academy of Sciences, 2021. **118**(29): p. e2105974118.

48. Li, T., *A mechanics model of microtubule buckling in living cells.* Journal of biomechanics, 2008. **41**(8): p. 1722-1729.

49. Fung, Y.-C., *Mechanical properties and active remodeling of blood vessels*, in *Biomechanics*. 1993, Springer. p. 321-391.

50. Lan, W.-J., et al., *Sealing properties and structure optimization of packer rubber under high pressure and high temperature.* Petroleum Science, 2019. **16**(3): p. 632-644.

51. Chawla, K., et al., *Superior mechanical properties by exploiting size-effects and multiscale interactions in hierarchically architected foams.* arXiv preprint arXiv:2207.03023, 2022.

52. Noronha, J., et al., *Hollow-walled lattice materials by additive manufacturing: Design, manufacture, properties, applications and challenges.* Current Opinion in Solid State and Materials Science, 2021. **25**(5): p. 100940.

53. Tancogne-Dejean, T. and D. Mohr, *Elastically-isotropic elementary cubic lattices composed of tailored hollow beams.* Extreme Mechanics Letters, 2018. **22**: p. 13-18.

54. Meza, L.R., S. Das, and J.R. Greer, *Strong, lightweight, and recoverable three-dimensional ceramic nanolattices.* Science, 2014. **345**(6202): p. 1322-1326.

55. Dimitriyev, M.S., et al., *Swelling thermodynamics and phase transitions of polymer gels.* Nano Futures, 2019. **3**(4): p. 042001.

56. Xiong, Y., et al., *Phase Transitions and Pattern Formation in Chemo-Responsive Gels and Composites.* Israel Journal of Chemistry, 2018. **58**(6-7): p. 693-705.

57. Sakai, T., *Physics of polymer gels*. 2020: John Wiley & Sons.

58. Zhang, T., et al., *Hybrid nanodiamond quantum sensors enabled by volume phase transitions of hydrogels.* Nature communications, 2018. **9**(1): p. 1-8.

59. Visentin, F., et al., *Selective Stiffening in Soft Actuators by Triggered Phase Transition of Hydrogel-Filled Elastomers.* Advanced Functional Materials, 2021: p. 2101121.

60. Shiblee, M.D.N.I., et al., *4D printing of shape-memory hydrogels for soft-robotic functions.* Advanced Materials Technologies, 2019. **4**(8): p. 1900071.

61. Miyata, T., T. Uragami, and K. Nakamae, *Biomolecule-sensitive hydrogels.* Advanced drug delivery reviews, 2002. **54**(1): p. 79-98.

62. Cui, K., et al., *Multiscale energy dissipation mechanism in tough and self-healing hydrogels.* Physical review letters, 2018. **121**(18): p. 185501.

63. Sato, K., et al., *Phase-separation-induced anomalous stiffening, toughening, and self-healing of polyacrylamide gels.* Advanced Materials, 2015. **27**(43): p. 6990-6998.

64. Ji, D. and J. Kim, *Recent Strategies for Strengthening and Stiffening Tough Hydrogels.* Advanced NanoBiomed Research, 2021: p. 2100026.

65. Cui, W., et al., *Mechanical enhancement of hydrophobically associating hydrogels by solvent-regulated phase separation.* Polymer, 2020. **210**: p. 123042.

66. Li, X., et al., *Mesoscale bicontinuous networks in self-healing hydrogels delay fatigue fracture.* Proceedings of the National Academy of Sciences, 2020. **117**(14): p. 7606-7612.

67. Nonoyama, T., et al., *Instant thermal switching from soft hydrogel to rigid plastics inspired by thermophile proteins.* Advanced Materials, 2020. **32**(4): p. 1905878.

68. Wei, C., et al., *Rate-dependent stress-order coupling in main-chain liquid crystal elastomers.* Soft Matter, 2023. **19**(41): p. 7923-7936.

69. Chung, C., et al., *Revealing the unusual rate-dependent mechanical behaviors of nematic liquid crystal elastomers.* International Journal of Solids and Structures, 2024: p. 112712.

70. Wang, Z., et al., *A nonlinear viscoelasticity theory for nematic liquid crystal elastomers.* Journal of the Mechanics and Physics of Solids, 2022. **163**: p. 104829.

71. Cang, Y., et al., *On the origin of elasticity and heat conduction anisotropy of liquid crystal elastomers at gigahertz frequencies.* Nature Communications, 2022. **13**(1): p. 5248.

72. Ware, T.H., et al., *Localized soft elasticity in liquid crystal elastomers.* Nature communications, 2016. **7**(1): p. 10781.

73. Fan, W., Z. Wang, and S. Cai, *Rupture of polydomain and monodomain liquid crystal elastomer.* International journal of applied mechanics, 2016. **8**(07): p. 1640001.

74. Annapooranan, R. and S. Cai, *Thermally induced self-rupture of a constrained liquid crystal elastomer.* Engineering Fracture Mechanics, 2022. **269**: p. 108584.

75. Euler, L., *Methodus inveniendi lineas curvas maximi minimive proprietate gaudentes, sive solutio problematis isoperimetrici lattissimo sensu accepti.* 1744.

76. Van der Heijden, A.M.A., *WT Koiter's elastic stability of solids and structures*. 2008: Cambridge University Press Cambridge, UK:.

77. Coulais, C., et al., *Discontinuous buckling of wide beams and metabeams.* Physical review letters, 2015. **115**(4): p. 044301.

78. Lubbers, L.A., M. van Hecke, and C. Coulais, *A nonlinear beam model to describe the postbuckling of wide neo-Hookean beams.* Journal of the Mechanics and Physics of Solids, 2017. **106**: p. 191-206.

79. Triantafyllidis, N., W.M. Scherzinger, and H.J. Huang, *Post-bifurcation equilibria in the plane-strain test of a hyperelastic rectangular block.* International journal of solids and structures, 2007. **44**(11-12): p. 3700-3719.

80. Chen, Y. and L. Jin, *From continuous to snapping-back buckling: A post-buckling analysis for hyperelastic columns under axial compression.* International Journal of Non-Linear Mechanics, 2020. **125**: p. 103532.

81. Hohlfeld, E. and L. Mahadevan, *Scale and nature of sulcification patterns.* Physical review letters, 2012. **109**(2): p. 025701.

82. Wilkes, E.W., *On the stability of a circular tube under end thrust.* The Quarterly Journal of Mechanics and Applied Mathematics, 1955. **8**(1): p. 88-100.

83. Haughton, D.M. and R.W. Ogden, *Bifurcation of inflated circular cylinders of elastic material under axial loading—II. Exact theory for thick-walled tubes.* Journal of the Mechanics and Physics of Solids, 1979. **27**(5-6): p. 489-512.

84. Goriely, A., R. Vandiver, and M. Destrade, *Nonlinear euler buckling.* Proceedings of the Royal Society A: Mathematical, Physical and Engineering Sciences, 2008. **464**(2099): p. 3003-3019.

85. Pan, F. and M.F. Beatty, *Remarks on the instability of an incompressible and isotropic hyperelastic, thick-walled cylindrical tube.* Journal of elasticity, 1997. **48**(3): p. 218-239.

86. Dorfmann, A. and D.M. Haughton, *Stability and bifurcation of compressed elastic cylindrical tubes.* International Journal of Engineering Science, 2006. **44**(18-19): p. 1353-1365.

87. Dai, H.-H., et al., *Pitchfork and octopus bifurcations in a hyperelastic tube subjected to compression: Analytical post-bifurcation solutions and imperfection sensitivity.* Mathematics and Mechanics of Solids, 2015. **20**(1): p. 25-52.

88. Budiansky, B., *Theory of buckling and post-buckling behavior of elastic structures*, in *Advances in applied mechanics*. 1974, Elsevier. p. 1-65.

89. Chakrabarti, A., et al., *Selection of hexagonal buckling patterns by the elastic Rayleigh-Taylor instability.* Journal of the Mechanics and Physics of Solids, 2018. **121**: p. 234-257.

90. Fu, Y.B. and R.W. Ogden, *Nonlinear stability analysis of pre-stressed elastic bodies.* Continuum Mechanics and Thermodynamics, 1999. **11**(3): p. 141-172.

91. Bigoni, D. and M. Gei, *Bifurcations of a coated, elastic cylinder.* International Journal of Solids and Structures, 2001. **38**(30-31): p. 5117-5148.

92. Yang, P., et al., *A perturbation force based approach to creasing instability in soft materials under general loading conditions.* Journal of the Mechanics and Physics of Solids, 2021. **151**: p. 104401.

93. Jin, L. and Z. Suo, *Smoothening creases on surfaces of strain-stiffening materials.* Journal of the Mechanics and Physics of Solids, 2015. **74**: p. 68-79.

94. Cai, S., et al., *Creasing instability of elastomer films.* Soft Matter, 2012. **8**(5): p. 1301-1304.

95. Wong, W.H., et al., *Surface instability maps for soft materials.* Soft Matter, 2010. **6**(22): p. 5743-5750.

96. Chen, D., et al., *Surface energy as a barrier to creasing of elastomer films: An elastic analogy to classical nucleation.* Physical review letters, 2012. **109**(3): p. 038001.

97. Hong, W., X. Zhao, and Z. Suo, *Formation of creases on the surfaces of elastomers and gels.* Applied Physics Letters, 2009. **95**(11): p. 111901.

98. Von Karman, T. and H.-S. Tsien, *The buckling of thin cylindrical shells under axial compression.* Journal of the Aeronautical Sciences, 1941. **8**(8): p. 303-312.

99. Kobayashi, T., Y. Mihara, and F. Fujii, *Path-tracing analysis for post-buckling process of elastic cylindrical shells under axial compression.* Thin-Walled Structures, 2012. **61**: p. 180-187.

100. Biot, M.A., *Surface instability of rubber in compression.* Applied Scientific Research, Section A, 1963. **12**(2): p. 168-182.

101. Fu, Y.B., *Perturbation methods and nonlinear stability analysis.* LONDON MATHEMATICAL SOCIETY LECTURE NOTE SERIES, 2001: p. 345-391.

102. Donnell, L.H. and C.C. Wan, *Effect of imperfections on buckling of thin cylinders and columns under axial compression.* 1950.

103. Liu, T., et al., *Buckling of viscoelastic spherical shells.* Journal of the Mechanics and Physics of Solids, 2022. **169**: p. 105084.

104. Li, Y. and T. Tanaka, *Phase transitions of gels.* Annual Review of Materials Science, 1992. **22**(1): p. 243-277.

105. Tanaka, T., et al., *Phase transitions in ionic gels.* Physical Review Letters, 1980. **45**(20): p. 1636.

106. Zhou, Y. and L. Jin, *Hydrolysis-induced large swelling of polyacrylamide hydrogels.* Soft Matter, 2020. **16**(24): p. 5740-5749.

107. Hirokawa, Y. and T. Tanaka. *Volume phase transition in a non-ionic gel*. 1984. American Institute of Physics.

108. Shen, T., et al., *On the blistering of thermo-sensitive hydrogel: the volume phase transition and mechanical instability.* Soft matter, 2019. **15**(29): p. 5842-5853.

109. Suzuki, A., S. Yoshikawa, and G. Bai, *Shrinking pattern and phase transition velocity of poly (N-isopropylacrylamide) gel.* The Journal of chemical physics, 1999. **111**(1): p. 360-367.

110. Bai, G. and A. Suzuki, *Phase separation of weakly ionized polymer gels during shrinking phase transition.* The Journal of Chemical Physics, 1999. **111**(22): p. 10338-10346.

111. Cai, S. and Z. Suo, *Mechanics and chemical thermodynamics of phase transition in temperature-sensitive hydrogels.* Journal of the Mechanics and Physics of Solids, 2011. **59**(11): p. 2259-2278.

112. Yu, Y., C.M. Landis, and R. Huang, *Salt-induced swelling and volume phase transition of polyelectrolyte gels.* Journal of Applied Mechanics, 2017. **84**(5).

113. Doi, M., *Gel dynamics.* Journal of the Physical Society of Japan, 2009. **78**(5): p. 052001.

114. Tomari, T. and M. Doi, *Swelling dynamics of a gel undergoing volume transition.* Journal of the Physical Society of Japan, 1994. **63**(6): p. 2093-2101.

115. Tomari, T. and M. Doi, *Hysteresis and incubation in the dynamics of volume transition of spherical gels.* Macromolecules, 1995. **28**(24): p. 8334-8343.

116. Hong, W. and X. Wang, *A phase-field model for systems with coupled large deformation and mass transport.* Journal of the Mechanics and Physics of Solids, 2013. **61**(6): p. 1281-1294.

117. Bao, X., H. Li, and H. Zhang, *Model for the phase separation of poly (N-isopropylacrylamide)–clay nanocomposite hydrogel based on energy-density functional.* Physical Review E, 2020. **101**(6): p. 062118.

118. Hennessy, M.G., A. Münch, and B. Wagner, *Phase separation in swelling and deswelling hydrogels with a free boundary.* Physical Review E, 2020. **101**(3): p. 032501.

119. Celora, G.L., et al., *A kinetic model of a polyelectrolyte gel undergoing phase separation.* Journal of the Mechanics and Physics of Solids, 2022: p. 104771.

120. Cirillo, E.N.M., P. Nardinocchi, and G. Sciarra, *Temperature-driven volume transition in hydrogels: Phase-coexistence and interface localization.* International Journal of Non-Linear Mechanics, 2016. **81**: p. 115-121.

121. Duda, F.P., A.C. Souza, and E. Fried, *Solvent uptake and cavitation.* Journal of the Mechanics and Physics of Solids, 2011. **59**(11): p. 2341-2354.

122. Yamamoto, T., Y. Masubuchi, and M. Doi, *Coil-globule transitions drive discontinuous volume conserving deformation in locally restrained gels.* Nature communications, 2018. **9**(1): p. 1-8.

123. Liu, M., et al., *An anisotropic hydrogel with electrostatic repulsion between cofacially aligned nanosheets.* Nature, 2015. **517**(7532): p. 68-72.

124. Kim, Y.S., et al., *Thermoresponsive actuation enabled by permittivity switching in an electrostatically anisotropic hydrogel.* Nature materials, 2015. **14**(10): p. 1002-1007.

125. Dušková-Smrčková, M. and K. Dušek, *How to Force Polymer Gels to Show Volume Phase Transitions.* ACS Macro Letters, 2019. **8**(3): p. 272-278.

126. Chang, Y.-W., et al., *Extreme thermodynamics with polymer gel tori: Harnessing thermodynamic instabilities to induce large-scale deformations.* Physical Review E, 2018. **98**(2): p. 020501.

127. !!! INVALID CITATION !!! .

128. Flory, P.J., *Thermodynamics of high polymer solutions.* The Journal of chemical physics, 1942. **10**(1): p. 51-61.

129. Flory, P.J., *Principles of polymer chemistry*. 1953: Cornell University Press.

130. Hirotsu, S., *Softening of bulk modulus and negative Poisson's ratio near the volume phase transition of polymer gels.* The Journal of chemical physics, 1991. **94**(5): p. 3949-3957.

131. Barton, A.F.M., *Handbook of polymer-liquid interaction parameters and solubility parameters*. 2018: Routledge.

132. Okumura, D. and S.A. Chester, *Ultimate swelling described by limiting chain extensibility of swollen elastomers.* International Journal of Mechanical Sciences, 2018. **144**: p. 531-539.

133. Dušek, K., et al., *Constrained swelling of polymer networks: characterization of vapor-deposited cross-linked polymer thin films.* Macromolecules, 2014. **47**(13): p. 4417-4427.

134. Sun, C., et al., *Fibrous gels modelled as fluid-filled continua with double-well energy landscape.* Proceedings of the Royal Society A, 2020. **476**(2244): p. 20200643.

135. Hong, W., et al., *A theory of coupled diffusion and large deformation in polymeric gels.* Journal of the Mechanics and Physics of Solids, 2008. **56**(5): p. 1779-1793.

136. Tanaka, T., *Collapse of gels and the critical endpoint.* Physical review letters, 1978. **40**(12): p. 820.

137. Bladon, P., E.M. Terentjev, and M. Warner, *Transitions and instabilities in liquid crystal elastomers.* Physical Review E, 1993. **47**(6): p. R3838.

138. Verwey, G.C. and M. Warner, *Compositional fluctuations and semisoftness in nematic elastomers.* Macromolecules, 1997. **30**(14): p. 4189-4195.

139. Biggins, J.S., E.M. Terentjev, and M. Warner, *Semisoft elastic response of nematic elastomers to complex deformations.* Physical Review E, 2008. **78**(4): p. 041704.

140. He, X., et al., *Uniaxial tension of a nematic elastomer with inclined mesogens.* Extreme Mechanics Letters, 2020. **40**: p. 100936.

141. Linares, C.P.M., et al., *The effect of alignment on the rate-dependent behavior of a main-chain liquid crystal elastomer.* Soft Matter, 2020. **16**(38): p. 8782-8798.

142. Luo, C., et al., *Real-time alignment and reorientation of polymer chains in liquid crystal elastomers.* ACS Applied Materials & Interfaces, 2021. **14**(1): p. 1961-1972.

143. Zhang, Y., et al., *Continuum mechanical modeling of liquid crystal elastomers as dissipative ordered solids.* Journal of the Mechanics and Physics of Solids, 2019. **126**: p. 285-303.

144. Wei, C., et al., *Exceptional stress-director coupling at the crack tip of a liquid crystal elastomer.* Journal of the Mechanics and Physics of Solids, 2024. **183**: p. 105522.

145. Guo, Q., Y. Zheng, and S. Cai, *Modeling and numerical simulation of thermo-electro-mechanical coupling behaviors of liquid crystal elastomers.* International Journal of Plasticity, 2023. **171**: p. 103799.

146. Chehade, A.E.H., et al., *Finite element modeling of viscoelastic liquid crystal elastomers.* 2023.

147. Zhou, H. and K. Bhattacharya, *Accelerated computational micromechanics and its application to polydomain liquid crystal elastomers.* Journal of the Mechanics and Physics of Solids, 2021. **153**: p. 104470.

148. Saed, M.O., et al., *Synthesis of programmable main-chain liquid-crystalline elastomers using a two-stage thiol-acrylate reaction.* JoVE (Journal of Visualized Experiments), 2016(107): p. e53546.

149. Kumar, A. and O. Lopez-Pamies, *On the two-potential constitutive modeling of rubber viscoelastic materials.* Comptes Rendus Mecanique, 2016. **344**(2): p. 102-112.

150. DeSimone, A. and G. Dolzmann, *Macroscopic Response Of¶ Nematic Elastomers via Relaxation Of¶ a Class of SO (3)-Invariant Energies.* Archive for rational mechanics and analysis, 2002. **161**: p. 181-204.

151. Zhang, Y., Z. Zhang, and Y. Huo, *Nucleation and critical conditions for stripe domains in monodomain nematic elastomer sheets under uniaxial loading.* Journal of the Mechanics and Physics of Solids, 2020. **144**: p. 104110.

152. Mandal, T.K., V.P. Nguyen, and J.-Y. Wu, *A length scale insensitive anisotropic phase field fracture model for hyperelastic composites.* International Journal of Mechanical Sciences, 2020. **188**: p. 105941.

153. Tutwiler, V., et al., *Rupture of blood clots: Mechanics and pathophysiology.* Science advances, 2020. **6**(35): p. eabc0496.

154. Ramanujam, R.K., et al., *Mechanics and microstructure of blood plasma clots in shear driven rupture.* Soft Matter, 2024.

155. Fernández-Rico, C., et al., *Elastic microphase separation produces robust bicontinuous materials.* Nature Materials, 2024. **23**(1): p. 124-130.

156. Wu, J.-Y., et al., *Computational modeling of localized failure in solids: XFEM vs PF-CZM.* Computer Methods in Applied Mechanics and Engineering, 2019. **345**: p. 618-643.

157. Wu, J.-Y., *A unified phase-field theory for the mechanics of damage and quasi-brittle failure.* Journal of the Mechanics and Physics of Solids, 2017. **103**: p. 72-99.

158. Wu, J.-Y., et al., *Phase-field modeling of fracture.* Advances in applied mechanics, 2020. **53**: p. 1-183.

159. Shrimali, B. and O. Lopez-Pamies, *The "pure-shear" fracture test for viscoelastic elastomers and its revelation on Griffith fracture.* Extreme Mechanics Letters, 2023. **58**: p. 101944.

160. Dammaß, F., et al., *Rate-and temperature-dependent ductile-to-brittle fracture transition: Experimental investigation and phase-field analysis for toffee.* Engineering Fracture Mechanics, 2024. **297**: p. 109878.

161. Miehe, C., F. Welschinger, and M. Hofacker, *Thermodynamically consistent phase-field models of fracture: Variational principles and multi-field FE implementations.* International journal for numerical methods in engineering, 2010. **83**(10): p. 1273-1311.

162. Yang, Z., et al., *Modified cohesive zone model for soft adhesive layer considering rate dependence of intrinsic fracture energy.* Engineering Fracture Mechanics, 2021. **258**: p. 108089.

163. Xie, X., et al., *An innovative tensile test method to evaluate the effect of the loading rate on viscoelastic interfaces.* Engineering Fracture Mechanics, 2022. **276**: p. 108872.